An Investigation of Real Gas Effects in Supercritical CO_2 Compressors

by

Nikola D. Baltadjiev

Submitted to the Department of Aeronautics and Astronautics
in partial fulfillment of the requirements for the degree of

Master of Science

at the

MASSACHUSETTS INSTITUTE OF TECHNOLOGY

September 2012

Author .....
Department of Aeronautics and Astronautics
August 23, 2012

Certified by .....
Zoltán S. Spakovszky
Professor of Aeronautics and Astronautics
Thesis Supervisor

Accepted by .....
Eytan H. Modiano
Professor of Aeronautics and Astronautics
Chair, Graduate Program Committee

An Investigation of Real Gas Effects in Supercritical CO_2 Compressors

by

Nikola D. Baltadjiev

Submitted to the Department of Aeronautics and Astronautics
on August 23, 2012, in partial fulfillment of the
requirements for the degree of
Master of Science

Abstract

This thesis presents a comprehensive assessment of real gas effects on the performance and matching of centrifugal compressors operating with CO_2 at supercritical conditions. The analytical framework combines first principles based modeling with targeted numerical simulations to characterize the internal flow behavior of supercritical fluids with implications for turbomachinery design and analysis. Trends in gas dynamic behavior, not observed for ideal fluids, are investigated using the influence coefficients for compressible channel flow derived for real gas. The variation in the properties of CO_2 and the expansion through the vapor-pressure curve due to local flow acceleration are identified as possible mechanisms for performance and operability issues observed near the critical point.

The performance of a centrifugal compressor stage is assessed at different thermodynamic conditions relative to the critical point using high fidelity simulations. The results indicate a reduction of 9% in the choke margin of the stage compared to its performance at ideal gas conditions due to variations in real gas properties. Compressor stage matching is also impacted by real gas effects as the excursion in corrected mass flow per unit area from inlet to outlet increases by 5%.

Investigation of the flow field near the impeller leading edge at high flow coefficients shows that local flow acceleration causes the thermodynamic conditions to reach the vapor-pressure curve. The significance of two-phase flow effects is determined through a non-dimensional parameter that relates the time required for liquid droplet formation to the residence time of the flow under saturation conditions. Applying this criterion to the candidate compressor stage shows that condensation is not a concern at the investigated operating conditions. In the immediate vicinity of the critical point however, this effect is expected to become more prominent.

While the focus of this analysis is on supercritical CO_2 compressors for carbon capture and sequestration, the methodology is directly applicable to other non-conventional fluids and applications. Experimental work is proposed to validate the key concepts and findings of this thesis.

Thesis Supervisor: Zoltán S. Spakovszky
Title: Professor of Aeronautics and Astronautics

Acknowledgments

First and foremost, I would like to express my deepest gratitude to my advisor, Prof. Zoltán Spakovszky, for his guidance and mentorship over the past two years. His dedication and passion for fluid mechanics provided a great source of wisdom and inspiration during my academic career.

I would like to thank Dr. Sumiu Uchida and Dr. Eisaku Ito of Mitsubishi Heavy Industries for the continued support of this project. I especially wish to thank Mr. Akihiro Nakaniwa for providing valuable feedback throughout our regular interactions.

I am also very grateful to Dr. Claudio Lettieri for being a great mentor and a friend. His unwavering support and expertise in numerical methods have helped me resolved many tough challenges along the way.

My learning experience would not have been the same without all the members of the Gas Turbine Lab, who made it a stimulating and exciting place to work. I am particularly indebted to Dr. Jeff Defoe, Dorian Colas, and Anne-Raphael Aubry for sharing their thoughts and experiences with me.

I wish to thank my parents, Dimitar Baltadjiev and Boyka Baltadjieva, and my sister, Denitsa Baltadjieva, for their encouragement and devotion and for always being there for me.

I could not have done this without one special person, my love Albena Karapska.

Contents

List of Figures

List of Tables

Nomenclature

Symbols

a_i^0 thermodynamic constant

a speed of sound, specific Helmholtz free energy

A area, Helmholtz free energy

b channel width

b_i thermodynamic constant

B thermodynamic constant

c absolute velocity

c_i thermodynamic constant

C thermodynamic constant

c_m meridional velocity

c_r radial velocity

c_p isobaric specific heat capacity

c_v isochoric specific heat capacity

d diameter

d_i thermodynamic constant

D thermodynamic constant

F_{shaft} shaft force

G Gibbs free energy

g specific Gibbs free energy

h specific enthalpy

l length scale

J nucleation rate

J_t Joule-Thomson coefficient

M Mach number

M_{U_2} machine Mach number

m molecular mass

$\dot{m}$ mass flow rate

m_s isentropic temperature exponent

N_s specific speed

n polytropic exponent

n_s isentropic pressure exponent

n_i thermodynamic constant

p pressure

p_s saturation pressure

p_v vapor pressure

r radius, radial coordinate

R gas constant

Re Reynolds number

S supersaturation

s specific entropy

t_i thermodynamic constant

t_n nucleation time

t_r residence time

T temperature

U_2 impeller tip speed

u specific internal energy

v specific volume

V volume

w relative velocity

w_p specific polytropic work

w_{shaft} shaft work

X general notation for thermodynamic property, compressibility function [6]

Y compressibility function [6]

Z compressibility factor

α absolute flow angle

α_i thermodynamic constant

β relative flow angle, thermodynamic constant

β' blade metal angle

β_i thermodynamic constant

β_p isobaric compressibility

β_T isothermal compressibility

γ ratio of specific heats, thermodynamic constant

Γ fundamental derivative

δ reduced density

ϵ_i thermodynamic constant

η_p polytropic efficiency

θ_i^0 thermodynamic constant

κ Boltzmann's constant

μ_0 work coefficient

μ_p pressure coefficient

ν kinematic viscosity

ρ density

ρ_l liquid density

σ surface tension

τ inverse reduced temperature

ϕ flow coefficient, reduced Helmholtz free energy

ψ loading coefficient

ω acentric factor

Ω rotational speed

Subscripts

0 stage inlet

1 impeller inlet

2 impeller outlet

3 diffuser outlet

4 stage outlet

c critical condition

d design quantity

i thermodynamic constant index

r reduced quantity

t stagnation quantity

Superscripts

^{0} ideal gas contribution, simple fluid contribution

^{r} residual part contribution, reference fluid contribution

Abbreviations

BL boundary layer

CCS carbon capture and sequestration

EOR enhanced oil recovery

EOS equation of state

LE leading edge

LHS left hand side

LK Lee-Kesler

NIST National Institute of Standards and Technology

RANS Reynolds-averaged Navier-Stokes

RHS right hand side

SW Span-Wagner

TE trailing edge

Chapter 1

Introduction

1.1 Background and Motivation

Despite efforts to utilize reusable energy sources, like wind and solar power, fossil fuels remain the primary source of energy worldwide. Coal-burning power plants produce nearly 40% of carbon dioxide emissions, nevertheless cleaner alternatives cannot compete with them because coal is such a cheap and widely available resource [7]. One way to reduce the negative impact of coal-burning power plants on the environment is by means of carbon capture and sequestration (CCS). In this process CO_2 is captured before being released into the atmosphere, compressed to very high pressures reaching supercritical state, and injected deep underground into saline aquifers or coal beds, as shown in Fig. 1-1. At this state, the fluid has the density of a liquid and the viscosity of a gas. It also expands to fill up a volume just like a gas does, therefore these fluids are sometimes refer to as dense gases. This makes it a very suitable working fluid for extracting natural gas and oil in a process known as Enhanced Oil Recovery (EOR), yielding 50% more oil than standard methods using air and water. Retrofitting plants with CCS systems however is very costly and power requirements can reach up to 20% of the plant gross power output [8]. In the US alone more than 5 billion tons of CO_2 per year are released into the atmosphere [7]. Given the enormous scale of these applications, efficiency levels can have a dramatic impact on operating costs and profits.

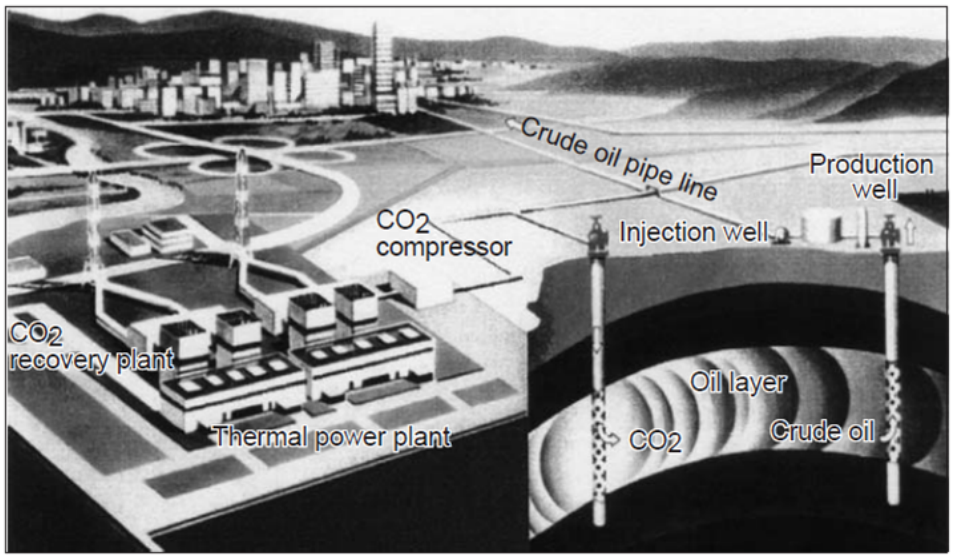

Figure 1-1: Carbon dioxide sequestration and storage [1].

1.2 Challenges

The majority of the work in the literature is on modeling the properties of supercritical fluids (i.e. equation of state (EOS) modeling). The behavior of these fluids in turbomachinery internal flow environments however, is still largely unknown. Current practice employs standard compressor stages designed for conventional fluids for use in supercritical applications. This can lead to decreased performance levels and operability issues. Common design tools coupled with thermodynamic property models are used to analyze the performance and the matching of centrifugal compressor stages, but what is missing is a clear description and characterization of the real gas effects of the fluid on the internal flow behavior and related mechanisms.

1.2.1 Compressor Under Investigation

Schematic representation of the CO_2 re-injection compressor investigated in this study is shown in Fig. 1-2. Carbon dioxide at atmospheric pressure is supplied at the inlet of the machine and raised to 203 bar at the outlet, yielding a pressure ratio of over 200. The power requirement for the drive motor of the system is 11.7 MW [2]. The compressor consists of a low pressure and a high pressure sections driven by

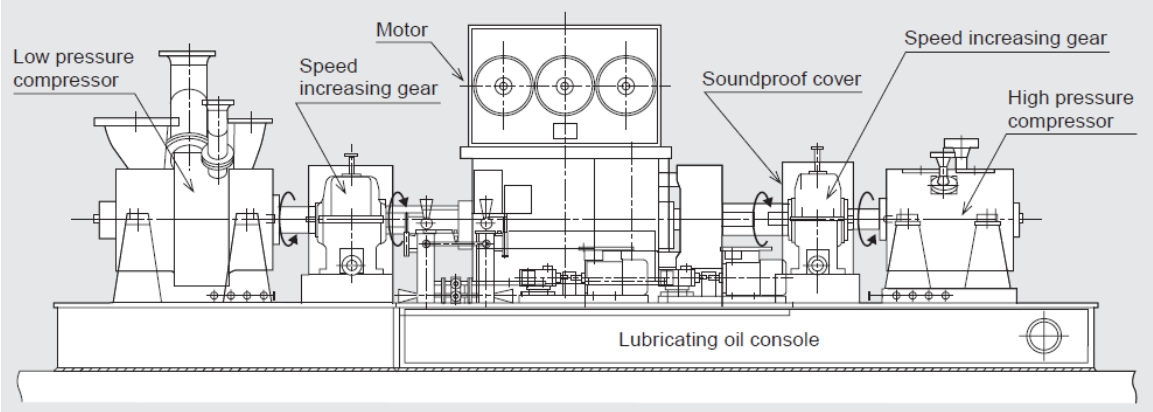

Figure 1-2: CO_2 re-injection compressor configuration from [2].

the electric motor through individual gear boxes. The low pressure section contains a total of 6 centrifugal compressor stages divided into two blocks, while the high pressure section has 7 stages divided into two blocks as well, with the four blocks connected via intercoolers (not shown here). The compression process is represented on the T-s diagram in Fig. 1-3. The first stage in the last block of the machine is closest to the critical point and is selected as the candidate stage to be analyzed in this study.

1.2.2 Problem Statement

Experimental data over a range of inlet conditions for the last block has helped determine an empirical safety boundary, represented by the red line in Fig. 1-3, beyond which performance and stability issues were observed, but the root cause could not be identified. Due to the nature of the experiments, no individual stage data could be obtained to identify the location and the exact conditions under which the issues arise. Current understanding of the internal flow behavior of supercritical fluids is a limiting factor in describing the mechanisms behind those issues.

Near critical and supercritical conditions, the ideal gas law does not hold for CO_2, because of significant variations in the thermodynamic properties. On the other hand, the proximity of the candidate stage to the two-phase region suggests the need to assess the possibility of localized condensation inside the compressor. The rigorous

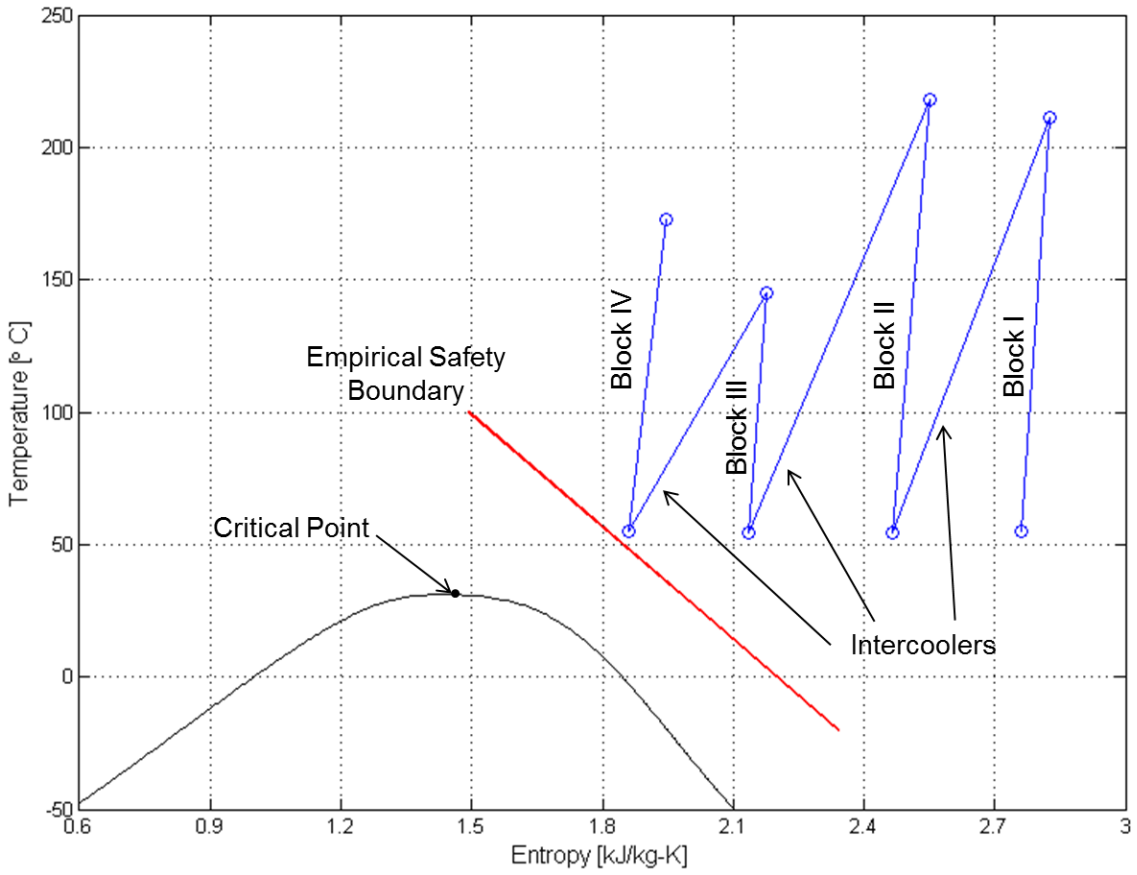

Figure 1-3: CO_2 compression process on a T-s diagram.

investigation of these real gas effects in supercritical CO_2 compressors will enable a more accurate assessment of compressor performance and stage matching and help mitigate in-field problems.

1.3 Review of Previous Work

Research efforts on supercritical CO_2 compressors have mainly focused on optimizing the compression process to reduce the power requirements. Several variations of the conventional centrifugal compression system are discussed by Moore and Nored in [9]. To improve the efficiency of the process, a semi-isothermal compression is proposed using intercooling between each centrifugal stage. This approach however, adds significant complexity to the system and leads to potential reliability risks. The development of an internally cooled centrifugal compressor is presented in [10], where

a cooling jacket is embedded around the gas flow path. The experimental results from a single stage test rig showed that over 50% of the heat addition by the impeller can be removed. The feasibility of this concept in a multistage configuration at supercritical pressures has yet to be determined.

An alternative method is to liquefy the CO_2 after the first vapor compression and use cryogenic liquid pumps to reach supercritical pressure. The combined power requirement for refrigeration and pumping is much lower than for the pure vapor compression, but there are significant challenges due to system complexity. In addition the liquid CO_2 transport may not be as efficient as gas pipeline transport.

Another area of research is the use of supercritical CO_2 in Brayton cycle applications [11–13]. Due to the liquid-like density and specific heat capacity of the fluid, it has the potential to reduce the weight and increase the power conversion efficiency of the system. The focus of the work in literature however is mostly on cycle developments. Several research labs, including Sandia National Laboratory [14], operate test loops to demonstrate the feasibility of the concept and investigate the system performance and characteristics. A discussion on deriving the turbomachinery specifications from the cycle analysis is presented by Fuller at al [15], while a 2D through-flow model for the design of supercritical CO_2 turbomachinery is proposed by Lee et al [16]. The methodology aims to integrate different empirical loss models developed for conventional turbomachinery with a real gas equation of state to establish the stage geometry and the performance maps. The drawback of this approach is that it fails to capture the impact of the real gas effects on the different loss mechanisms. Numerical simulation of a centrifugal compressor stage operating with CO_2 in the vicinity of the critical point is presented by Pecnik et al [17]. The paper however focuses on validating the numerical schemes and the interaction between the solver and the real gas model. It lacks depth in the analysis of the compressor performance and of its departure from ideal gas behavior.

1.4 Goals and Objectives

The goal of this thesis is to describe in a rigorous manner the impact of real gas effects on the internal flow behavior of supercritical CO_2 and the implications for the design and analysis of centrifugal stages employed in CCS. The main objectives of this work are to:

- Examine the differences between ideal and real gas compressible flow theory and apply first principles based modeling to identify trends in the gas dynamic behavior, not observed in ideal fluids,
- give insight into the root cause and the mechanisms responsible for the performance and operability issues observed in CO_2 compressors operating at supercritical conditions,
- quantify the impact of real gas effects on the compressor performance characteristics and stage matching using targeted numerical simulations,
- assess the possibility of condensation in the compressor stage and establish a non-dimensional criterion to determine the significance of two-phase flow effects for the compressor operation.

The potential payoffs include improved assessment of compressor performance and engineering margins, leading to a reduction in development costs and in-field problems. Given the large scale of future markets, this could be a key step towards making CCS an economically viable process.

1.5 Technical Roadmap

The gap between current design practices and technological needs is illustrated in Fig. 1-4. Real gas EOS models are used to scale existing stage designs for use with supercritical fluids, but what is missing is a fundamental investigation of the behavior of these fluids in internal flow situations. Successful description of the real gas internal flow processes could be the basis for an advanced compressor design methodology. A

systematic approach is proposed, starting with an assessment of different real gas models to be used with numerical simulation codes. The level of fidelity in the calculations is gradually increased from 2D steady canonical flow situations to 3D unsteady simulation of an actual compressor stage. At each level of assessment, experimental work is proposed to validate the methods and the key findings. The technological roadmap, described by Fig. 1-5, allows for an improved assessment of compressor performance leading to stage designs tailored to the non-conventional working fluid.

A detailed comparison between different EOS models is presented in Chapter 2 to identify the most appropriate for the range of operating conditions in the vicinity of the critical point. A short description of the implementation of the real gas models in various CFD tools is also included. Chapter 3 focuses on the thermodynamics of real fluids. A review of basic thermodynamic relations is presented, followed by a generalized formulation of compressible flow relations valid for both real and ideal gas. Significant attention is given to the implications of the variation of real gas properties on compressible flow, specifically on the corrected mass flow per unit area. These concepts are validated with numerical simulations of a converging nozzle and several hypotheses regarding the impact of real gas effect on compressor performance and matching are established.

Further assessment of the behavior of supercritical CO_2 in turbomachinery environment is presented in Chapter 4. A 2D radial blade row is used to make a comparison between atmospheric air, air at high pressure (typical of CO_2 compressors), ideal gas CO_2, and real gas CO_2. Numerical simulations are extended to the actual 3D geometry of a centrifugal compressor stage at the operating conditions typical of CO_2 compressor applications.

In Chapter 5, the possibility of condensation due to local flow acceleration around the impeller leading edge is assessed. A summary of the loss mechanisms associated with condensation is given, followed by numerical calculations to quantify its impact on the flow field. A non-dimensional criterion is established that determines whether two-phase flow effects are present in the flow. In Chapter 6, real gas CFD simulations

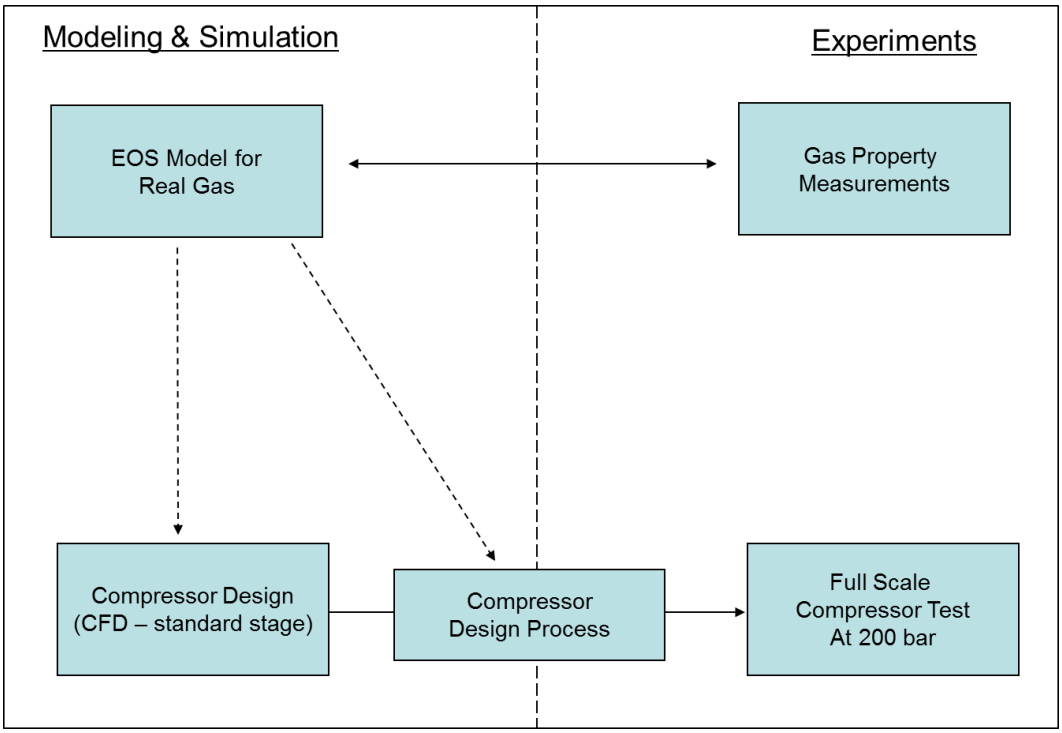

Figure 1-4: Technological gap in CO_2 compressor design process.

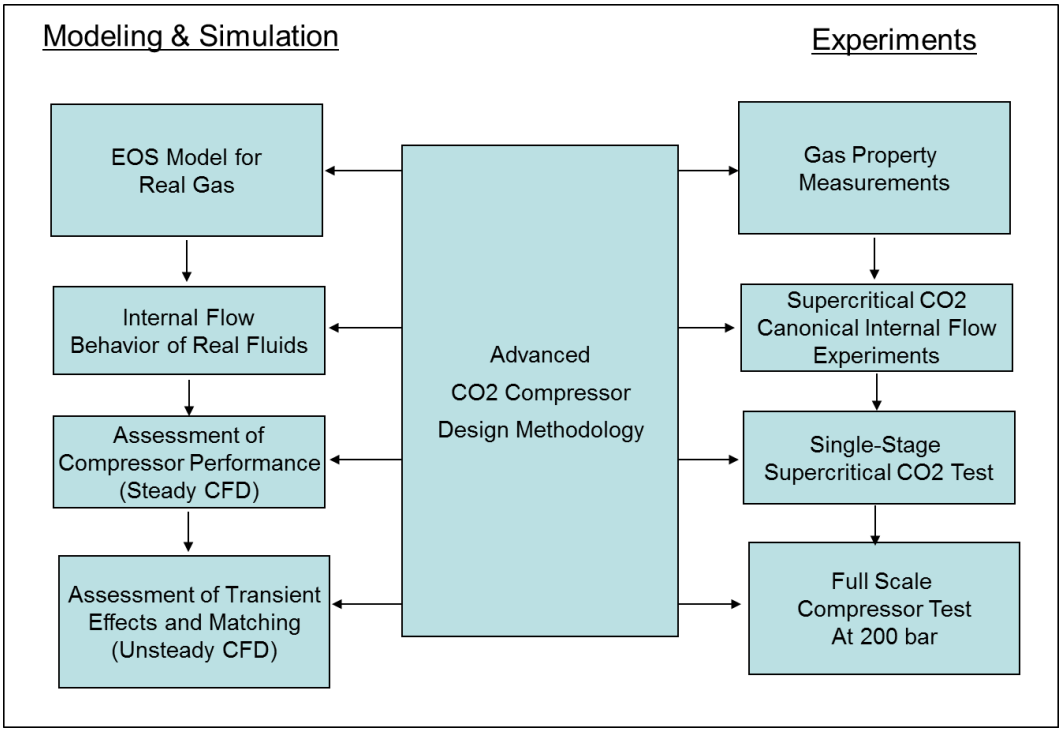

Figure 1-5: Proposed technological roadmap.

are extended from the current operating conditions of the compressor to conditions approaching the empirical safety limit. The objective is to investigate changes in performance and operating range. Finally, a summary of the key contributions and findings, as well as recommendations for future work are presented in Chapter 7.

1.6 Key Contributions

The approach described in the previous section allows for the rigorous assessment of the impact of real gas effects on supercritical CO_2 compressors. The contributions of this thesis can be summarized as follows.

1. The influence coefficients for compressible channel flow and the corrected mass flow per unit area are derived for real gas and used to examine trends in the internal flow behavior of real fluids. The variation in real gas properties of CO_2 near the critical point and the local flow expansion through the vapor-pressure curve are identified as possible mechanisms for performance and operability issues.

2. At the current operating conditions of the candidate stage, real gas effects are found to have no significant impact on the performance and matching of centrifugal compressor stages. Furthermore, the compressor performance can be adequately modeled using ideal gas, provided that dynamic similarity with the real fluid conditions is preserved.

3. Approaching the critical point, numerical calculations show a 9% reduction in the choke margin of the candidate stage due to the variation in real gas properties. The swing in corrected mass flow from inlet to outlet of the stage also increases by 5% relative to the design conditions, which may lead to significant matching problems for the downstream components.

4. Based on the established non-dimensional criterion, it is shown that condensation is not a concern for the candidate compressor stage at its current operating

conditions. In the vicinity of the critical point however, the conditions for liquid droplet formation may be achieved and the impact on compressor performance needs to be further assessed.

While the work in this thesis focuses on supercritical CO_2 compressors for carbon capture and sequestration, the analytical methods and techniques presented here are directly applicable to other non-conventional fluids and applications.

Chapter 2

Modeling of Supercritical CO_2 Properties

The properties of carbon dioxide have been studied extensively in the past because of its widespread occurrence and importance form both an engineering and scientific standpoint. In chemistry, its significance results from being one of the main products of hydrocarbon combustion and a greenhouse gas. More recently CO_2 has been extensively used in CCS and EOR, raising concerns not only about its behavior in fluid machinery but also its chemical stability at the storage conditions in the earth's outer mantle. In engineering it is commonly used as a test fluid for calibration purposes due to the relative abundance of measurement data. These applications cover a wide range of pressures and temperatures where CO_2 exhibits substantial deviations from ideal gas behavior. The location of the critical point ($T_c = 304.21\,\mathrm{K}$, $p_c = 73.773\,\mathrm{bar}$) allows for many processes to be carried out in its vicinity. This region is characterized by relatively high density, similar to a liquid, while the fluid still expands to fill up a volume, just like a gas does. Viscosity and thermal conductivity are diminishingly small, while specific heat capacity is asymptotically approaching a value that is over 10 times larger than that of water. Such violent fluctuations present significant challenges for modeling thermodynamic properties.

2.1 Literature Overview

A variety of EOS models exist with variable accuracy depending on the particular range of thermodynamic states of interest. A study by Lüdtke [18] compares three of the most common real gas models: the Benedict, Webb, and Rubin (1940) formulation with extension by Sterling (1973) referred to as BWRS; the formulation by Redlich and Kwong (1949) augmented by Soave (1972) known as RKS model; and the Lee and Kesler model (1975) modified by Ploker, Knapp, and Prausnitz (1978) referred to as LKP model. Compressibility factors calculated using these models were compared against gas property tables published in the 1960s and 1970s for selected fluids. The study found that for CO_2 at pressures between 50 bar and 250 bar the LKP model had the best agreement with experimental data, with deviation of less than 2%. The BWRS model had significantly worse agreement of up to 5%, while the RKS model was not recommended at all.

A more recent equation of state model, particularly tailored for carbon dioxide was developed by Span and Wagner (1996) (SW) [19], whose accuracy is shown to be on the same order as the uncertainty of the experimental measurements, which is 0.05% for density. The Lee-Kesler (LK) [20] model is well-established and widely used in industry, while the SW model has recently gained popularity, mainly in science and research, due to emerging new applications for supercritical CO_2. Descriptions of the strengths and weaknesses of both EOS models are presented in this chapter, including a comparison between the two in the supercritical region together with a discussion of their application to CFD simulations.

2.2 The Lee-Kesler Model

The main objective of the LK EOS model was to improve the accuracy of existing real gas models, particularly in the subcooled liquid and superheated vapor regions. The model is based on the 3-parameter corresponding states principle, where thermodynamic properties are represented as a linear function of acentric factor at constant

reduced temperature, $T_r = T/T_c$, and pressure, $p_r = p/p_c$. The acentric factor is a dimensionless parameter that serves as a measure for the non-sphericity of a given substance's molecule. The form of the function is

$$Z = Z^{(0)} + \frac{\omega}{\omega^{(r)}}(Z^{(r)} - Z^{(0)}) \quad . \tag{2.1}$$

The compressibility factor of the real fluid, Z, with acentric factor, ω, is a weighted summation of the compressibility factors of a simple fluid, denoted by superscript $^{(0)}$ and $\omega^{(0)} = 0$, and a reference fluid denoted by superscript $^{(r)}$. The terms $Z^{(0)}$ and $Z^{(r)}$ are represented by the same empirically derived equation in terms of reduced pressure and temperature, but with different sets of coefficients. The general form of the equation is

$$Z^{(0),(r)} = \left(\frac{p_r v_r}{T_r}\right) = 1 + \frac{B}{v_r} + \frac{C}{v_r^2} + \frac{D}{v_r^5} + \frac{c_4}{T_r^3 v_r^2}\left(\beta + \frac{\gamma}{v_r^2}\right) e^{\left(-\frac{\gamma}{v_r^2}\right)} \quad . \tag{2.2}$$

The term v_r is not the actual reduced volume. In this correlation it is defined as $v_r = p_c v/RT_c$. For a given reduced temperature and pressure it can be calculated for the simple and reference fluids using Eq. 2.2. The remaining terms on the right hand side of Eq. 2.2 are empirically determined constants using measurements of argon ($\omega = 0.04$), krypton ($\omega = 0.02$), and methane ($\omega = 0.08$) for the simple fluid, and n-Octane ($\omega = 0.398$) for the reference fluid. From the equation of the compressibility factor Z, the authors also derive other important thermodynamic functions including the departures from ideal gas of enthalpy, entropy, isobaric and isochoric specific heat capacities, as well as the derivatives $\left(\frac{\partial p_r}{\partial v_r}\right)_{T_r}$ and $\left(\frac{\partial p_r}{\partial T_r}\right)_{v_r}$. These derivatives reduce to trivial expressions ($-\frac{p_r}{v_r}$ and $\frac{p_r}{T_r}$ respectively) when working with an ideal gas and are generally disregarded. Their significance for real fluids is discussed in Chapter 3.

In this study, the LK model is implemented as a stand-alone subroutine in MatLab that is used to provide real gas properties of CO_2 in CFD calculations. The subroutine is validated against tabulated data from the original paper by Lee and Kesler. More details on the implementation of the model are given in Section 2.6. It must be noted here that during the process, a typographical error was uncovered in the equation for

$\left(\frac{\partial p_r}{\partial T_r}\right)_{v_r}$. Equation (15) as published in the paper reads

$$\left(\frac{\partial p_r}{\partial T_r}\right)_{v_r} = \frac{1}{v_r}\left\{1 + \frac{b_1 + b_3/T_r^2 + 2b_4/T_r^3}{v_r} + \frac{\mathbf{c_1 - 2c_3/T_r^3}}{\mathbf{2v_r^2}} + \frac{\mathbf{d_1}}{\mathbf{5v_r^5}} - \frac{2c_4}{T_r^3 v_r^2}\left[\left(\beta + \frac{\gamma}{v_r^2}\right)e^{\left(-\frac{\gamma}{v_r^2}\right)}\right]\right\} \tag{2.3}$$

However two of the terms appear to have mistyped coefficients. The proper form of the equation is provided below, with the corrections marked in bold.

$$\left(\frac{\partial p_r}{\partial T_r}\right)_{v_r} = \frac{1}{v_r}\left\{1 + \frac{b_1 + b_3/T_r^2 + 2b_4/T_r^3}{v_r} + \frac{\mathbf{c_1 - 2c_3/T_r^3}}{\mathbf{v_r^2}} + \frac{\mathbf{d_1}}{\mathbf{v_r^5}} - \frac{2c_4}{T_r^3 v_r^2}\left[\left(\beta + \frac{\gamma}{v_r^2}\right)e^{\left(-\frac{\gamma}{v_r^2}\right)}\right]\right\} \tag{2.4}$$

Even though the Lee-Kesler equation of state was targeted primarily towards modeling the properties of hydrocarbons, it is shown to have good agreement with experimental data for other fluids, including CO_2 [18, 21]. The average error in compressibility factor for CO_2 reported in [21] is 1.18% with a maximum error of 5.84% in the immediate vicinity of the critical point ($T_r = 0.99$ and $p_r = 0.95$). Even though the LK model has diminishing accuracy near the critical point, especially in derived properties such as specific heats or speed of sound, to the author's knowledge there is no published comparison of these properties with experimental data. To quantify the error in the derived properties, a detailed comparison of the LK model to data obtained from the National Institute of Standards and Technology (NIST) for CO_2 is presented in Section 2.5.

2.3 The Span-Wagner Model

The LK model, as well as the preceding EOS models, has two fundamental deficiencies. It is developed as a generalized model, using data from several reference fluids to

describe the behavior of a wide range of substances. Furthermore, it uses only p-v-T data to model the compressibility factor, leading to a reduced accuracy in the rest of the properties. To overcome these issues, the SW model employs a completely different approach focusing specifically on CO_2. The equation of state is represented as a fundamental equation in terms of the Helmholtz energy, A, in non-dimensional form

$$A(\rho,T)/(RT) = \phi(\delta,\tau) = \phi^o(\delta,\tau) + \phi^r(\delta,\tau) \quad . \tag{2.5}$$

The two terms on the right hand side represent the ideal gas contribution, denoted by a superscript ^{o}, and residual fluid contribution, denoted by a superscript ^{r}. The two independent variables are reduced density, $\delta = \rho/\rho_c$, and inverse reduced temperature, $\tau = T_c/T$. The remaining thermodynamic properties can be expressed as functions of the Helmholtz energy and its derivatives with respect to temperature and density. For example, the compressibility factor Z can be written as

$$Z(\rho,T) = 1 + \delta\phi^r_\delta \quad , \tag{2.6}$$

where

$$\phi_\delta = \left(\frac{\partial\phi}{\partial\delta}\right)_\tau \quad .$$

The ideal gas contribution is treated almost entirely analytically. The only empirical contribution is coming from the expression of the ideal gas specific heat c_p^o as a function of temperature. The expression for ϕ^o is of the form

$$\phi^o(\delta,\tau) = ln(\delta) + a_1^o + a_2^o\tau + a_3^o ln(\tau) + \sum_{\eta=4}^{8} a_i^o ln\left[1 - e^{(-\tau\theta_i^o)}\right] \tag{2.7}$$

where the coefficients a_i^o and θ_i^o are coming from the expression for c_p^o. In contrast to the ideal gas part, the residual part of the Helmholtz energy is determined empirically using experimental measurements. Since it is impossible to directly measure this property, the authors propose a complicated procedure to establish an empirical

correlation between the Helmholtz energy and experimental measurements of thermodynamic properties including p-v-T data, as well as internal energy, enthalpy, entropy, isochoric and isobaric specific heat capacities, speed of sound, and other properties. The authors reviewed the available data sets on CO_2 property measurements dating back as far as 1903 and divide them into 3 categories: data sets used for development of empirical correlations, data sets suitable for comparison, and data sets that do not meet the required levels of uncertainty or the level of uncertainty could not be determined. This ensures that the resulting formulation can model secondary properties without diminishing accuracy due to inappropriate data fitting. The expression for ϕ^r is of the form

$$\begin{aligned}\phi^r(\delta,\tau) &= \sum_{\eta=1}^{7} n_i \delta^{d_i} \tau^{t_i} + \sum_{\eta=8}^{34} n_i \delta^{d_i} \tau^{t_i} e^{(-\delta^{c_i})} \\ &+ \sum_{\eta=35}^{39} n_i \delta^{d_i} \tau^{t_i} e^{\left[-\alpha_i(\delta-\epsilon_i)^2-\beta_i(\tau-\gamma_i)^2\right]} \\ &+ \sum_{\eta=40}^{42} n_i \Delta^{b_i} \delta e^{\left[-C_i(\delta-1)^2-D_i(\tau-1)^2\right]} \end{aligned} \tag{2.8}$$

The last terms (n = 40 to 42) represent the effect of the critical point, with Δ being an exponential function that damps their influence outside the critical region. All the coefficients in Equation 2.8 can be found in [19]. The reported uncertainty of the model ranges from 0.03% to 0.05% in density, 0.03% to 1% in speed of sound, and 0.15% to 1.5% in isobaric heat capacity. This state-of-art model is used by NIST within its database of thermodynamic properties of various substances, called REFPROP, to reference properties of CO_2, supplemented by auxiliary models for the transport properties described in the following section.

2.4 Transport Properties

Auxiliary models for viscosity and thermal conductivity are based on the publication by Vesovic et. al. [22], with an extension for viscosity by Fenghour et. al. [23]. The properties are represented as the sum of three terms: the zero-density limit of the property, an excess term representing the effects of increased density, and a critical enhancement term due to increased fluctuations in the vicinity of the critical point.

$$X(\rho, T) = X^o(T) + \Delta X(\rho, T) + \Delta_C X(\rho, T) \tag{2.9}$$

All three terms are empirically derived functions of temperature and density. While the zero-density limit and the excess property have relatively straight-forward formulations as the sum of several terms with different constant coefficients and exponents, the critical enhancement term presents a much more significant challenge. Very few reliable experimental measurements of the transport properties exist close to the critical point, where the singular behavior of these properties require the use of crossover functions to blend with the smooth behavior away from this region. The critical enhancement term is found to be explicitly dependent on temperature and density, but also implicitly dependent on the correlation length of the density fluctuations (ξ) which diverges at the critical point and requires a complicated iterative procedure to calculate. The critical enhancement term has a weaker impact on viscosity compared to thermal conductivity, and is restricted to a much smaller region. The critical viscosity enhancement accounts for more than 1% of the overall viscosity in the range of temperatures and densities bounded by $300\,\mathrm{K} < T < 310\,\mathrm{K}$ and $300\,{}^{\mathrm{kg}}/_{\mathrm{m}^3} < \rho < 600\,{}^{\mathrm{kg}}/_{\mathrm{m}^3}$. In the case of thermal conductivity the bounds of this region extend to $240\,\mathrm{K} < T < 450\,\mathrm{K}$ and $25\,{}^{\mathrm{kg}}/_{\mathrm{m}^3} < \rho < 1000\,{}^{\mathrm{kg}}/_{\mathrm{m}^3}$. Over most of the gas phase, the deviation of the model compared to experimental data does not exceed 2%. Maximum error is observed in the liquid phase for the thermal conductivity of about 5%.

2.5 Comparison of EOS Models

To understand the full scope and limitations of the LK model for CO_2, a detailed comparison against data obtained from NIST's REFPROP database [24] is presented here. The comparison is performed entirely in the supercritical region for a range of pressures between 74 bar and 203 bar, and temperatures between 304 K and 433 K. The relative error is calculated using

$$error = \frac{\mid X_{LK} - X_{NIST} \mid}{X_{NIST}} \quad . \tag{2.10}$$

Table 2.1 summarizes the results in terms of maximum and RMS errors for the specified range.

Property	Max. Rel. Error	RMS Rel. Error
Density	7.72%	0.999%
Specific Volume	7.17%	1.01%
Enthalpy	2.41%	1.21%
Entropy	1.65%	0.842%
Internal Energy	2.49%	1.35%
c_p	70.7%	4.16%
c_v	37.6%	5.33%
Speed of Sound	43.0%	3.35%
Joule-Thompson	10.6%	2.88%
Viscosity	6.37%	0.974%

Table 2.1: Comparison of Lee Kesler model to NIST data.

All the primary properties (density, enthalpy, entropy, and internal energy) are modeled accurately with an average discrepancy of about 1%, which is in agreement with [18, 21]. The maximum error in all properties occurs in the immediate vicinity of the critical point. The LK model is unable to capture the singular behavior of the fluid at this point and the resulting error in the primary properties gets amplified

by an order of magnitude in the derived properties. This substantial deviation near the critical point drives a misleadingly high value of the average error. To better understand the limitations of the LK model it is useful to look at the distribution of the relative error in a primary property (density) and a derived property (isobaric specific heat capacity).

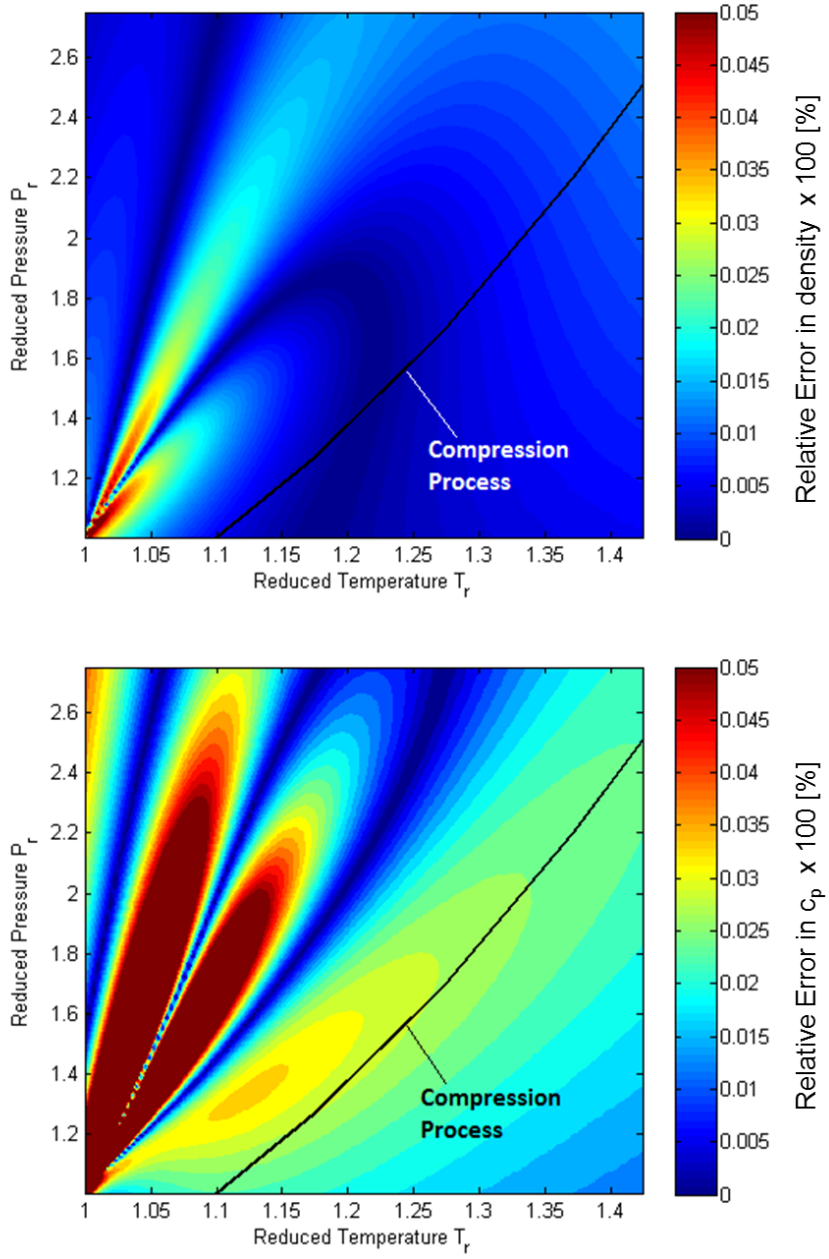

Figure 2-1: Relative error in density and isobaric specific heat capacity.

The black line in Fig. 2-1 represents the operating states of the compressor introduced in Chapter 1. The contours are clipped at 5% to illustrate the region where the accuracy of the LK model begins to diminish. For density this region is limited to the immediate vicinity of the critical point, while for the specific heat capacity it extends into the so-called "pseudo-critical" region where the fluid behavior begins to asymptotically approach the singularity at the critical point. In the operating range of the compressor however, the difference between the LK and SW models is less than 2.5% in all derived properties.

2.6 Implementation

The SW EOS model is available for use in CFD simulations through the REFPROP database. In this study, the LK EOS model is implemented as a User-Defined Real Gas Model (UDRGM) through the MatLab subroutine. In a single iteration the solver will call the UDRGM numerous times, so the numerical efficiency of the scheme has direct impact on the computational cost of a simulation.

Even though the LK model has relatively simpler formulation compared to the SW model, the non-linear form of Eq. 2.2 requires an iterative approach to solve. The function is continuous and differentiable, which allows for the application of the Newton-Raphson method. This method is preferred because of its straightforward expression and fast, generally quadratic, convergence. Special consideration must be given to the region bounded by $T_r < 1$ and $p_r < 1$, where Eq. 2.2 can have non-physical solutions inside the two-phase dome. An adequate initial guess for the Newton-Raphson method can be obtained with the ideal gas law to avoid non-physical roots of the equation and to enhance convergence.

This approach improves the computational time of a CFD simulation in Fluent by a factor of five compared to the built-in REFPROP database. The level of accuracy of the LK model in the vicinity of the operating range of the compressor provides a good representation of the flow field inside the machine. The results from the numerical calculations are discussed in the following chapters.

2.7 Summary

This chapter provides a brief literature review of the available work on modeling supercritical CO_2 properties. The Lee-Kesler and Span-Wagner models are identified as the most suitable EOS models for the range of thermodynamic conditions where the compressor introduced in Chapter 1 operates. The LK model is based on the 3-parameter corresponding states principle, where data from several different fluids is used to develop a general correlation that is applicable over a wide range of states. Its main drawback is the diminishing accuracy in the vicinity of the critical point, particularly in derived properties. The SW model on the other hand is developed specifically for CO_2. The empirical correlation is optimized to fit experimental measurements of p-v-T data, enthalpy, entropy, speed of sound, and other properties. Special treatment of the critical region is considered to ensure that the highly nonlinear behavior of the fluid in that region is captured appropriately. The accuracy of the model is reported to be within the experimental uncertainty of the data.

Comparison of the two models shows that they are in good agreement in the vicinity of the operating range of the compressor, as shown in Fig. 2-1. The average relative error in the LK model compared to the SW is found to be less than 1% in primary properties, such as density, and less than 2.5% in derived properties, such as c_p. All CFD calculations presented in this thesis employ the Lee-Kesler equation of state, since the thermodynamic conditions are within the acceptable range for this model. For simulations that extend closer to the critical point however, the use of the Span-Wagner model is recommended.

Chapter 3

Real Gas Thermodynamics

Before conducting detailed flow investigations using CFD, it is important to establish some useful real gas thermodynamic relations and to examine the departure from ideal gas theory. The non-ideal state of the fluid gives rise to a set of derived properties that impact the governing equations of compressible flow of real fluids. Studying the behavior of these properties can help identify various real gas phenomena and provide insight into the operation of a compressor stage. The principle of corrected mass flow per unit area is used to establish hypotheses for the impact of real gas effects on compressor performance and stage matching.

3.1 The Non-Ideal Fluid

3.1.1 Compressibility Factor

The compressibility factor can be interpreted as a measure of the fluid's deviation from ideal gas behavior and can be expressed as $Z = v/v_{ideal}$, where $v_{ideal} = RT/p$. However, Z only gives the magnitude of the deviation. There are two additional state variables that determine the relative change in specific volume with respect to pressure at constant temperature (isothermal compressibility) and with respect to temperature at constant pressure (isobaric compressibility). The definitions of these properties and their expressions for an ideal gas are summarized in Table 3.1.

Property	Definition	Ideal Gas Case
Compressibility factor	$Z = f(T, p)$	$Z = 1$
Isothermal compressibility	$\beta_T = -\frac{1}{v}\left(\frac{\partial v}{\partial p}\right)_T = \frac{1}{p} - \frac{1}{Z}\left(\frac{\partial Z}{\partial p}\right)_T$	$\beta_T = \frac{1}{p}$
Isobaric compressibility	$\beta_p = \frac{1}{v}\left(\frac{\partial v}{\partial T}\right)_p = \frac{1}{T} + \frac{1}{Z}\left(\frac{\partial Z}{\partial T}\right)_p$	$\beta_p = \frac{1}{T}$

Table 3.1: Compressibility functions for real gas.

When dealing with ideal fluids, these state variables are usually disregarded due to their trivial formulation, but they must be accounted for in many thermodynamic relations for real gases.

3.1.2 Caloric Equation of State

Another important difference from a perfect gas is that enthalpy is a function of both pressure and temperature. This is illustrated for CO_2 in a T-s diagram in Fig. 3-1.

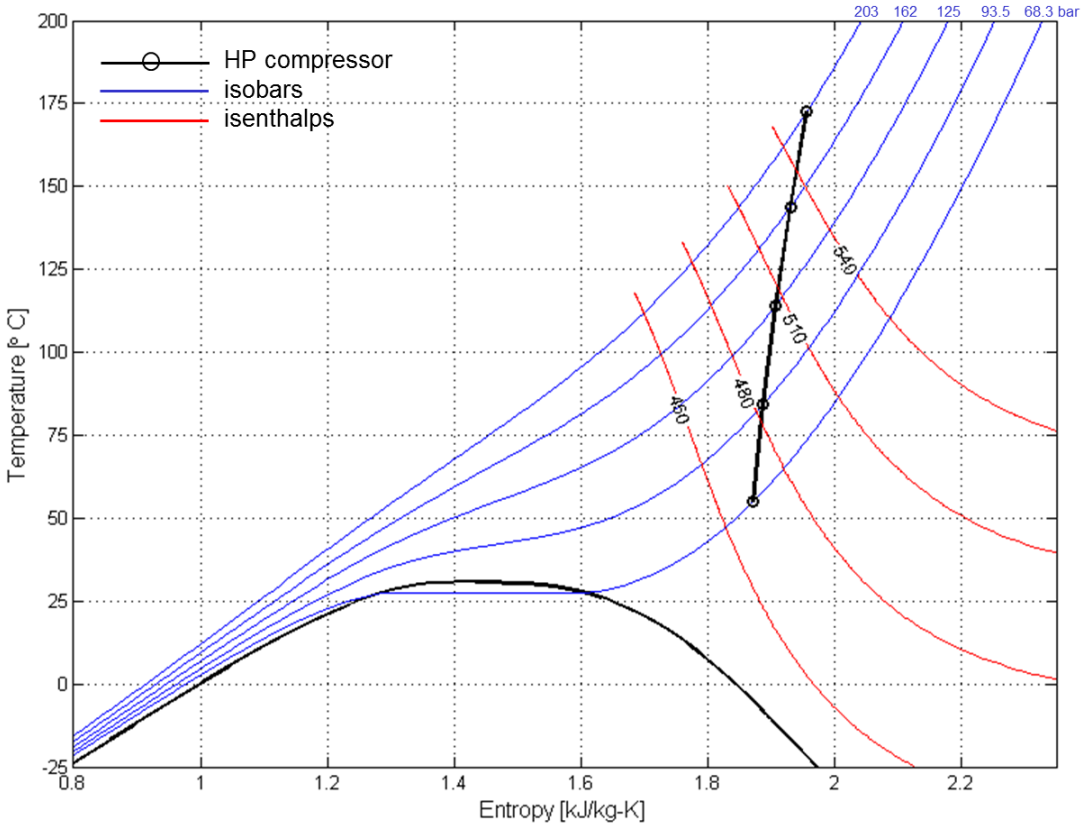

Figure 3-1: Dependence of enthalpy on pressure and temperature for CO_2.

This effect is described by the Joule-Thomson coefficient, which is defined as $J_t = \left(\frac{\partial T}{\partial p}\right)_h$. For an ideal gas $J_t = 0$ and enthalpy is only a function of temperature. For CO_2 at supercritical and near-critical conditions the isenthalps exhibit strong dependence on pressure and temperature, as shown in Fig. 3-1. Consequently, the relationship $dh = c_p dT$ is not valid for a real gas and the more fundamental caloric equation of state must be considered

$$dh = \left(\frac{\partial h}{\partial T}\right)_p dT + \left(\frac{\partial h}{\partial p}\right)_T dp \ . \tag{3.1}$$

By definition $c_p = \left(\frac{\partial h}{\partial T}\right)_p$, while the second partial derivative can be rewritten using the Maxwell relations, shown in Appendix A, as

$$\left(\frac{\partial h}{\partial p}\right)_T = v - T\left(\frac{\partial v}{\partial T}\right)_p \ . \tag{3.2}$$

Substituting the expressions for the two derivatives in Eq. 3.1 yields

$$dh = c_p dT + \left[v - T\left(\frac{\partial v}{\partial T}\right)_p\right] dp = c_p dT + v\left(1 - \beta_p T\right) dp \ . \tag{3.3}$$

If the ideal gas form of the isobaric compressibility is substituted in Eq. 3.3, the pressure dependence term vanishes, and the relationship reduces to the familiar expression for a perfect gas. The caloric equation of state can also be expressed in terms of $u(T, v)$

$$du = \left(\frac{\partial u}{\partial T}\right)_v dT + \left(\frac{\partial u}{\partial v}\right)_T dv \ . \tag{3.4}$$

Similar to the relationship for enthalpy, Eq. 3.4 can be rewritten as

$$du = c_v dT + \left[T\left(\frac{\partial p}{\partial T}\right)_v - p\right] dv = c_v dT + p\left(\frac{\beta_p T}{\beta_T p} - 1\right) dv \ . \tag{3.5}$$

In the case of a perfect gas, Eq. 3.5 reduces to $du = c_v dT$.

3.2 Isentropic Relations

For an ideal gas the isentropic process in p-v coordinates is described by $pv^{\gamma} = const.$ It can be shown that in the case of a real fluid, the isentropic exponent involves also the isothermal compressibility in addition to the specific heat ratio. Substituting γ with the general term n_s and rewriting the expression of an isentrope in differential form gives

$$\frac{dp}{p} + n_s \frac{dv}{v} = 0 \Big|_{s=const} \quad . \tag{3.6}$$

Rearranging the terms yields an equation for n_s

$$n_s = -\frac{v}{p}\left(\frac{\partial p}{\partial v}\right)_s \tag{3.7}$$

Eq. 3.7 can be expressed in terms of the isothermal compressibility and specific heat ratio by using the Maxwell relations and the cyclic relation rule. A review of these is also provided in Appendix A. Expressing entropy as function of temperature and pressure yields

$$ds = \left(\frac{\partial s}{\partial T}\right)_p dT + \left(\frac{\partial s}{\partial p}\right)_T dp \quad . \tag{3.8}$$

Alternatively, combining Gibbs' equation

$$dh = Tds + vdp \tag{3.9}$$

with Eq. 3.3 yields another relationship for ds

$$ds = \frac{c_p}{T} dT - \left(\frac{\partial v}{\partial T}\right)_p dp \quad . \tag{3.10}$$

Comparing Eq. 3.8 to 3.10 shows that $\frac{C_p}{T} = \left(\frac{\partial s}{\partial T}\right)_p$. Using the cyclic rule and the Maxwell relation for $\left(\frac{\partial p}{\partial s}\right)_T$ gives

$$\frac{c_p}{T} = \left(\frac{\partial p}{\partial T}\right)_s \left(\frac{\partial v}{\partial T}\right)_p \quad . \tag{3.11}$$

An expression for c_v can be obtained in a similar fashion by considering $s(T, v)$ and comparing it to Eq. 3.4 yielding

$$\frac{c_v}{T} = -\left(\frac{\partial p}{\partial T}\right)_v \left(\frac{\partial v}{\partial T}\right)_s \quad . \tag{3.12}$$

Combining the two equations for the specific heats and applying the cyclic rule one more time gives

$$\gamma = \frac{c_p}{c_v} = \frac{(\partial p/\partial v)_s}{(\partial p/\partial v)_T} \tag{3.13}$$

or equivalently

$$-\frac{v}{p}\left(\frac{\partial p}{\partial v}\right)_s = -\gamma\frac{v}{p}\left(\frac{\partial p}{\partial v}\right)_T = \frac{\gamma}{\beta_T p} \quad . \tag{3.14}$$

Substituting Eq. 3.14 into 3.7 yields a relation for the isentropic exponent

$$n_s = \frac{\gamma}{\beta_P T} \quad . \tag{3.15}$$

The expression of an isentrope can be derived also in T-p coordinates involving a different exponent, where $Tp^{-m_s} = const.$ This derivation is provided in Appendix A, and the final form of both exponents and their ideal gas equivalents are summarized in Table 3.2.

Isentropic exponent	General Expression	Ideal Gas Case
Pressure exponent	$n_s = \frac{\gamma}{\beta_T p}$	$n_s = \gamma$
Temperature exponent	$m_s = \frac{\gamma-1}{\gamma}\frac{\beta_T p}{\beta_p T}$	$m_s = \frac{\gamma-1}{\gamma}$

Table 3.2: Isentropic exponents for real gas.

Table 3.2 gives one example of the importance of the compressibility functions β_T and β_p and the need for an appropriate EOS model that accurately evaluates

these derived properties. Another significant implication of the different form of the isentropic exponent is observed in the expression for the speed of sound of a real gas. By definition

$$a^2 = \left(\frac{\partial p}{\partial \rho}\right)_s = -v^2 \left(\frac{\partial p}{\partial v}\right)_s \quad . \tag{3.16}$$

Substituting Eq. 3.14 in 3.16 and taking the square root yields

$$a = \sqrt{n_s p v} = \sqrt{n_s Z R T} \quad . \tag{3.17}$$

For a real fluid the speed of sound is not a function of temperature alone, as is the case for a perfect gas. It has a secondary pressure and temperature dependence through the isentropic exponent and the compressibility factor. In certain dense gases, this secondary dependence can cause the speed of sound to increase even when the temperature is decreasing, leading to inversion of gas dynamic behavior. This phenomenon is described in greater detail in Section 3.5.

3.3 Compressible Internal Flow

The fundamental difference in compressible flow theory between ideal and real gas can be illustrated with the fanno flow example sketched on Fig. 3-2. For an adiabatic

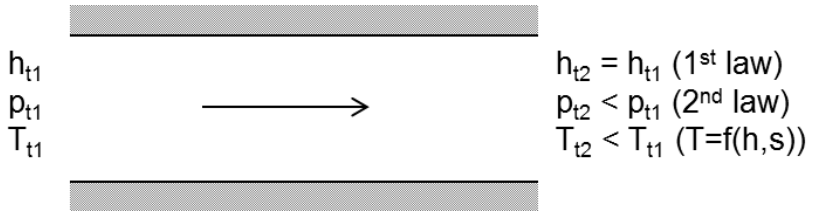

Figure 3-2: Fanno flow for real gas.

flow with friction, the total enthalpy is conserved per the 1^{st} law of thermodynamics, while total pressure decreases from inlet to outlet due to viscous losses per the 2^{nd} law of thermodynamics. If enthalpy is a function of temperature and pressure as discussed in Section 3.1, total temperature must decrease as well. Contrary to ideal

gas theory, the adiabatic condition is not a sufficient condition to define stagnation temperature. In the general case of a real gas, stagnation temperature must be defined as the temperature of a fluid decelerated to zero velocity in an adiabatic, reversible process, similar to the definition of stagnation pressure.

3.3.1 Stagnation Properties

Applying the condition of reversibility ($ds = 0$) to Eq. 3.10 yields a relationship between pressure and temperature for an isentropic process

$$c_p dT = (v\beta_p T)\, dp|_{s=const} \quad . \tag{3.18}$$

This relation can be employed with Eq. 3.3 to express dh as the derivative of temperature or pressure alone.

$$dh = \frac{c_p}{\beta_p T} dT \bigg|_{s=const} \tag{3.19}$$

$$dh = v dp|_{s=const} \tag{3.20}$$

The latter can also be derived by applying the isentropic condition directly to Eq. 3.9. Either equation can be integrated to obtain the relationships between total and static properties. In this section the process is carried out using Eq. 3.20 and the alternative is shown in Appendix A

$$\int_h^{h_t} dh = \int_p^{p_t} v dp \quad . \tag{3.21}$$

The LHS of Eq. 3.21 is relatively straight-forward to integrate and using the definitions of total enthalpy, Mach number, and Eq. 3.17 it can be rewritten as:

$$\int_h^{h_t} dh = h_t - h = \frac{c^2}{2} = \frac{(aM)^2}{2} = \frac{M^2}{2} n_s p v \quad . \tag{3.22}$$

The RHS of Eq. 3.21 can be expressed in terms of pressure by relating total and static conditions through the equation for an isentropic process in p-v coordinates

$$p_t v_t^{n_{s,t}} = p v^{n_s} \quad . \tag{3.23}$$

Before the integration can be performed however, the assumption is made that the isentropic exponent remains constant from total to static conditions. Away from the critical point, the variations in n_s are small enough such that an average value between total and static conditions can be used. The validity of this assumption is further examined in Section 3.6. Integrating the RHS of Eq. 3.21 yields

$$\int_p^{p_t} v_t \left(\frac{p_t}{p}\right)^{1/n_s} dp = v_t p_t \left[1 - \left(\frac{p}{p_t}\right)^{\frac{n_s-1}{n_s}}\right] \frac{n_s}{n_s - 1} \quad . \tag{3.24}$$

Equating the two sides of Eq. 3.21 gives

$$\frac{M^2}{2} = \frac{v_t p_t}{v p} \left[1 - \left(\frac{p}{p_t}\right)^{\frac{n_s-1}{n_s}}\right] \frac{1}{n_s - 1} \quad . \tag{3.25}$$

Using Eq. 3.23 to express Eq. 3.25 in terms of pressure ratio and rearranging the terms yields the final form of the isentropic relation for stagnation pressure

$$\frac{p_t}{p} = \left(1 + \frac{n_s - 1}{2} M^2\right)^{\frac{n_s}{n_s-1}} \quad . \tag{3.26}$$

The rest of the relations follow directly from the expressions of an isentropic process in T-p and p-v coordinates.

$$\frac{T_t}{T} = \left(1 + \frac{n_s - 1}{2} M^2\right)^{\frac{m_s n_s}{n_s-1}} \tag{3.27}$$

$$\frac{\rho_t}{\rho} = \left(1 + \frac{n_s - 1}{2} M^2\right)^{\frac{1}{n_s-1}} \tag{3.28}$$

These equations are similar to their ideal gas counterparts. It is important to note that they involve the compressibility functions β_T and β_p through the isentropic exponents. In addition, the temperature ratio has an exponent, which in the case of

ideal gas reduces to unity. Another useful relation for the compressibility factor Z can be derived by substituting Eq. 3.26 to 3.28 in the real gas EOS

$$\frac{Z_t}{Z} = \frac{p_t v_t}{T_t}\frac{T}{pv} = \left(1 + \frac{n_s - 1}{2}M^2\right)^{1-\frac{m_s n_s}{n_s - 1}} \quad . \tag{3.29}$$

Total quantities are often used when evaluating turbomachinery performance. If the real gas effects are not accounted for, significant discrepancy may arise between the design and the actual operation of a stage.

3.3.2 Corrected Mass Flow per Unit Area

The compressible flow relations can be used to derive the corrected mass flow per unit area equation for real gas. Combining the 1D continuity equation with the real gas EOS and Eq. 3.17 yields

$$\dot{m} = \rho c A = M\frac{Ap\sqrt{n_s}}{\sqrt{ZRT}} \quad . \tag{3.30}$$

Substituting the compressible flow relations and rearranging the terms gives the final form of the equation

$$\frac{\dot{m}\sqrt{Z_t R T_t}}{A p_t \sqrt{n_s}} = M\left(1 + \frac{n_s - 1}{2}M^2\right)^{\frac{-n_s - 1}{2(n_s - 1)}} \quad . \tag{3.31}$$

Similar to ideal gas, Eq. 3.31 has a maximum at $M = 1$. Depending on the particular thermodynamic state however, the isentropic exponent varies and the magnitude of the corrected mass flow per unit area changes. The corrected mass flow function is plotted against Mach number for three different values of n_s in Fig. 3-3. The maximum corrected mass flow per unit area decreases with increasing n_s.

This effect is shown to be more prominent when the isentropic exponent varies between total and static condition in Section 3.7 by examining the behavior of n_s for CO_2. Another useful application of the corrected mass flow per unit area is the assessment of the matching of compressor stages by looking at the excursion from

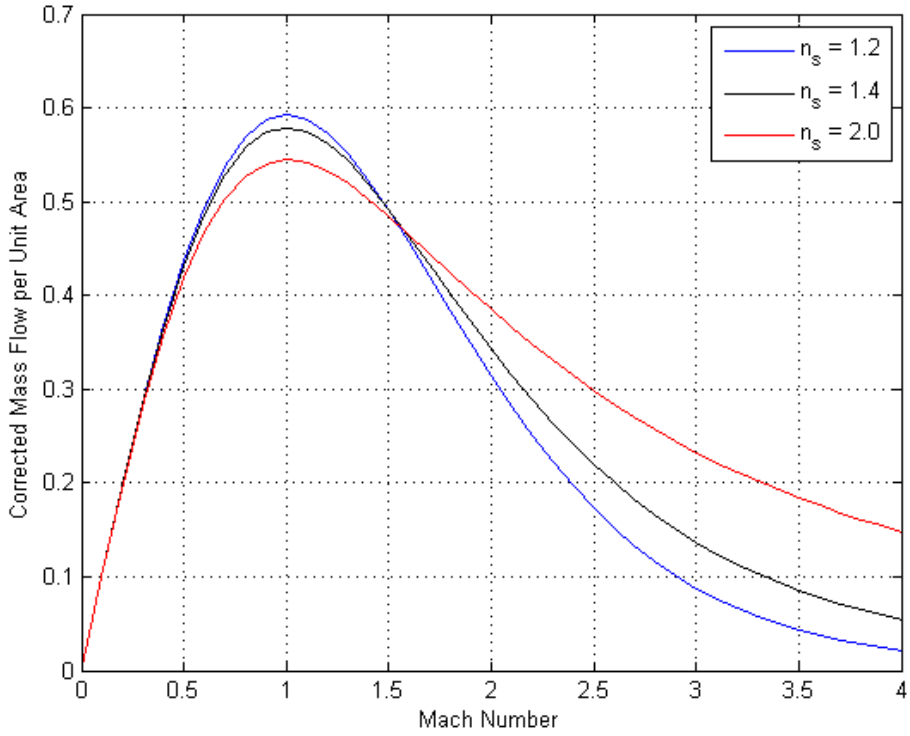

Figure 3-3: Variation in corrected mass flow per unit area with different isentropic exponents

inlet to outlet. This principle is discussed in Chapter 4 for a simplified 2D radial impeller, and in Chapter 6 for the compressor stage under investigation.

3.4 Influence Coefficients for 1-D Compressible Flow

The thermodynamic relations presented so far can be used to examine the effects of area change and shaft work on compressible channel flow without the assumption of an ideal gas. While the quantitative description of the flow field can be obtained with numerical simulations, the differential form of the governing equations gives significant information about the trends in the behavior of the solution. If the area change dA/A and the shaft work $dw_{shaft}/\left(c_pT\right)$ are chosen as independent quantities, the conservation laws and the equation of state yield a system of equations for the flow field variables dc/c, dT/T, dp/p, and $d\rho/\rho$. Other derived quantities such as

da/a and dM/M can be obtained by considering the definitions of speed of sound, Eq. 3.17, and Mach number.

Following the analysis of Greitzer [25] for an ideal gas, the system of equations can be set up as a matrix of influence coefficients, shown in Table 3.3. The detailed derivations of all the real gas expressions are provided in Appendix B and only the final results are presented here. The dependent variables from the first column can be obtained by summing the product of the influence coefficients from the corresponding row with the independent variables at the top of the columns. The change in absolute velocity, for example, is given by

$$\frac{dc}{c} = \left[-\frac{1}{(1-M^2)}\right]\frac{dA}{A} + \left[\frac{1}{(1-M^2)}\frac{(\beta_p T)^2}{(\gamma-1)}\right]\frac{dw_{shaft}}{c_p T} \tag{3.32}$$

where the terms in the square brackets are the influence coefficients. The results presented in [25] can be reproduced by substituting the ideal gas form of the isothermal and isobaric compressibilities from Table 3.1.

	$\frac{dA}{A}$	$\frac{dw_{shaft}}{CpT}$
$\frac{du}{u}$	$-\frac{1}{(1-M^2)}$	$\frac{1}{(1-M^2)}\frac{(\beta_p T)^2}{(\gamma-1)}$
$\frac{dT}{T}$	$\frac{M^2}{(1-M^2)}\frac{(\gamma-1)}{\beta_p T}$	$-\frac{\beta_p T}{(1-M^2)}$
$\frac{dp}{p}$	$\frac{\gamma M^2}{(1-M^2)}\frac{1}{\beta_T p}$	$-\frac{1}{(1-M^2)}\frac{\gamma}{(\gamma-1)}\frac{(\beta_p T)^2}{(\beta_T p)}$
$\frac{d\rho}{\rho}$	$\frac{M^2}{(1-M^2)}$	$-\frac{1}{(1-M^2)}\frac{(\beta_p T)^2}{(\gamma-1)}$
$\frac{dM}{M}$	$-\frac{1+(\Gamma-1)M^2}{(1-M^2)}$	$\frac{\Gamma}{(1-M^2)}\frac{(\beta_p T)^2}{(\gamma-1)}$
$\frac{da}{a}$	$\frac{(\Gamma-1)M^2}{(1-M^2)}$	$\frac{(\Gamma-1)}{(1-M^2)}\frac{(\beta_p T)^2}{(\gamma-1)}$

Table 3.3: Influence coefficients for real gas compressible channel flow.

The term Γ is a thermodynamic property called the fundamental derivative and it relates the relative rate of change of speed of sound with respect to density at constant entropy. The definition and the significance of this property for a real fluid is discussed next.

3.5 The Fundamental derivative

The fundamental derivative Γ is defined as

$$\Gamma = 1 + \frac{\rho}{a}\left(\frac{\partial a}{\partial \rho}\right)_s \quad . \tag{3.33}$$

For an ideal gas, Eq. 3.33 reduces to $\Gamma = \frac{\gamma+1}{2}$ and is always greater than one. However, research in the 60s and 70s has shown that for certain fluids Γ can become negative near the critical point yielding an inverted gas dynamic behavior (Thompson, 1971 [26]). This phenomenon can be illustrated on an isentropic expansion process for example. When $\Gamma > 1$ then $\left(\frac{\partial a}{\partial \rho}\right)_s > 0$, meaning that the speed of sound will decrease as density decreases. As the flow accelerates, density drops and the Mach number increases, as is the case for an ideal gas. When $0 < \Gamma < 1$ then $\left(\frac{\partial a}{\partial \rho}\right)_s < 0$ and the speed of sound will invert its behavior. As the flow accelerates however, the increase in velocity is greater than the increase in speed of sound and the Mach number still increases. In the case when $\Gamma < 0$ there is a complete inversion in the gas dynamic behavior of the fluid. As the flow expands, the speed of sound increases more than the increase in velocity and the Mach number decreases. The reverse process also occurs in an isentropic compression. This effect is reflected by the influence coefficients in the last two rows in Table 3.3.

Alternatively, the fundamental derivative can be related to the curvature of the isentropes in p-v coordinates. Using thermodynamic relations, Eq. 3.33 can be rewritten as

$$\Gamma = \frac{v^3}{2a^2}\left(\frac{\partial^2 p}{\partial v^2}\right)_s \quad . \tag{3.34}$$

In this form, it is more convenient to graphically represent the region where $\Gamma < 0$ on a p-v diagram, as shown in Fig. 3-4.

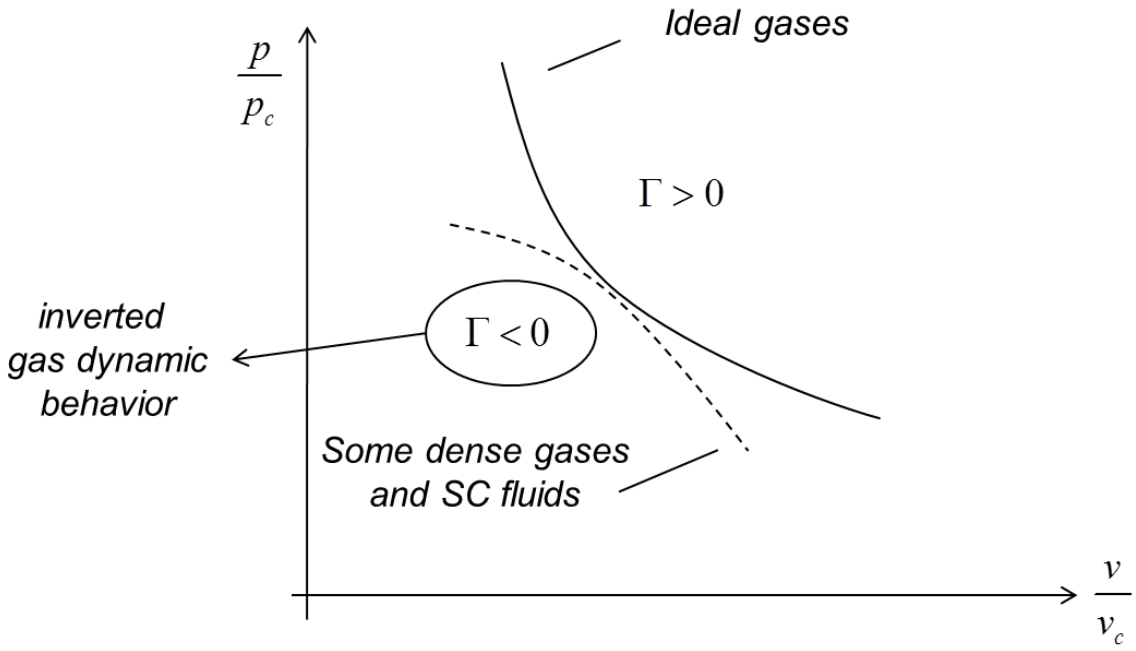

Figure 3-4: Curvature of isentropes.

For example, the inversion of gas dynamic behavior was studied by Colonna et. al. [3] for the expansion of siloxane MDM, a heavy organic fluid, through turbine nozzle guide vanes (NGVs). The behavior was investigated using a two-dimensional Euler solver coupled with a real gas model. This fluid is known to have a region of negative Γ at supercritical states near the critical point. Several cases are analyzed including an expansion starting from subcritical condition corresponding to the actual design point and an expansion starting from a supercritical condition near the critical point.

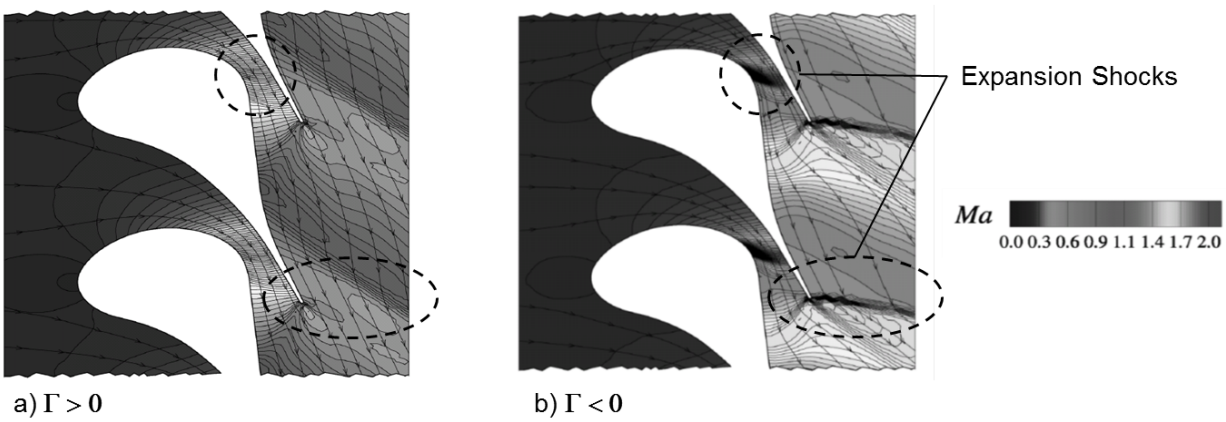

Figure 3-5: a) Design flow conditions with no inversion of gas dynamic effects. b) Inverted gas dynamic behavior at supercritical state. [3]

The results in Fig. 3-5 clearly show the dramatically different flow behavior between the two cases. The inverted color scheme in the Mach contours is indicative of the inverted gas dynamic behavior in the supercritical case. It is particularly visible near the throat, where a rapid expansion occurs, and near the trailing edge where the flow is further expanded through a shock (rarefaction shock). The implications of this study are that non-ideal flow effects can lead to significant deterioration in performance if they are not accounted for in the design. Since CO_2 compressors operate at supercritical conditions, it is important to understand whether the fluid exhibits inverted gas dynamic behavior or not.

To the author's knowledge, no publication has specifically identified the behavior of the fundamental derivative for CO_2. Experimental measurements of this property are unfeasible, while representing the second derivative by means of an EOS model is practically impossible. Using thermodynamic relations however, Γ can be rewritten in terms of first derivatives of the speed of sound with respect to temperature and pressure given by

$$\Gamma = 1 + a\rho \left(\frac{\partial a}{\partial p}\right)_T + \frac{\beta_p a T}{c_p} \left(\frac{\partial a}{\partial T}\right)_p \quad . \tag{3.35}$$

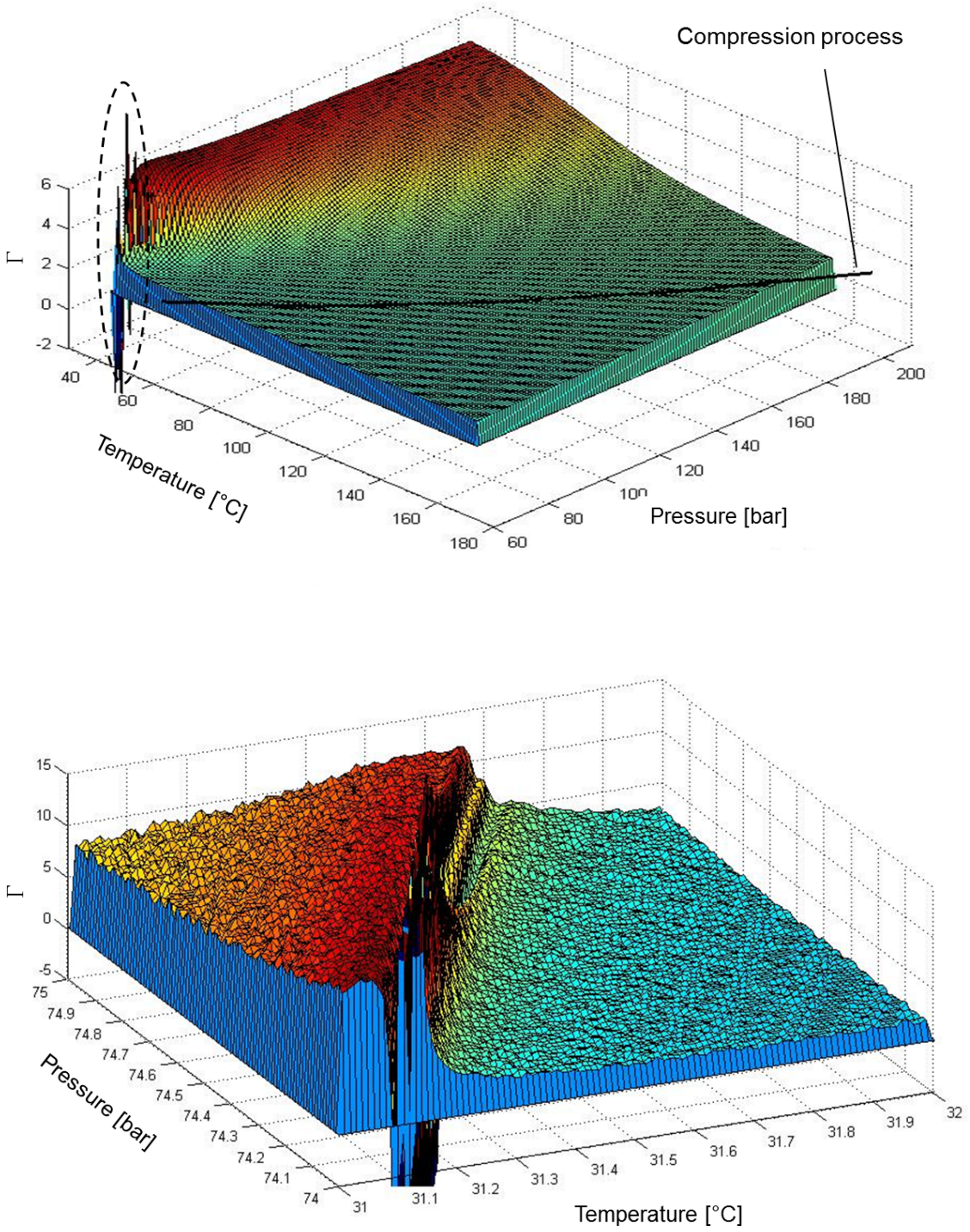

Figure 3-6: Fundamental derivative of CO_2 near the compressor operating range (top) and in the immediate vicinity of the critical point (bottom).

In this form Γ can be evaluated numerically for a specified range of thermodynamic state variables. On a sufficiently fine grid the derivatives of the speed of sound can be represented using a central difference scheme. The range of thermodynamic states is selected near the operating range of the CO_2 compressor and data is obtained from NIST's Chemistry WebBook [24]. Smooth representation of Γ is achieved with $\Delta p = 1$ bar and $\Delta T = 1°C$.

Even with the most advanced EOS model, it is difficult to accurately estimate Γ at the critical point due to the uncertainty in speed of sound. However in the region of interest where the machine operates, Γ remains positive which suggests that inverted gas dynamic behavior is not a concern for the CO_2 compressor under investigation.

3.6 Variation of Real Gas Properties for CO_2

Even though CO_2 does not exhibit inverted gas dynamic behavior, there are other important differences between ideal and real gas, as previously discussed. It is important to assess how much they matter for CO_2 and what the impact on the supercritical CO_2 compressor performance is. A comprehensive answer to these questions requires the use of high fidelity numerical simulations, presented in the following chapters. However, an initial assessment can be obtained by interrogating the behavior of real gas properties of CO_2. It is convenient to represent these properties in a T-s diagram to better understand their variation with respect to the critical point and the operating range of the compressor.

Each segment of the black line in Fig. 3-7 represents an individual stage of the high-pressure block of the CO_2 compressor. It is important to note that the iso-Z lines (in green) are nearly orthogonal to the compression process in the vicinity of the machine's operating range, implying that Z remains almost constant through each stage. In this case, real gas effects are expected to have no significant impact on the flow behavior. This hypothesis is examined using CFD simulations in Chapter 4.

Fig. 3-8 shows the variation of the isentropic exponent n_s for CO_2. Even though the isentropic exponent behaves quite differently from the compressibility factor, the

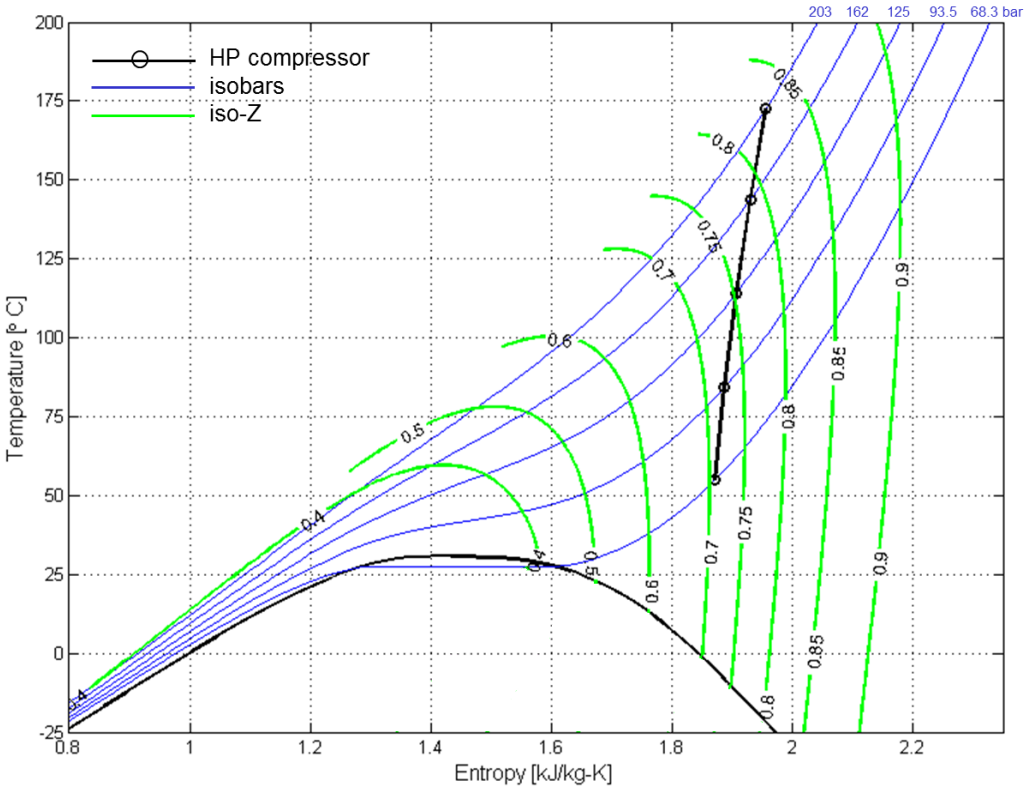

Figure 3-7: Variation in compressibility factor Z for CO_2.

gradients near the compressor operating range are much smaller compared to those in the vicinity of the critical point. The individual stages of the CO_2 compressor are experiencing a 3% change in n_s. Using an average value for n_s in the compressible flow equations is expected to give fairly accurate results, even though there is small deviation from the assumption made in Section 3.2 that the isentropic exponent remains constant. The error associated with this deviation can be quantified numerically using a canonical test case. The isentropic expansion of CO_2 through a converging nozzle is investigated at two different stagnation states. In the first case, total pressure and total temperature at the inlet are set to 93.5 bar and 357 K, corresponding to the outlet condition of the candidate compressor stage. In the second case, the inlet condition is moved closer to the empirical safety margin along a constant temperature line, by increasing the pressure to 140 bar, as shown in Fig. 3-8. The comparison of the corrected mass flow per unit area obtained from the CFD simulations with the value given by Eq. 3.31 is discussed next. Additional diagrams

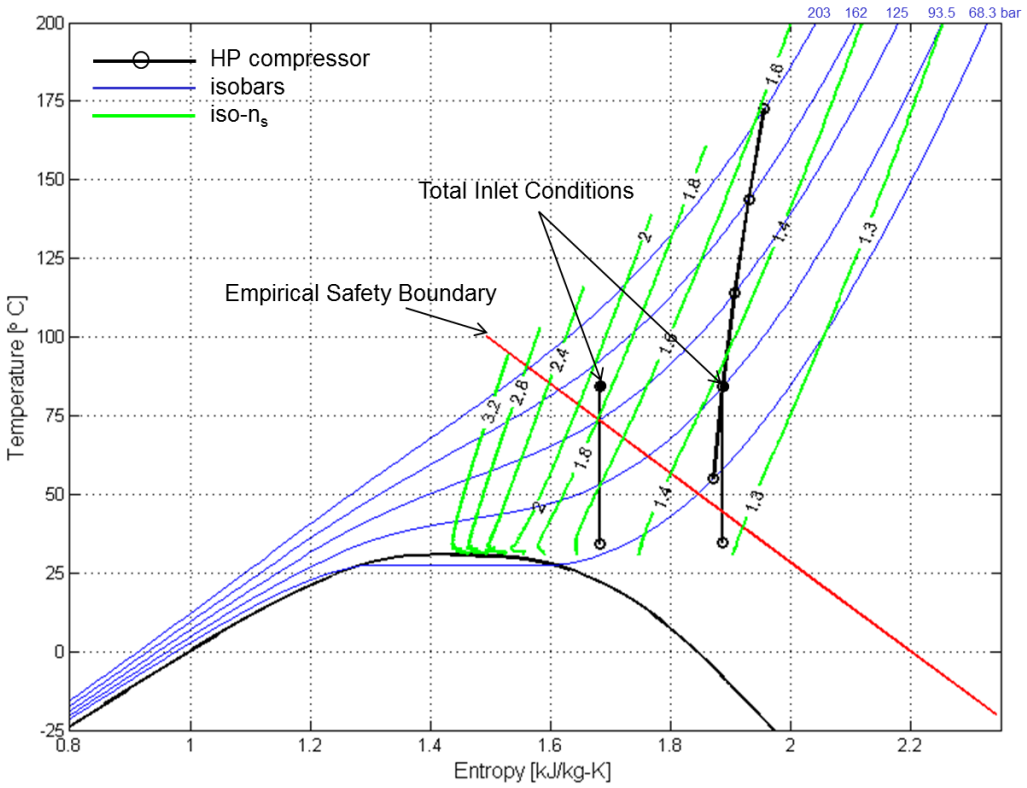

Figure 3-8: Variation in isentropic exponent n_s for CO_2.

with other real gas properties of CO_2 can be found in Appendix C.

3.7 Canonical Test Case: Converging Nozzle

3.7.1 Computational Domain

The calculations are conducted with ANSYS CFX using a steady-state RANS solver with the k-Ω SST turbulence model. The real gas properties of the fluid are provided by the Lee-Kesler model. The nozzle profile and grid are shown in Fig. 3-9. The profile of the nozzle wall is chosen to be circular with a diameter that is about 10 times larger than the throat length to minimize flow non-uniformity. The short, straight section of the wall starting from the inlet is blended with the circular profile using a spline curve. A free-slip, adiabatic boundary condition is applied to the wall to achieve isentropic flow. To assess the deviation from 1D compressible flow theory, CFD simulations are performed with air at ideal gas conditions for several

different pressure ratios. The deviation in Mach number at the throat due to flow non-uniformity is found to be less than 0.2% in all cases. The boundary conditions at the inlet are set per the discussion in Section 3.6. The static pressure at the outlet is varied to achieve Mach numbers at the throat from 0.5 to 1.

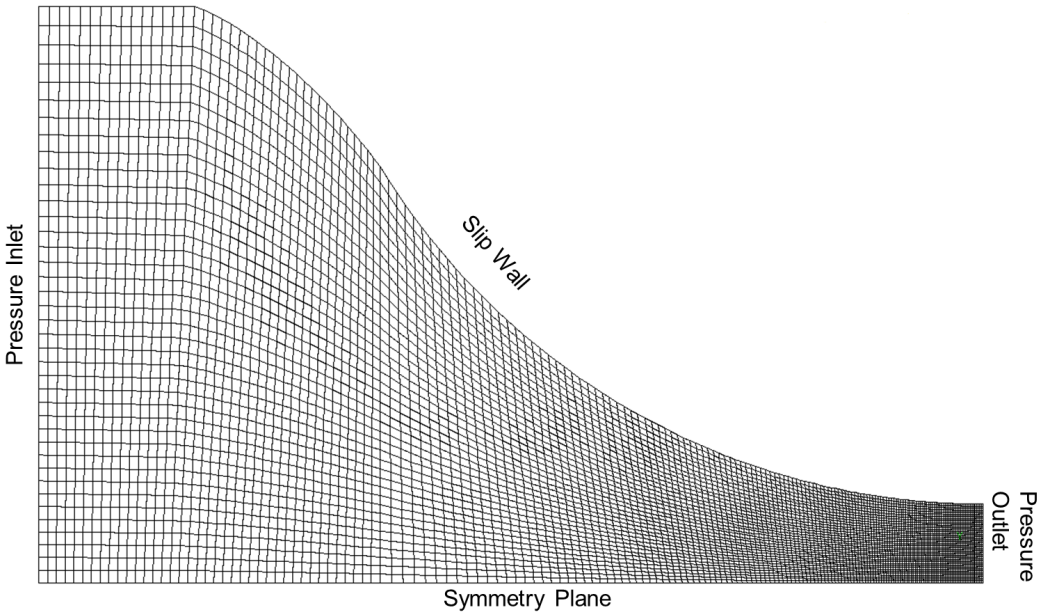

Figure 3-9: 2D Nozzle geometry and mesh setup

3.7.2 Effects of n_s on Corrected Mass Flow

Figures 3-10 and 3-11 show the Mach number distribution and the corresponding variation of the isentropic exponent through the nozzle at the different stagnation states.

For the case where the total inlet conditions are along the compressor operating line, the isentropic exponent varies from 1.39 to 1.32, or only by 6%. Closer to the empirical safety line the variation increases up to 20%. The results can be used to calculate the exact value of the corrected mass flow per unit area, the left hand side of Eq. 3.31, and to plot it against throat Mach number for a range of pressure ratios. Figure 3-12 compares the numerical results to the corrected mass flow per unit area obtained with Eq. 3.31. The corrected mass flow for air at ideal gas conditions is also

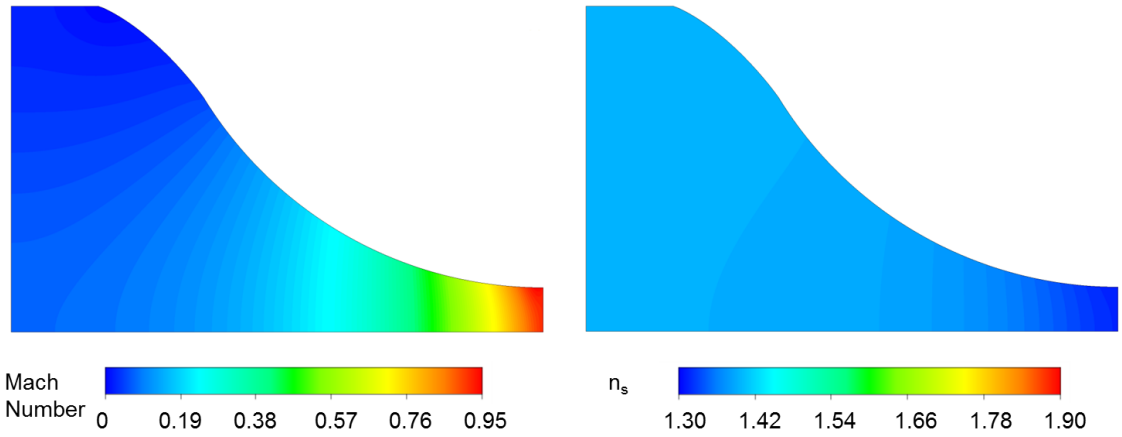

Figure 3-10: Nozzle flow field at $p_t = 93.5$ bar

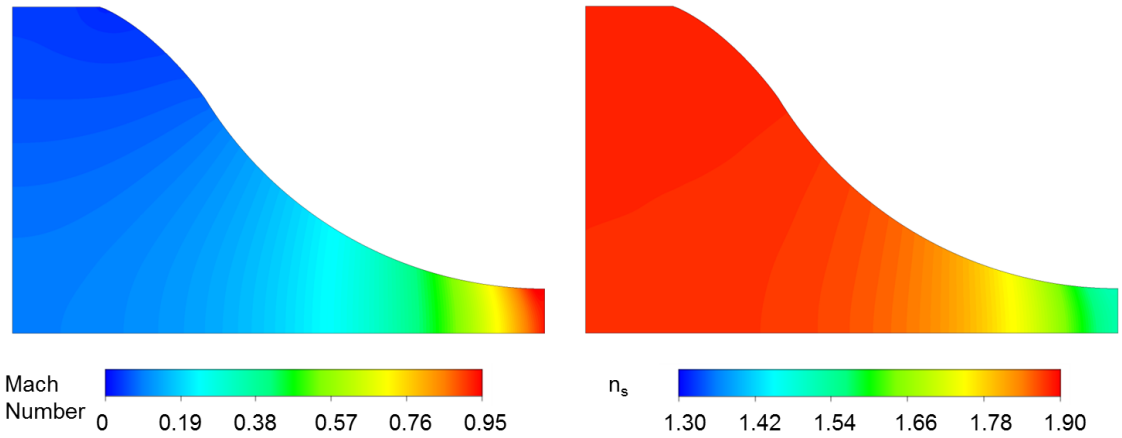

Figure 3-11: Nozzle flow field at $p_t = 140$ bar

shown as a reference.

Away from the critical point, the error in Eq. 3.31 is about 1% for a maximum variation in isentropic exponent of 6%. Furthermore, the average value of n_s is close to that for air at ideal gas conditions. Consequently, the corrected mass flow per unit area for the two fluids is shown to be similar in this region. Approaching the empirical safety line where the variations in n_s increase up to 20%, the error rises to more than 7%. The implication is that in the vicinity of the compressor operating range, the relations derived in Section 3.3 give fairly accurate results despite the small variation in isentropic exponent. The accuracy gradually diminishes approaching the critical point due to the steep gradients in n_s.

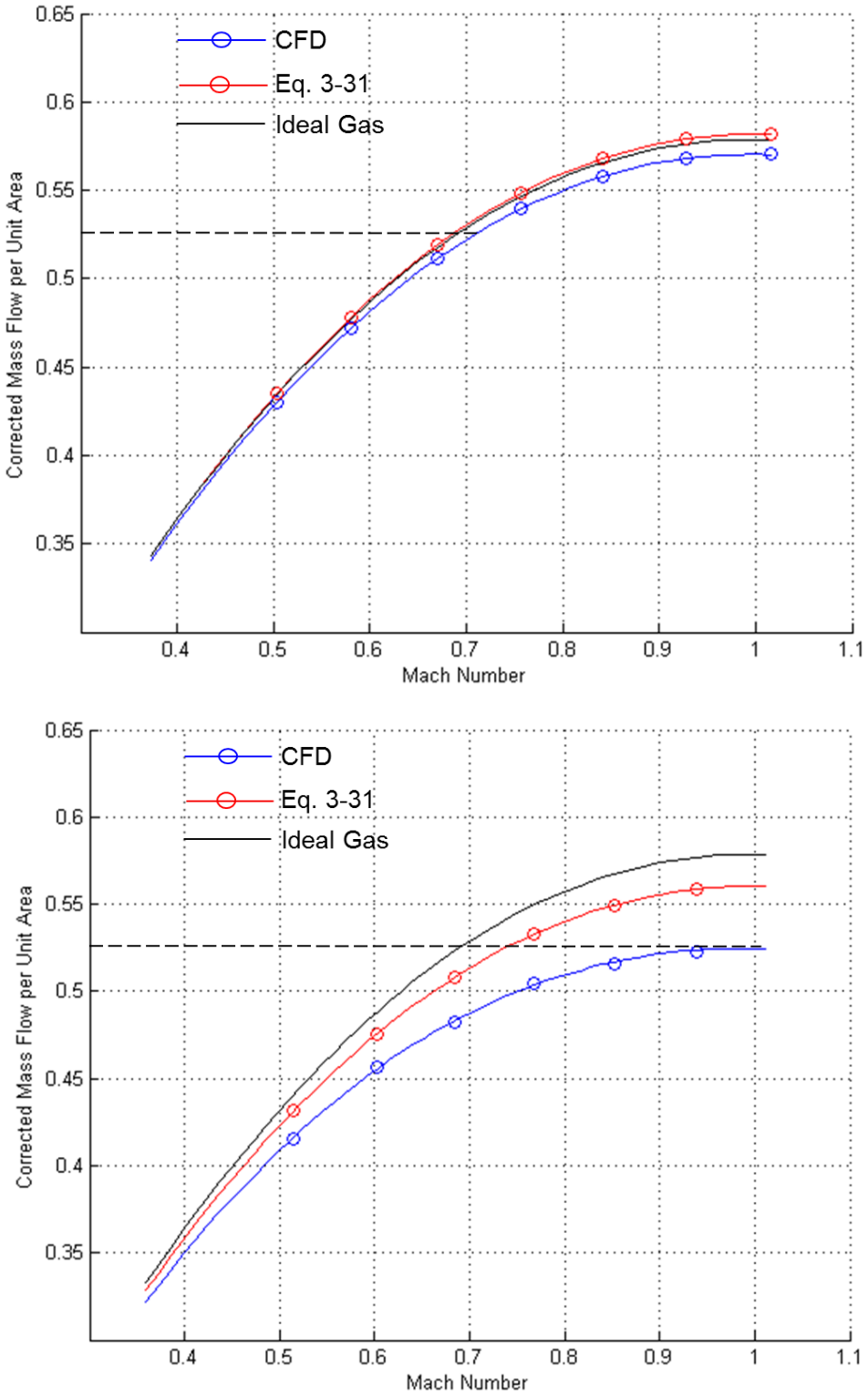

Figure 3-12: Corrected mass flow comparison for inlet total pressure of 93.5 bar (top) and 140 bar (bottom).

It is important to note that the value of the corrected mass flow function decreases as the isentropic exponent increases. A device designed to operate with corrected mass flow per unit area of 0.52 would have a Mach number of about 0.7 for $n_s = 1.4$. If that device operates in the vicinity of the empirical safety margin, for the same corrected mass flow per unit area the corresponding Mach number will be closer to sonic condition. The implication for a compressor stage is that it may choke sooner than expected at these off-design conditions. This effect is demonstrated on the actual compressor stage in Chapter 6.

3.8 Chapter Summary

Several fundamental thermodynamic relations for real gas are presented in this chapter, emphasizing the importance of real gas properties such as the compressibility factor, and the isothermal and isobaric compressibilities. These properties are shown to have impact on the isentropic relations, definition of speed of sound, compressible flow equations, and corrected mass flow per unit area. These tools provide a foundation for an initial assessment of the compressor stage. The variations of real gas properties for CO_2 are examined over a wide range of thermodynamic states and several hypothesis and insights are drawn regarding the operation of the stage:

- Inverted gas dynamic behavior is not a concern because the fundamental derivative remains positive in the region of interest.

- Near the current operating conditions of the compressor, the gradients of Z are orthogonal to the compression process. Furthermore, the isentropic exponent varies by less than 3% and is similar to that of air at ideal gas conditions. At these conditions real gas effects are expected to have no significant impact on compressor performance and stage matching.

- The compressor may choke sooner than expected when approaching the critical point due to the significant increase in the isentropic exponent.

These hypotheses are investigated further in the following chapters and the impact of real gas effects on the compressor stage is quantified through CFD simulations.

Chapter 4

Compressor Performance Away From the Critical Point

The deviation of CO_2 from ideal gas behavior at supercritical conditions was shown in the previous chapter by studying the variation in real gas properties. A qualitative analysis of real gas effects in internal flow situations was obtained through the principle of corrected mass flow per unit area and several hypotheses regarding their impact on the candidate compressor stage were established. A brief discussion of the design features of a centrifugal compressor is presented in this chapter along with the performance metrics that are used to characterize the stage. A simplified 2D radial blade row is used to demonstrate the analysis methods and to provide an initial assessment of real gas effects, before extending the CFD calculations to the candidate compressor stage at its current operating conditions.

4.1 Compressor Performance Metrics

The notation for labeling individual stage components and the definitions of the compressor performance metrics are briefly introduced here. Figure 4-1, adapted from Casey et al [4], shows a schematic representation of a centrifugal compressor stage, indicating the different components and corresponding station numbers. The diffuser section can be vaned or vaneless depending on the particular design. The last

stage in a compressor block typically discharges into a plenum, represented by the dashed lines.

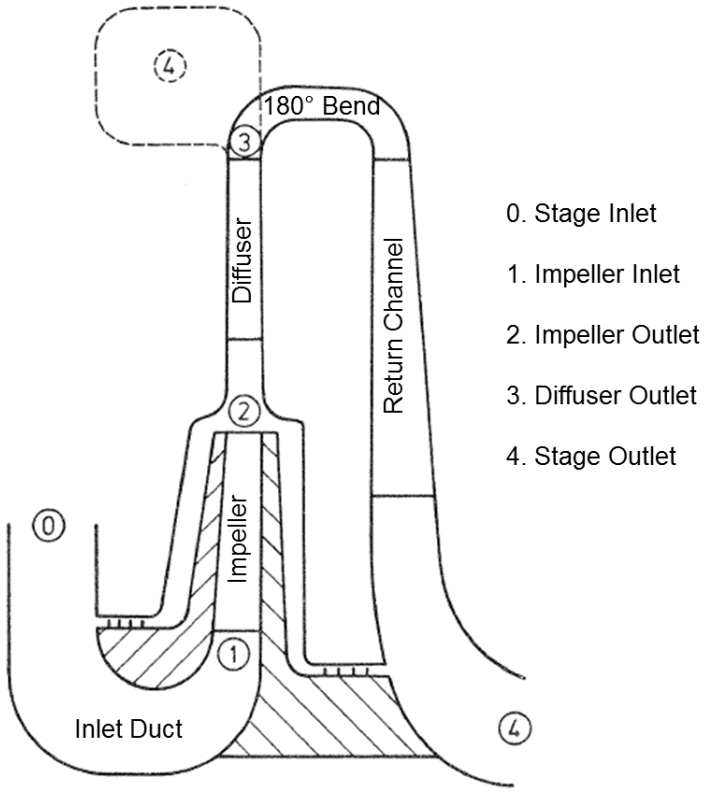

Figure 4-1: Centrifugal compressor stage adapted from [4].

As in many fluid mechanics problems, the most convenient way to characterize turbomachinery devices is by means of non-dimensional parameters. The performance of a compressor stage is determined by its geometry, the flow rate $\dot{m}$, pressure and temperature at the inlet, the gas properties, and the rotational speed Ω. Using dimensional analysis, several parameters can be identified which describe the operation of the stage.

The flow coefficient ϕ is defined as the mass flow rate non-dimensionalized by a characteristic density, the stagnation density at inlet $\rho_{t,0}$, a characteristic velocity, the impeller tip speed U_2, and a characteristic area based on the impeller diameter

$$\phi = \frac{\dot{m}}{\frac{\pi}{4}\rho_{t,0}U_2 d_2^2} \quad . \tag{4.1}$$

The mass flow at inlet can be expressed as the product of the inlet density, the meridional velocity, and the inlet area, and Eq. 4.1 can be rewritten as

$$\phi = \frac{\rho_1}{\rho_{t,0}} \frac{c_{m1}}{U_2} \frac{A_1}{\frac{\pi}{4} d_2^2} \quad . \tag{4.2}$$

If for a given stage the area ratio is constant, ϕ can be interpreted as non-dimensional velocity coefficient, which relates to the flow angle, and hence incidence angle, through the velocity triangles as shown in Fig. 4-2.

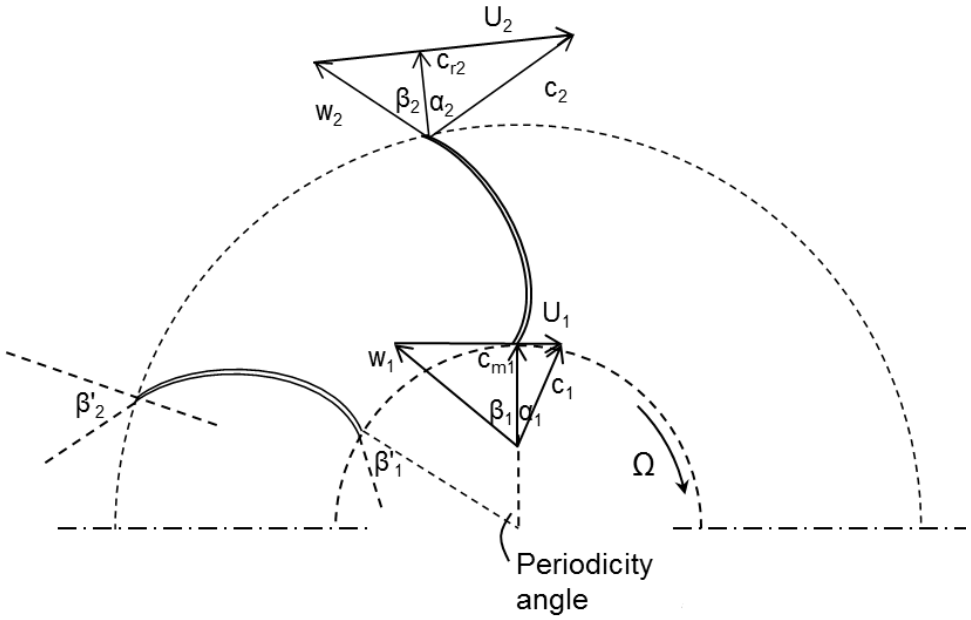

Figure 4-2: Velocity triangles at inlet and outlet of a centrifugal impeller.

The pressure coefficient μ_p is a measurement of the useful specific work of the compressor w_p, non-dimensionalized by the impeller specific kinetic energy. Since both of these are proportional to the square of the impeller tip speed, the expression for μ_p can be written as

$$\mu_p = \frac{w_p}{U_2^2} \quad . \tag{4.3}$$

The useful work is the energy input that goes into raising the pressure of the fluid and is not wasted into overcoming internal losses. It is defined as

$$w_p = \int_0^4 v dp \quad . \tag{4.4}$$

A relationship between w_p and the pressure ratio of the stage can be obtained under the assumption that the compression follows a polytropic process of the form $pv^n = const.$ The path-dependent process is governed by the entropy generation through various loss mechanisms. The special case of an isentropic process was discussed in Section 3.2. Since the mathematical formulation is identical, the same procedure can be used here to perform the integration in Eq. 4.4 yielding

$$w_p = \frac{n}{n-1}\left(p_{t,4}v_{t,4} - p_{t,0}v_{t,0}\right) = \frac{n}{n-1} Z_{t,0} R T_{t,0} \left[\left(\frac{p_{t,4}}{p_{t,0}}\right)^{\frac{n-1}{n}} - 1\right] \quad . \tag{4.5}$$

Unlike the isentropic exponent n_s which is a state variable, the polytropic exponent n is a process-dependent variable and can be calculated using the initial and final states

$$n = \frac{\log\left(p_{t,4}/p_{t,0}\right)}{\log\left(v_{t,0}/v_{t,4}\right)} \quad . \tag{4.6}$$

Substituting Eq. 4.5 into 4.3 yields the final form of the pressure coefficient

$$\mu_p = \frac{n}{n-1}\frac{Z_{t,0} R T_{t,0}}{U_2^2}\left[\left(\frac{p_{t,4}}{p_{t,0}}\right)^{\frac{n-1}{n}} - 1\right] \quad . \tag{4.7}$$

In many publications μ_p is also referred to as the polytropic head coefficient. Similarly, the polytropic efficiency η_p of the stage is defined as

$$\eta_p = \frac{w_p}{h_{t,4} - h_{t,0}} \quad . \tag{4.8}$$

It is related to the pressure coefficient through the work input coefficient μ_0 via the expression $\mu_p = \eta_p \mu_0$. The definitions presented so far follow the ones used by Schultz in [6], where additional discussions on the polytropic compression for real gas can be found. The inlet and outlet conditions of a radial machine are related by the

specific speed

$$N_s = \frac{\phi^{1/2}}{\psi^{3/4}} \tag{4.9}$$

where ψ is the loading coefficient given by $\Delta p / (\rho_t \Omega^2 d_2^2)$. For a given family of designs, the specific speed is governed primarily by the ratio of the inlet to outlet diameter, as discussed by Cumpsty in [27].

Another important parameter, the machine Mach number M_{U_2}, is the impeller tip speed normalized by the stagnation speed of sound at inlet

$$M_{U_2} = \frac{U_2}{a_{t,0}} = \frac{\Omega r_2}{a_{t,0}} \quad . \tag{4.10}$$

This is not a real Mach number in a fluid dynamic sense, but it provides a useful relation between the pressure and temperature rise in a stage as discussed in [4]. For an ideal gas, it reduces to the more commonly used corrected speed $\Omega_{cor} = \Omega / \sqrt{T/T_{ref}}$, but it should not be employed for a real gas because of the pressure dependence of the speed of sound.

4.2 Design Considerations

The design flow coefficients of centrifugal compressors usually span from 0.01 to 0.12. Figure 4-3, adopted from Casey et al [4], shows the variation in design point efficiency with flow coefficient for a range of specific speeds, as well as the relative magnitude of the three main types of loss mechanisms. Also included in the figure are sketches of meridional sections through the impellers which provide a physical perception of the design based on specific speed.

At high flow coefficients of $\phi > 0.1$, performance begins to deteriorate due to high fluid velocities. The decrease in efficiency is more dramatic for $\phi < 0.05$ where all three types of losses increase significantly. Low flow coefficient stages are characterized by narrow gas paths yielding increased aerodynamic losses due to friction. The leakage flows over the hub and shroud for a given family of stages remains relatively constant

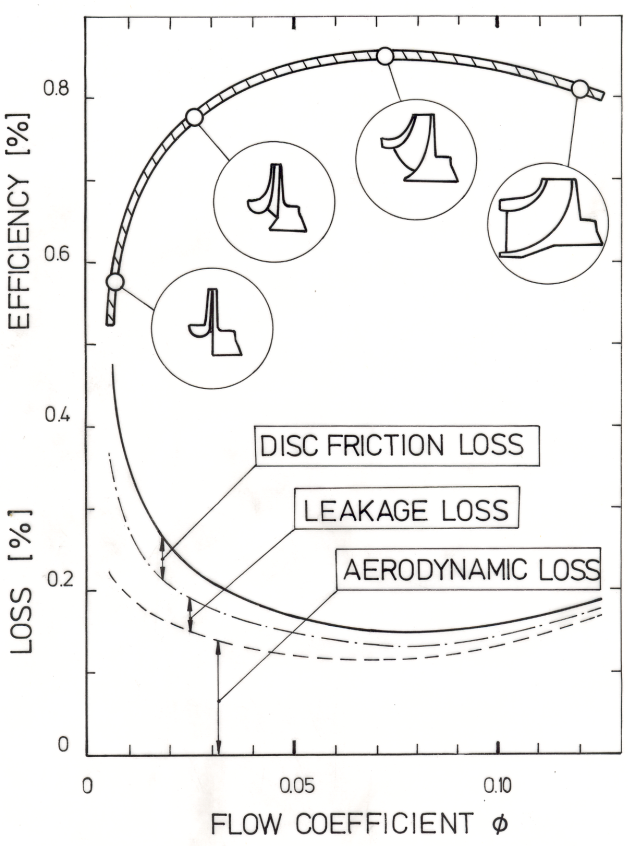

Figure 4-3: Typical design point performance of centrifugal stages from [4].

as it depends mostly on the seal design and the pressure ratio across it. At low flow coefficients, the leakage flows represent a larger portion of the total flow through the stage yielding an increased loss in efficiency. Similarly, the power required to overcome disc friction losses is shown to be relatively independent from the flow rate [28], but the proportion to the total shaft power increases at low flow coefficients.

Because of the liquid-like density of supercritical CO_2 and the relatively low mass flow rates associated with these applications, the required compressor stages are pushing the lower limits of the design spectrum. For instance, the candidate compressor stage is designed for $\phi = 0.009$, while the last stage of the same block must operate at $\phi = 0.006$ due to the increase in density. These stages however would yield better efficiencies than the ones predicted by Fig. 4-3 due to the Reynolds number effect. The Reynolds number of a centrifugal compressor stage is defined as

$$Re = \frac{U_2 b_2}{\nu_{t,0}} \tag{4.11}$$

where b_2 is the impeller width at outlet and $\nu_{t,0}$ is the kinematic viscosity at total inlet conditions. An empirical correlation is proposed by Casey that relates the Reynolds number to a change in efficiency over a reference state [5].

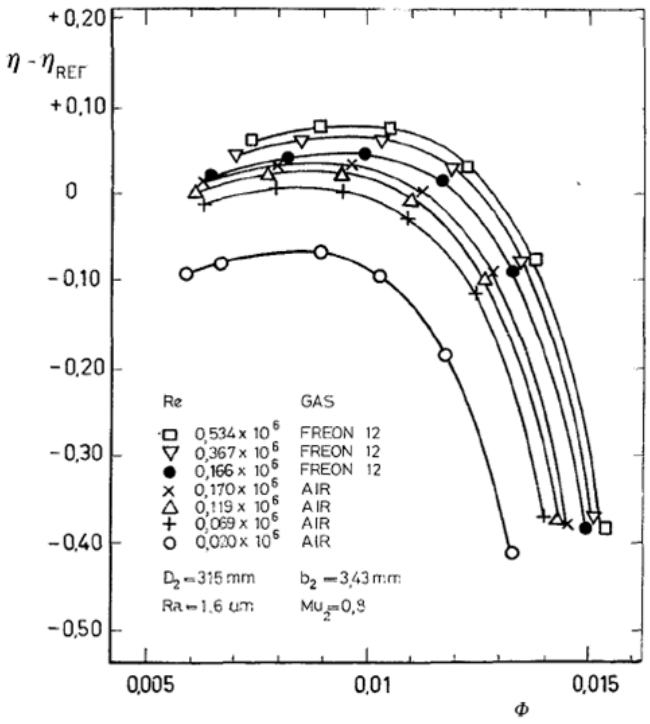

Figure 4-4: Reynolds number effect on low flow coefficient stages from. [5]

The correlation is obtained through the analysis of friction losses from tests of a wide range of centrifugal compressors. The results are summarized in a plot of $\Delta\eta_p$ against flow coefficient at different Reynolds numbers, presented in Fig. 4-4. The kinematic viscosity of supercritical CO_2 is about two orders of magnitude lower than that of air yielding Re on the order of 10^7, much larger than that of conventional compressors. Due to the logarithmic nature of the correlation, the expected efficiency gain for the candidate compressor stage with CO_2 is predicted to be around 5% compared to atmospheric air with Re of 10^5.

4.3 Canonical Test Case: 2D Radial Impeller

The main purpose of this test case is to assess the following hypothesis. Near the current operating conditions of the candidate compressor stage the gradients in the compressibility factor are almost orthogonal to the compression process. This suggests that real gas effects have little impact on the machine's performance and stage matching. The actual compressor stage however, involves many intricate features, so it is useful to first examine a simplified turbomachinery test case.

4.3.1 2D Impeller Definition

The 2D radial impeller and vaneless diffuser setup, shown in Fig. 4-5, incorporates much of the real compressor elements, such as rotating frame and blade cascade aerodynamics, but without the complexity of 3D flow features and endwall effects.

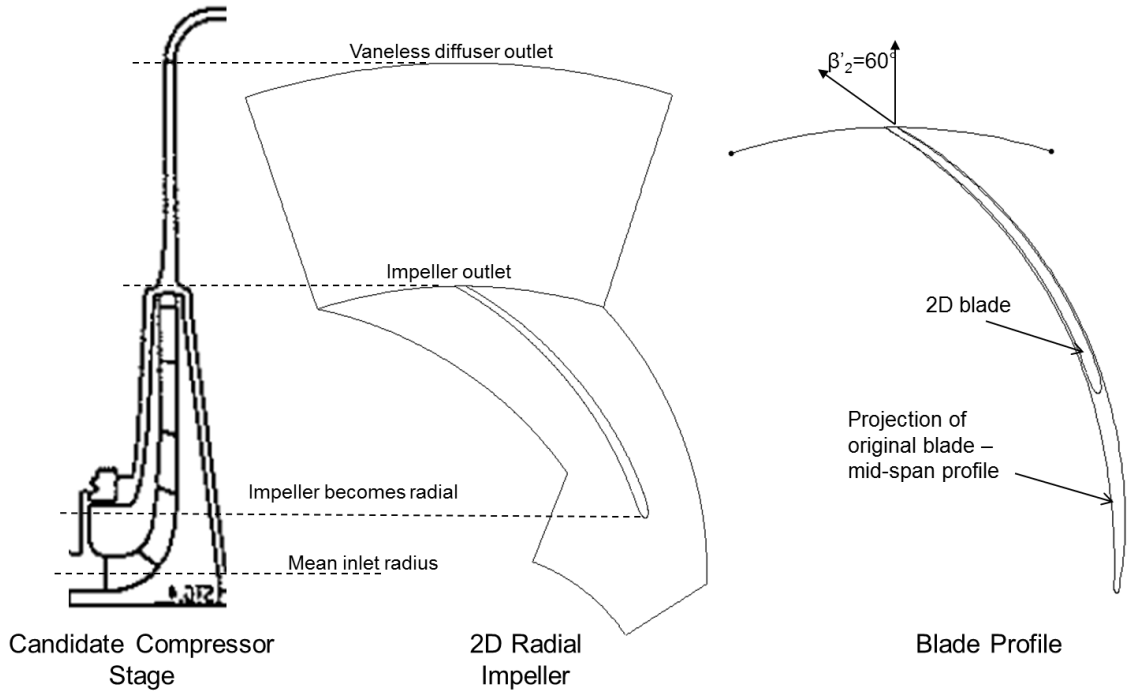

Figure 4-5: 2D radial impeller and vaneless diffuser setup.

The geometrical definitions of the 2D radial impeller and vaneless diffuser are derived from the candidate compressor stage introduced in Chapter 1. The blade

profile is modeled after the radial part of the original 3D blade, as shown in Fig. 4-5. As a result, the leading edge (LE) of the 2D blade is moved to a slightly higher inlet radius as compared to the actual stage, while the blunt trailing edge (TE) is kept at the same radial location and with the same blade metal angle β_2'. The vaneless diffuser extends up to the start of the 180° bend of the actual stage. The original impeller contains 10 blades, resulting in a blade passage periodicity of 36°. The same blade count is used for the 2D model. More detailed description of the candidate compressor stage is provided in Section 4.4.

4.3.2 Scope of Investigation

Four sets of numerical simulations are performed with the 2D radial impeller. They are grouped into categories based on different fluid conditions, which are summarized in Table 4.1. Each set represents a characteristic speed line for the compressor, that is a sweep of flow coefficients between the stall and choke points of the stage at the same machine Mach number of $M_{U_2} = 0.75$.

	Fluid	Inlet Conditions	Re number
1	Ideal Gas Air	Atmospheric	10^5
2	Ideal Gas Air	High Pressure	5×10^6
3	Ideal Gas CO_2	High Pressure	5×10^6
4	Real Gas CO_2	High Pressure	10^7

Table 4.1: 2D radial impeller simulation matrix.

The CFD calculations are conducted in ANSYS Fluent using steady state, density-based RANS solver in a rotating frame of reference with the k-Ω SST turbulence model. All simulations are performed for a single passage with periodic boundary conditions. The mesh for the 2D radial impeller and diffuser was created in Pointwise. The turbulence model requires a y^+ value of 1 for an accurate representation of the boundary layers. To control the size of the cells within the boundary layers, a blocking structure is wrapped around the blade. Because of the lower Reynolds number, the mesh for the atmospheric air simulation requires fewer cells compared to the other cases.

For the first speed line the working fluid is set to air at ideal gas conditions with stagnation properties at the inlet corresponding to the standard atmosphere ($T_{t,0} = 288\,\mathrm{K}$, $p_{t,0} = 1.01325\,\mathrm{bar}$). The working fluid in the second case is kept the same but the stagnation properties at inlet are raised to the conditions corresponding to the candidate compressor stage ($T_{t,0} = 328\,\mathrm{K}$, $p_{t,0} = 68.27\,\mathrm{bar}$). The same inlet conditions are used for the last two speed lines, but the working fluid is changed to CO_2 at ideal gas conditions with constant c_p, viscosity, and thermal conductivity, and real gas CO_2 using the LK EOS model. A pressure outlet boundary condition is applied at the outlet of the vaneless diffuser. The value of the static pressure is varied accordingly for each case to yield the same range of flow coefficients along the speed line.

4.3.3 Performance Analysis

The results from the numerical calculations are summarized in the form of compressor characteristics in Fig. 4-6. The flow coefficient, polytropic efficiency, and pressure coefficient are calculated via Eq. 4.1, 4.7, and 4.8 using mass-weighted average quantities obtained from the CFD results.

The design point of the compressor is identical in all four cases at $\phi = 0.019$. A weak Reynolds number effect can be observed from the efficiency plots in Fig. 4-6. The trends between the cases are consistent with the Reynolds numbers, but the magnitudes are much smaller than the ones expected for a real compressor stage, as described in Section 4.2. In this simplified test case most of the loss mechanisms, such as endwall effects, leakage flows, and disk friction are absent. The only loss source is the profile drag yielding relatively high efficiency levels. The pressure coefficient plots also show small difference of less than 1% near the design point between the four cases. The similarity in the operation of the 2D radial impeller for the different fluid conditions can be demonstrated qualitatively by comparing the flow fields. Figure 4-7 shows the contours of relative Mach number at the peak efficiency point of each performance characteristic.

The results of this study support the claim that real gas effects have little impact

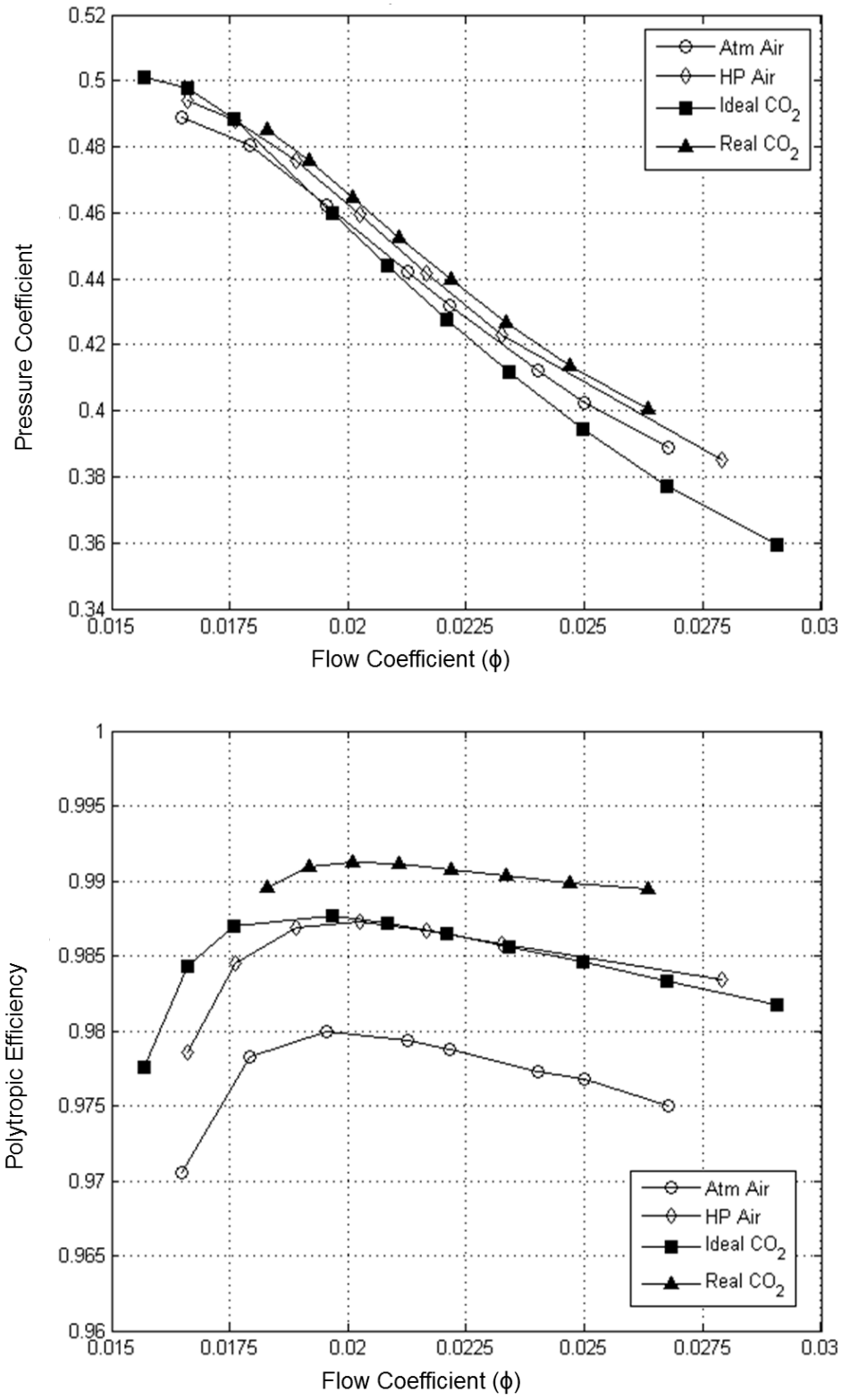

Figure 4-6: 2D radial impeller performance characteristics at $M_{U_2} = 0.75$: pressure coefficient (top), polytropic efficiency (bottom).

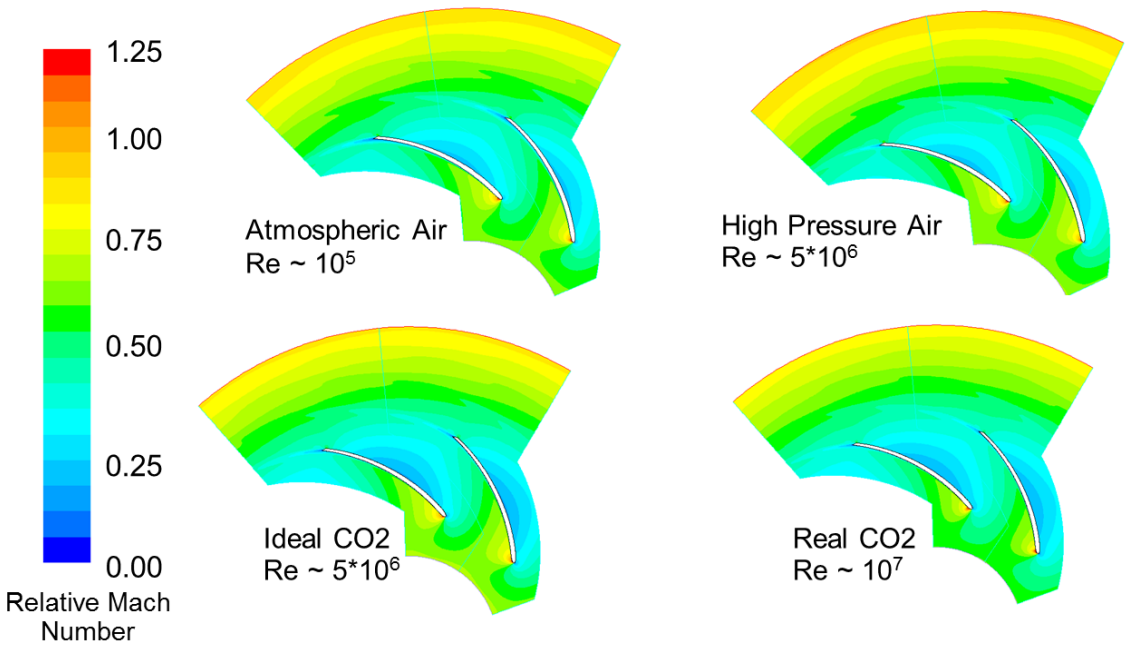

Figure 4-7: Weak Reynolds number effect in the 2D radial impeller.

on the compressor stage performance near its current operating conditions. Its operation can be accurately modeled using an ideal gas provided that dynamic similarity with the real fluid conditions is preserved.

4.3.4 Stage Matching Analysis

Next, the matching of compressor stages in multistage configuration is assessed. The performance of the first stage determines the stagnation properties at the inlet of the following stage, affecting both the flow coefficient and machine Mach number of the latter. These two parameters however, can be related by taking the product of Equations 4.1 and 4.10

$$\phi M_{U_2} = \frac{\dot{m}}{\frac{\pi}{4}\rho_{t,0} a_{t,0} d_2^2} \quad . \tag{4.12}$$

Using the real gas EOS and Eq. 3.17 to express the density and the speed of sound in terms of temperature and pressure and dividing both sides of Eq. 4.12 by the inlet area gives

$$\phi M_{U_2} \left(\frac{\pi d_2^2}{4 A_0} \right) = \frac{\dot{m} \sqrt{Z_{t,0} R T_{t,0}}}{A_0 p_{t,0} \sqrt{n_s}} \quad . \tag{4.13}$$

The right hand side of Eq. 4.13 is the corrected mass flow per unit area, and the excursion in corrected flow from inlet to outlet of a stage determines the swing in incidence into the next stage. At high pressure, where compressibility is important, small swings in inlet corrected mass flow can lead to larger swings in exit corrected mass flow. This concept is presented in more detail by Cumpsty [27]. The emphasis in this section is on assessing the impact of real gas effects on the stage matching process using the 2D radial impeller calculations. The pressure coefficient is plotted against the normalized corrected mass flow per unit area at inlet and outlet for the four cases, as shown in Fig. 4-8. The identical swing in corrected mass flow between the real and ideal gas cases indicates that real gas effects have little impact on matching at the current operating conditions of the stage.

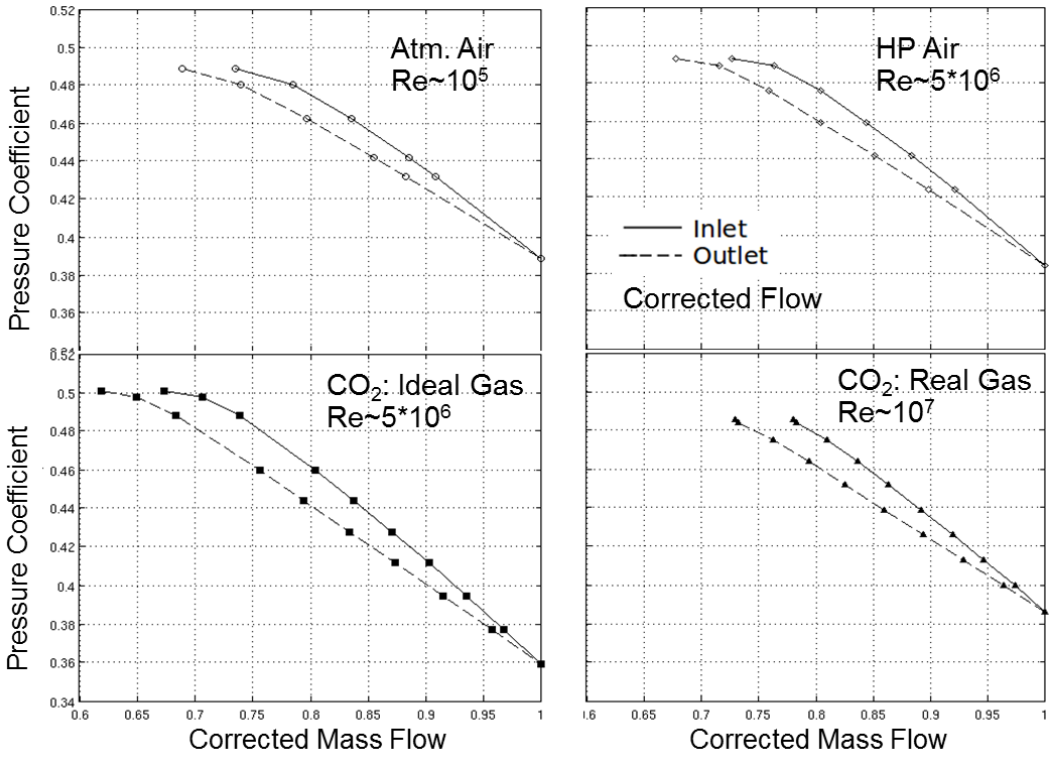

Figure 4-8: Excursions in corrected mass flow from inlet to outlet.

As discussed in Chapter 3, approaching the critical point the corrected mass flow

per unit area becomes more sensitive to fluctuations in Mach number due to the increase in the isentropic exponent. As a result, the swing in corrected flow through the stage is expected to increase as well at these conditions. This effect is investigated on the candidate compressor stage in Chapter 6. A detailed investigation of the compressor performance a the current operating conditions is presented in the following section.

4.4 Candidate Compressor Stage

4.4.1 Stage Geometry

The candidate compressor stage is the first stage in the high-pressure block of the CO_2 compressor, the one that operates closest to the critical point and two-phase region. Figure 4-9 shows a 3D sectional view along with a meridional view of the compressor indicating the narrow passages associated with low flow coefficient stages. A set of inlet guide vanes (not shown in the figure) de-swirl the incoming flow such that the velocity field at the inlet is in the meridional direction. The stage also features a shrouded impeller, which eliminates tip leakage flows.

The vaneless diffuser is pinched to avoid flow instability due to the highly swirling flow coming out of the impeller. Similar to the 2D radial blade row, this study is focused only on the impeller and vaneless diffuser of the stage. At the exit of the diffuser the flow is decelerated below Mach 0.3 so that in the downstream static passages it is essentially incompressible.

4.4.2 Performance Analysis

The computational setup for the compressor stage is similar to that previously discussed for the 2D radial impeller. The stagnation temperature ($T_{t,0} = 328\,\mathrm{K}$) and pressure ($p_{t,0} = 68.27\,\mathrm{bar}$) are specified at the inlet and the static pressure at outlet is varied to achieve a full performance characteristic. The machine Mach number is again set to 0.75. Two investigations are performed: with CO_2 at ideal gas conditions,

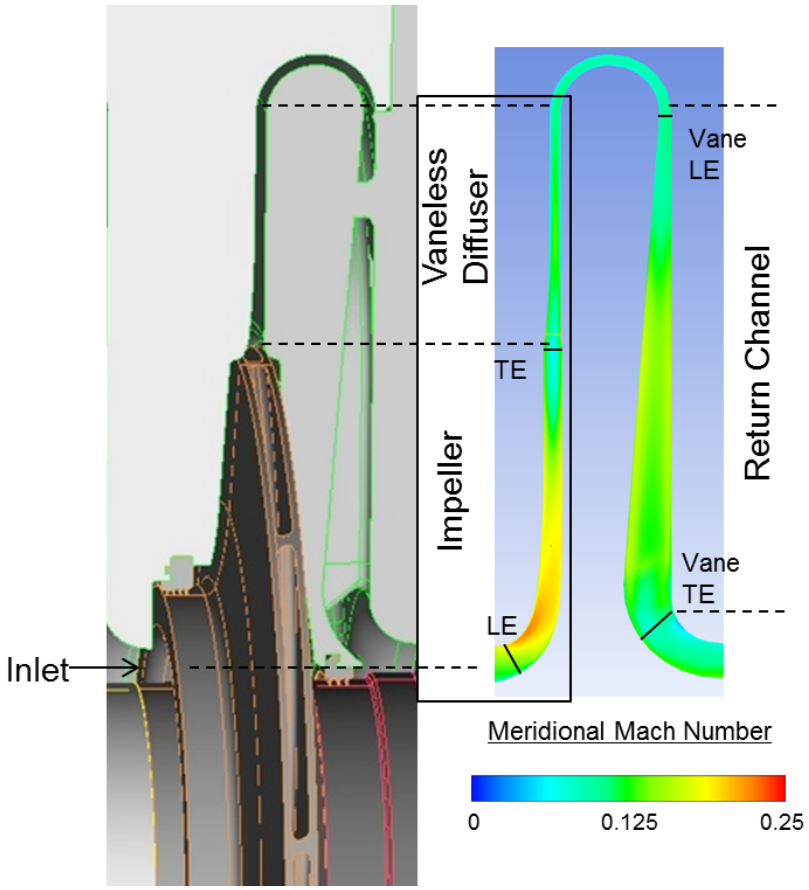

Figure 4-9: Geometry of the candidate compressor stage.

and real gas CO_2 using the LK EOS model. To ensure identical Reynolds number of about 10^7 for the two cases the viscosity of the ideal gas is modified to match that of the real gas. The compressor characteristics are shown in Fig. 4-10. The performance metrics are normalized by their values at the design point.

For dynamically similar cases, meaning the same Re, M_{U_2}, and ϕ, the results indicate identical performance between ideal and real gas simulations over most of the operating range of the compressor . As discussed in Chapter 3, the gradients of the compressibility factor are almost orthogonal to the polytropic process yielding no significant change in Z through the stage. The pitchwise averaged distribution of Z along the meridional direction is depicted in Fig. 4-11. The compressibility factor increases by less than 2% from its value at the inlet when the compressor is operating at the maximum efficiency point. At this scale, variations in real gas properties have

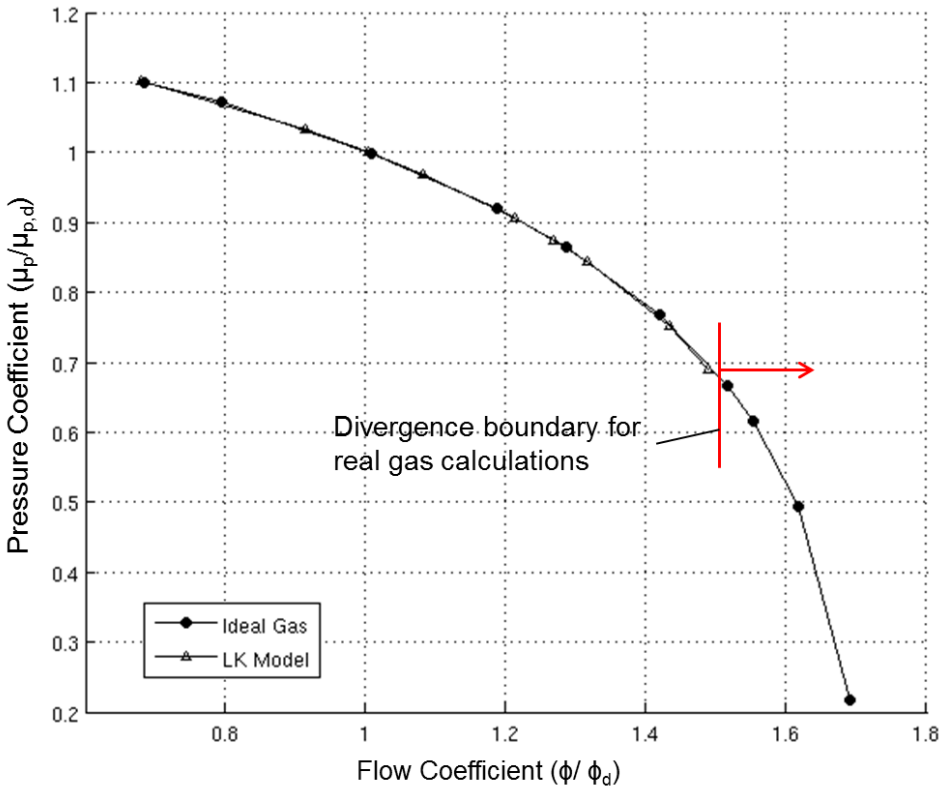

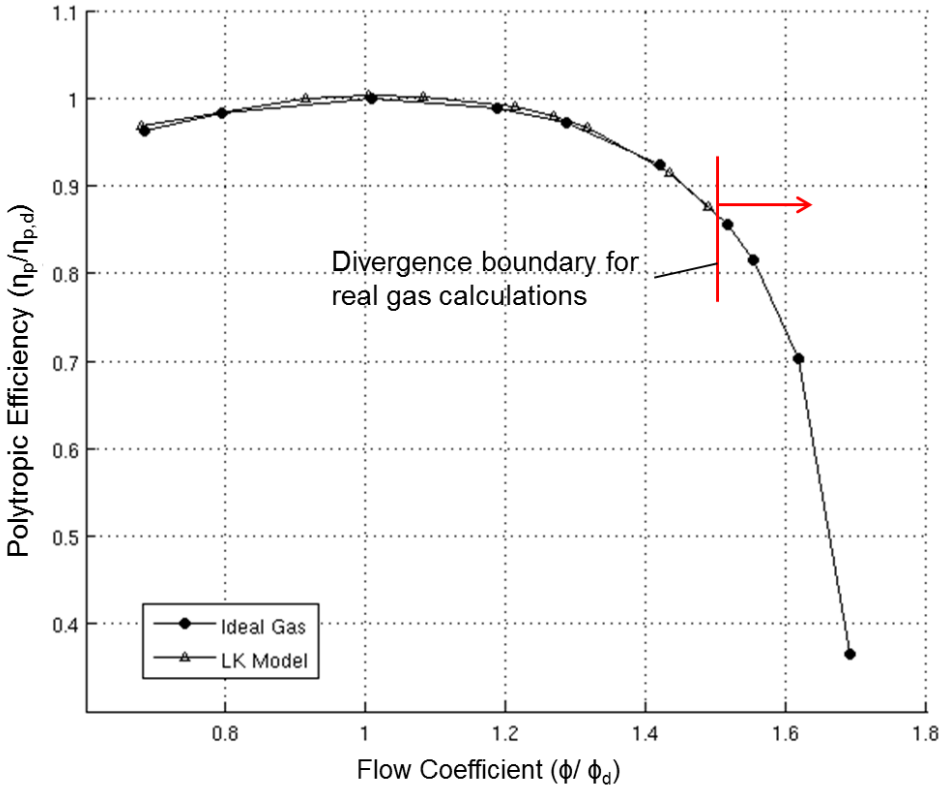

Figure 4-10: Real gas effects have no impact on pressure coefficient (top) and polytropic efficiency (bottom) at current operating conditions.

negligible impact on the compressor performance.

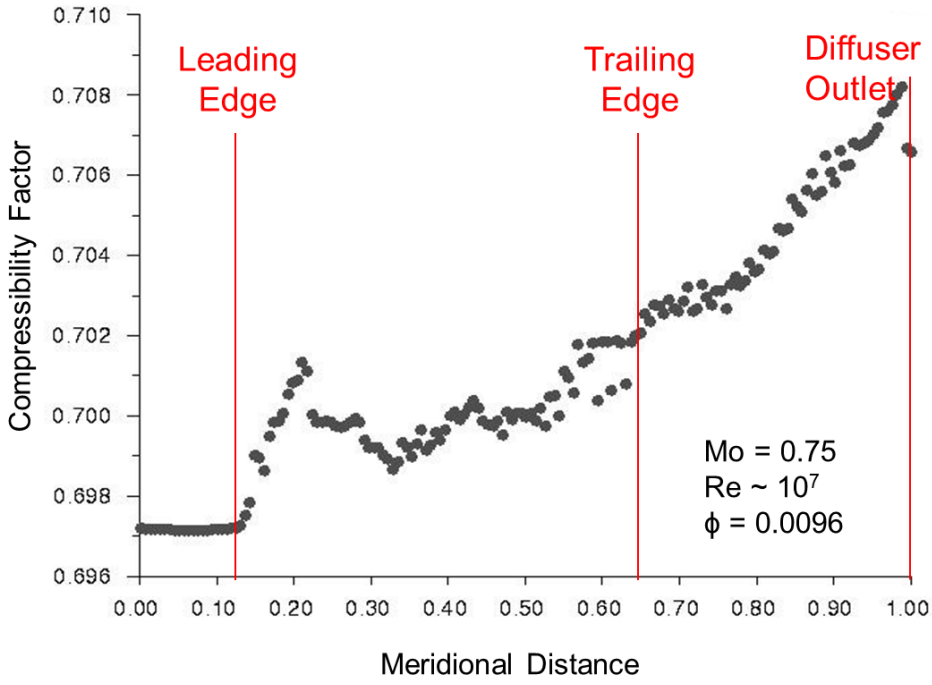

Figure 4-11: Distribution of pitchwise averaged Z through the stage.

As Figure 4-10 indicates however, the real gas simulations abruptly diverge for flow coefficients $\phi/\phi_d > 1.45$. This is further investigated next.

4.4.3 Flow Behavior Near Choke Conditions

The divergence in real gas calculations occurs at high flow coefficients near the choke limit of the compressor. At these conditions the impeller is subjected to a highly negative incidence angle at the leading edge. The stagnation point moves towards the suction side of the blade and the flow accelerates around the leading edge, forming a supersonic region on the pressure side. Figure 4-12 shows a 3D view of the supersonic patch along the span of the leading edge and a close-up view of the Mach field in the mid-span plane.

Because of the 3D shape of the blade, close to the inlet the flow velocities are higher near the shroud and the supersonic region is more prominent there. As the flow accelerates, the static pressure and temperature of the fluid decrease significantly

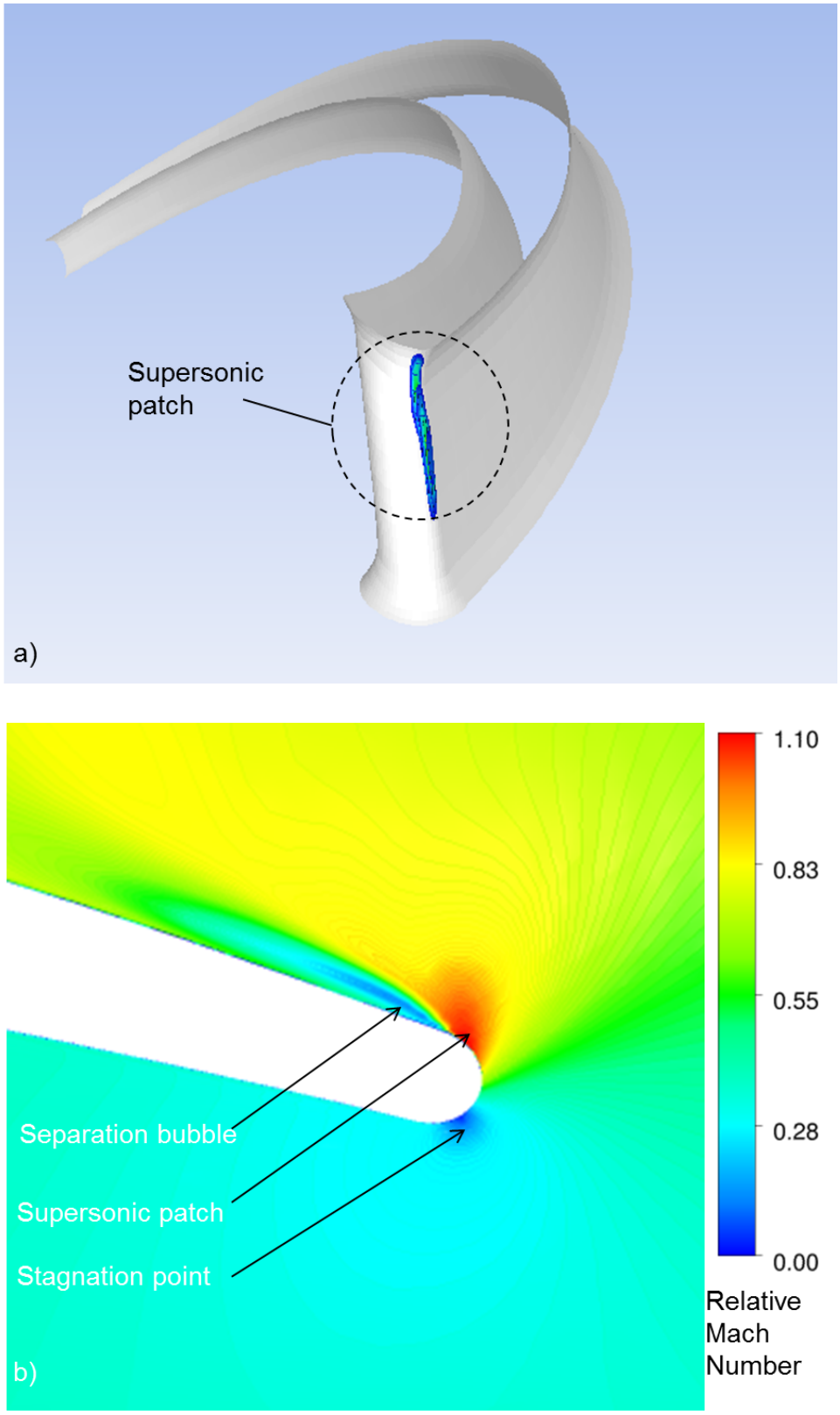

Figure 4-12: Supersonic patch due to negative incidence angle at $\phi/\phi_d = 1.45$: a) along the impeller blade, b) mid-span cross-section.

and eventually fall below the saturation curve. In a single phase calculation, the real gas model immediately returns the liquid properties of the fluid, which the solver interprets as divergence due to the discontinuous change. Even though this effect is limited to a small region near the leading edge of the impeller, it suggests the need to investigate the possibility of condensation occurring inside the compressor. This is discussed in Chapter 5.

4.5 Summary

This chapter presents several concepts related to the performance of centrifugal compressor stages. The nomenclature and performance metrics introduced here are used throughout the remainder of this thesis. A discussion of the design implications for low flow coefficient stages, required for supercritical CO_2 applications, is included. A canonical turbomachinery test case is analyzed using a 2D radial impeller and vaneless diffuser, before extending the CFD simulations to the actual compressor stage. In both cases, comparison between ideal and real gas calculations show identical overall performance and flow field features, provided that dynamic similarity is preserved. The main take-away is that at the current operating conditions of the compressor real gas effects have no significant impact on performance and matching, confirming the hypothesis of Chapter 3. Real gas simulations at flow coefficients close to the choke limit of the compressor however, suggest the possibility of condensation occurring due to local flow acceleration near the impeller leading edge. A detailed investigation is performed in the following chapter before the compressor performance is examined at different thermodynamic conditions closer to the empirical safety margin. This is discussed in Chapter 6.

Chapter 5

Effects of Condensation on CO_2 Compressor Performance

The problem of condensation in turbomachinery has been studied extensively for steam turbines, where significant amount of the flow undergoes a phase change as it expands through the turbine stages. This phenomenon however, is uncommon in compressors where the polytropic process moves away from the two-phase dome. Nevertheless, conditions for condensation can be attained due to local flow acceleration such as for example around the impeller leading edge, as shown in Chapter 4 for the supercritical CO_2 compressor stage. Reaching saturation conditions does not necessarily mean that the fluid condenses. In high speed flows nucleation usually occurs under non-equilibrium conditions where the rate of droplet formation depends on the magnitude of the departure from the equilibrium state. The objective of this study is to establish a non-dimensional criterion that determines the relative importance of two-phase flow effects and to assess the impact of non-equilibrium thermodynamic conditions on the candidate compressor stage performance.

5.1 Losses Associated with Condensation

Three types of loss mechanisms are associated with condensation in turbomachinery. Losses due to the friction between the droplets and the gas phase of the fluid are

usually referred to as kinematic relaxation losses. Another loss mechanism is the breaking loss resulting from the impacts of droplets onto the moving blades. Part of the work input by the impeller is absorbed in the impact and does not go into raising the pressure of the fluid. The third loss mechanism is the thermodynamic wetness loss which occurs during the formation of the liquid phase under non-equilibrium conditions. The difference between equilibrium and non-equilibrium condensation can be described using the p-T diagram in Fig. 5-1.

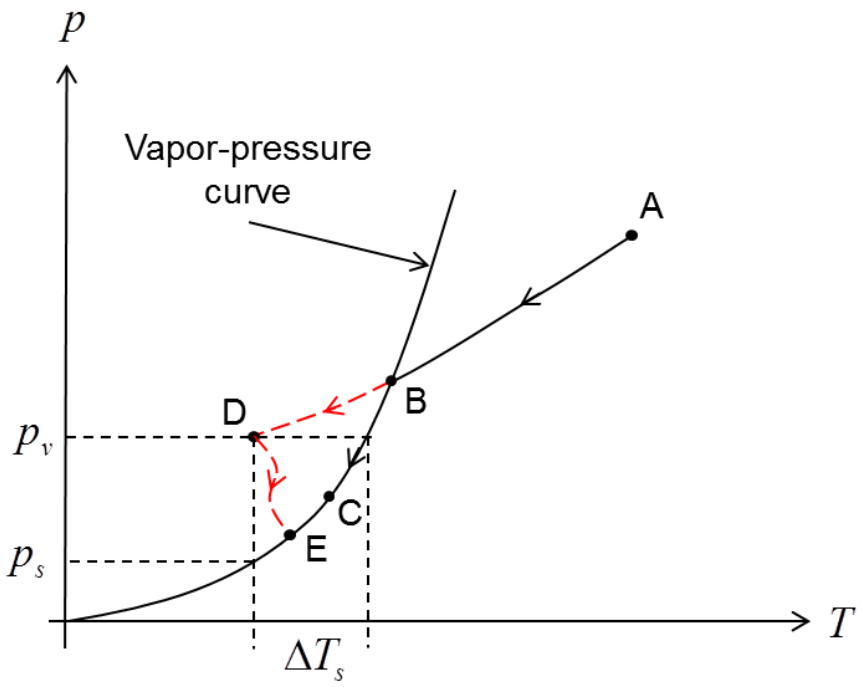

Figure 5-1: Equilibrium (ABC) and non-equilibrium (ADE) flow expansion through the vapor-pressure curve.

Following an expansion process starting from point A, a fluid eventually reaches saturation conditions (point B). If the expansion proceeds in equilibrium state, droplets would begin to form and the process would continue along the vapor-pressure curve towards point C. In this case, even though there is an entropy change for both the liquid and vapor phases, there is no net entropy generation for the two-phase mixture due to condensation.

Numerous experimental measurements however, reveal that condensation might not occur in equilibrium and the expansion process can actually continue through the

vapor pressure curve towards point D. At these conditions the fluid is in a metastable phase, which is characterized by the temperature difference relative to the corresponding equilibrium state, referred to as supercooling ΔT_s, or alternatively by the ratio of the fluid pressure to the equilibrium pressure, referred to as supersaturation $S = p_v/p_s$. When the level of supercooling (or supersaturation) reaches a certain threshold, droplets begin to form and the fluid reaches a stable state along the vapor-pressure curve, designated by point E in Fig. 5-1. There is net entropy generation associated with this process due to the finite temperature difference. The final state is at a lower pressure and temperature compared to the one for equilibrium condensation. This theory is discussed in greater detail in [29].

The thermodynamic wetness loss accounts for 20% to 45% of the overall condensation losses, as reported by Gyarmathy [30], and up to 6.5% of the total loss for the steam turbine analyzed by Starzmann and Casey [31]. A reliable prediction of the thermodynamic wetness loss would require numerical models for the nucleation rate (rate of droplet formation) and droplet growth rate. The classical nucleation model, used extensively for steam, is presented in the following section.

5.2 Review of Classical Nucleation Theory

The energy required for condensation can be expressed in the form of the Gibbs free energy, which is a thermodynamic potential representing the useful work that can be obtained from a system at constant pressure and temperature. The governing equations describe the mechanism through which nucleation occurs. In homogeneous nucleation, clusters of molecules form in the interior of a uniform substance, while in heterogeneous nucleation, nuclei form at the interfaces between particles of different species. Because the content of CO_2 in the last block of the supercritical CO_2 compressor is estimated to be 99.8%, any condensation inside the candidate compressor stage can be considered homogeneous.

Using the assumption that the nuclei of the liquid phase have spherical shape, the change in the Gibbs free energy can be written as

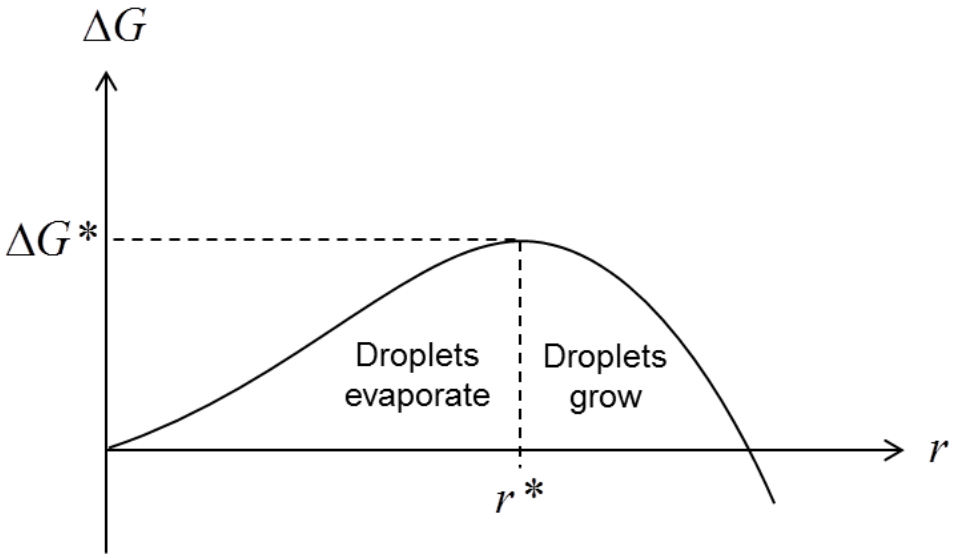

Figure 5-2: Critical radius for droplet growth in non-equilibrium condensation.

$$\Delta G = 4\pi r^2 \sigma - \frac{4}{3}\pi r^3 \rho_l \left[g\left(p_v, T\right) - g\left(p_s, T\right) \right] \tag{5.1}$$

where g is the specific Gibbs free energy and σ is the surface tension. The first term on the right-hand side of Eq. 5.1 represents the energy required to form the droplet surface and is proportional to r^2, while the second term represents the energy release associated with the formation of the liquid phase and is proportional to r^3. For small r, the quadratic term outweighs the cubic term, which induces an energy barrier. The nuclei are unstable and evaporate instantaneously. For a critical radius r^* the change in Gibbs free energy reaches a maximum at which point the nuclei become stable and the droplets can grow. This is represented schematically in Fig. 5-2. Using $\frac{dG}{dr} = 0$ yields an expression for the critical radius

$$r^* = \frac{2\sigma}{\rho_l \left[g\left(p_v, T\right) - g\left(p_s, T\right) \right]} \quad . \tag{5.2}$$

Substituting Eq. 5.2 into 5.1 gives

$$\Delta G^* = \frac{4}{3}\pi r^{*2} \sigma \quad . \tag{5.3}$$

The term ΔG^* is a measurement of the limiting energy barrier for which nuclei

can grow and is dependent on the level of supersaturation of the fluid. For an ideal gas the change in specific Gibbs free energy is related to the supersaturation via

$$g\left(p_v, T\right) - g\left(p_s, T\right) = RTln(p_v/p_s) \quad . \tag{5.4}$$

Eq. 5.4 can be used in the nucleation models for steam, but does not apply to CO_2 at near-critical conditions where its deviation from ideal gas behavior is significant. For a real gas, the change in Gibbs free energy is given by

$$g\left(p_v, T\right) - g\left(p_s, T\right) = \left[h\left(p_v, T\right) - Ts\left(p_v, T\right)\right] - \left[h\left(p_s, T\right) - Ts\left(p_s, T\right)\right] \quad . \tag{5.5}$$

In any case, the higher the supersaturation is the lower ΔG^* is, and the easier it is for liquid droplets to form. In classical nucleation theory, the nucleation rate J is represented as a Boltzmann-like distribution function of the form

$$J = \left[\sqrt{\frac{2\sigma}{\pi m^3}}\frac{\rho_v^2}{\rho_l}\right] e^{\left(-\frac{\Delta G^*}{\kappa T}\right)} \tag{5.6}$$

where m is the mass of a single molecule of the fluid and κ is the Boltzmann's constant.

Eq. 5.6 has been used extensively for modeling steam applications, however work in literature on non-equilibrium condensation of CO_2 is limited to much lower pressures than those of the candidate compressor stage. Li et al [32] show that Eq. 5.6 is in good agreement with experimental measurements of nozzle flow of CO_2 at pressures of up to 3 bar.

Classical nucleation theory can be used to define a relative time scale ratio that determines weather the departure from equilibrium conditions in an internal flow situation is significant enough for stable liquid droplets to form. This concept is described in more detail and applied to the candidate compressor stage in Section 5.4. Before the analysis can be conducted however, the modeling of metastable properties of CO_2 needs to be considered.

5.3 Modeling of the Metastable Phase of CO_2

Modeling non-equilibrium condensation requires an estimation of the fluid properties at metastable conditions. As metastable properties have not been measured experimentally, this is usually handled by extrapolating the gas properties onto the liquid domain. A similar technique has been extensively used for steam and it is employed in the IAPWS-97 database of steam properties, but to the authors knowledge no such database has been published for CO_2. In the study of condensation in plumes at pressures of up to 3 bar by Li et al [32] the saturation pressure of CO_2 given by Span and Wagner [19] was used, but the gas phase was treated as an ideal fluid. A more relevant study of a centrifugal compressor stage, operating with CO_2 near the critical point, is presented by Pecnik et al [17]. While the authors point out that flow acceleration around the leading edge leads to pressure levels below the saturation line, they treat the fluid inside the two-phase region in equilibrium condition. In the present study, a MatLab subroutine is created to generate a database with the vapor and supercritical properties of CO_2 using the LK model and extrapolate them onto the liquid domain, as shown in Fig. 5-3, using enthalpy as an example.

The particular structure of the database follows the requirements of ANSYS CFX for the description of user-defined fluids through real gas property (RGP) tables. A description of the liquid properties is provided in a separate RGP file for use in CFD calculations.

5.4 Numerical Simulations Setup

It was shown in Chapter 4 that for $\phi/\phi_d = 1.45$ and $M_{U_2} = 0.75$ the local flow acceleration around the impeller leading edge causes the thermodynamic conditions to reach the vapor-pressure curve. To gain insight into the condensation process another set of simulations is performed using ANSIS CFX, where the metastable condition is handled by the method described in the previous section. The solver setup and turbulence model are similar to the ones previously discussed in Chapter

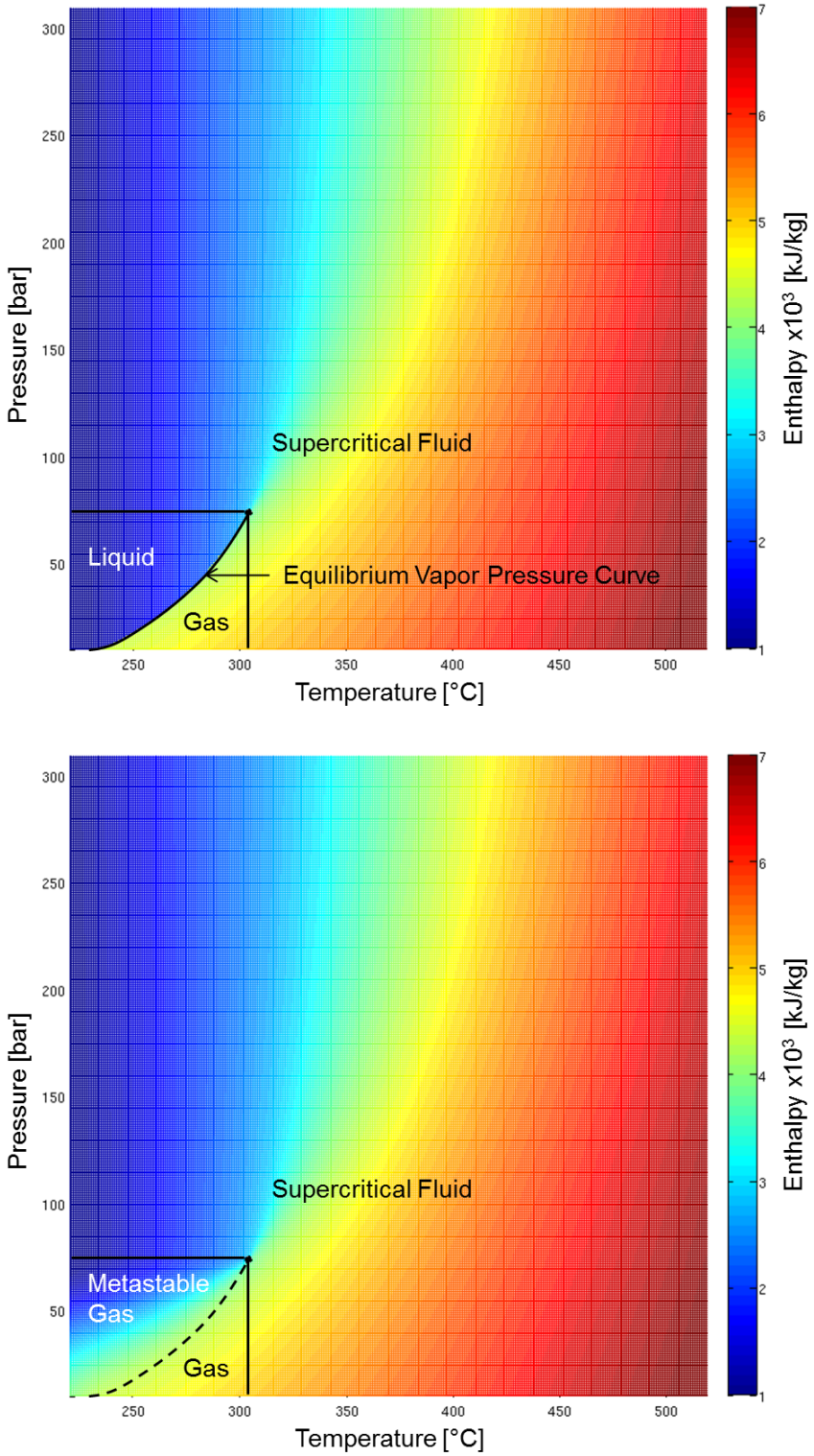

Figure 5-3: Enthalpy of CO_2 provided by the EOS model (top) is amended with the metastable phase by extrapolating the gas property onto the liquid domain (bottom).

4. The mesh required for this solver is generated automatically with TurboGrid from the candidate stage geometry. The boundary layers are represented with 10 cell layers and a $y+$ value of 1, as required by the turbulence model to accurately capture viscous effects. The mesh size is targeted at 10^6, yielding a grid that is similar to the one used in FLUENT.

The total pressure at the inlet boundary is kept the same at 68.27 bar, while the total temperature was reduced by 10 K to 318 K. A lower temperature moves the operating conditions of the compressor closer to saturation, representing a worst case scenario for the candidate stage. The change in stagnation inlet temperature yields a negligible change in the Reynolds number ($Re \sim 10^7$). A pressure boundary with targeted mass flow rate is used at the outlet. The rotating speed and target mass flow rate are adjusted to maintain the same ϕ and M_{U_2} as in the simulation in Chapter 4.

5.5 Assessment of Condensation

A two-phase calculation is performed by introducing liquid CO_2 as a dispersed phase. A source term, given by Eq. 5.6, is added to the equations of motion to take into account the phase change. The exact form of the Eulerian-Lagrangian formulation of the governing equations, as well as the model for droplet growth rate are provided in [33]. The results show a negligible mass fraction of liquid CO_2 of 10^{-9} and no significant impact on the compressor performance. To confirm these findings, a single-phase simulation is performed using RGP tables with metastable CO_2 properties. The region around the impeller leading edge where thermodynamic conditions are below the saturation line is shown in Fig. 5-4.

Two time scales related to the condensation process can be extracted from the CFD results. A measure of the time required for stable droplets to form can be defined by

$$t_n = \frac{1}{J_{max} V} \tag{5.7}$$

where V is the volume of condensing CO_2 shown in Fig. 5-4 and J_{max} is the maximum

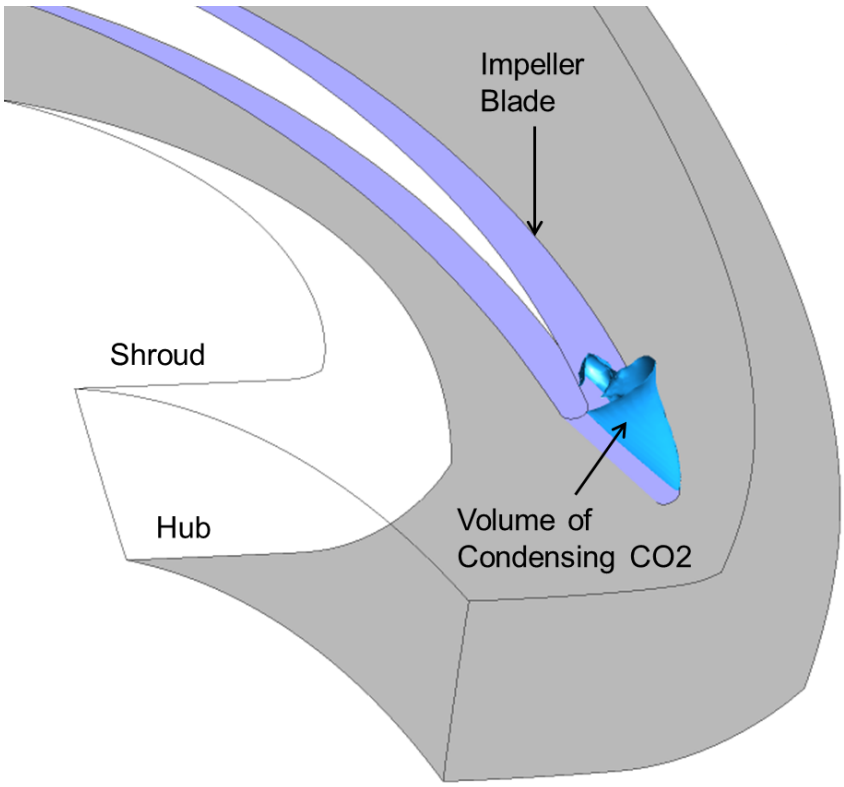

Figure 5-4: Volume of metastable fluid near the impeller LE at $\phi/\phi_d = 1.45$ and $M_{U_2} = 0.75$.

nucleation rate given by Eq. 5.6. This time scale can be compared to the residence time of the flow, which is defined as

$$t_r = \frac{l}{c_{ave}} \tag{5.8}$$

where l is the length of the condensing volume along the blade's camber line and c_{ave} is the average flow velocity. The non-dimensional ratio t_r/t_n relates the level of supersaturation of the fluid to the flow field. For the candidate compressor stage, the time scale ratio is found to be $t_r/t_n = 0.01$, meaning that the time required for stable liquid droplets to form is significantly larger than the residence time of the flow inside the nucleating region. As a consequence, the level of supersaturation of the fluid is not large enough to induce significant phase change. The implication for the compressor is that condensation due to local flow acceleration around the impeller leading edge is not a concern at the current operating conditions of the stage.

Moving closer to the critical point however, the expansion across the saturation line becomes more significant while the surface tension of the fluid asymptotically approaches zero, which suggests a significant increase in the nucleation rate such that $t_r/t_n > 1$. As a result, condensation is expected to become an issue and it may need to be accounted for in the analysis of the compressor stage through two-phase flow simulations. The limitations of this analysis are related to the validity of the classical nucleation model in the vicinity of the critical point. Due to the increased coalescence of molecules Eq 5.6 is expected to underestimate the nucleation rate at these conditions. The numerical simulation models may need to be supplemented by experimental measurements, as discussed in Chapter 7.

5.6 Summary

This chapter provides a brief discussion on the mechanisms and governing equations for non-equilibrium homogeneous condensation. A set of numerical simulations is presented that incorporates the classical nucleation model to investigate the effects of two-phase flow on the candidate compressor stage. The CFD results show that condensation is not a concern at the current operating conditions because the time required for stable liquid droplets to form is significantly larger than the residence time of the flow inside the nucleating region. An important implication is that two-phase flow simulations are not required when the condensation time scale ratio $t_r/t_n << 1$. The compressor performance can be predicted using single-phase simulations as long as the EOS model is amended with the metastable properties of the fluid.

Approaching the critical point however, liquid phase becomes much more likely to form than predicted by classical nucleation theory, and the potential impact on a compressor stage is still unknown. Before the analysis of the compressor performance can be extended to the vicinity of the critical region, it is useful to examine the effects of the variation in real gas properties independent of condensation. This investigation is presented in the following chapter.

Chapter 6

Compressor Performance Approaching the Critical Point

As discussed in the previous chapters, real gas effects have no significant impact on compressor performance and matching at the current operating conditions of the candidate stage. Approaching the critical point however, the departure from ideal gas behavior of CO_2 becomes more significant. It was shown in Chapter 3 that the increase in the isentropic exponent causes a decrease in the maximum corrected mass flow per unit area, leading to the hypothesis that the compressor may choke sooner than expected. Numerical simulations are performed on the candidate stage at different thermodynamic conditions to quantify the impact of the variations in real gas properties on the compressor performance and stage matching.

6.1 Scope of Investigation

The operating conditions of the candidate compressor stage are varied by changing the stagnation state at the inlet similar to the procedure for the converging nozzle study outlined in Chapter 3. Starting from the inlet conditions to the second stage of the supercritical CO_2 compressor ($p_t = 93.5$ bar, $T_t = 357$ K), the safety margin is approached by increasing the pressure along a constant temperature line, as shown in Fig. 6-1. At the inlet conditions to second stage the gradients in the compressibility

factor are almost orthogonal to the polytropic process and the isentropic exponent has a value of about 1.4, similar to air at ideal gas conditions. In addition, the inlet state is further away from the saturation line, such that significant excursion into the two-phase region is avoided when approaching the critical point, where the variations in real gas properties become more significant. The inlet stagnation states where the compressor performance is assessed are marked with black circles. The intermediate state is at a pressure of 120 bar, while the final state corresponds to 140 bar.

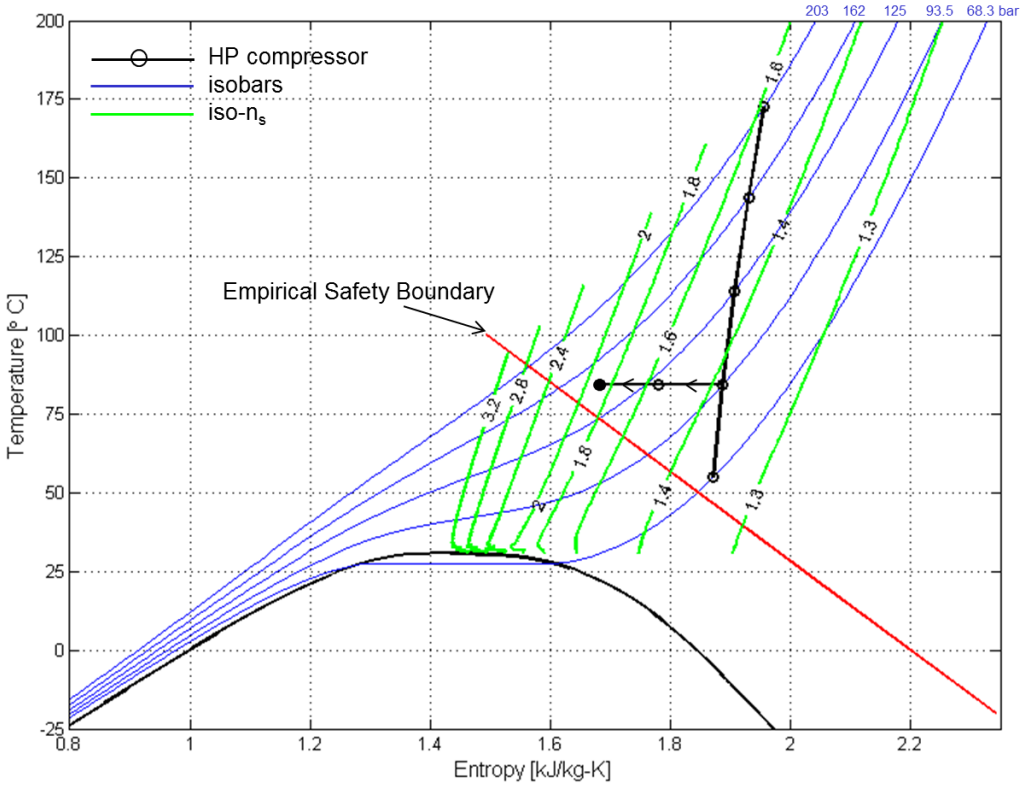

Figure 6-1: Moving 2nd stage compressor inlet conditions towards the empirical safety margin.

The CFD calculations are performed in ANSYS CFX using a similar setup as the one previously discussed in Chapter 5. The change in the inlet conditions yields a negligible change in Reynolds number, such that the mesh does not require further refinements. The rotational velocity is adjusted between the three cases to maintain machine Mach number of $M_{U_2} = 0.8$, and for each case the back pressure is varied to generate the performance characteristics, which are presented in the following section.

Simulations for high flow coefficients at both $p_t = 120$ bar and $p_t = 140$ bar show that local flow acceleration around the leading edge causes the thermodynamic conditions to reach below the vapor-pressure curve. This is handled by amending the EOS model with metastable properties of CO_2, as described in Chapter 5. The nucleation time scale ratio in all cases is found to be on the order of 10^{-2}, meaning that condensation is not a concern and two-phase flow simulations are not necessary.

6.2 Overall Compressor Performance

The pressure coefficient and the polytropic efficiency of the stage are calculated via Eq. 4.5 and 4.8 using mass flow averaged quantities from the CFD results. The performance metrics are normalized by the design point values and the characteristic curves for the three operating conditions are presented in Fig. 6-2.

The results suggest an increased sensitivity of the compressor performance to fluctuations in the mass flow rate at high flow coefficients approaching the empirical safety line. Near the choke limit at the current operating conditions, a change in the flow coefficient of $\Delta\phi = 2.5\%$ corresponds to a change in efficiency of $\Delta\eta = 3\%$. Due to the larger isentropic exponent near the safety line, the same change in flow coefficient would yield $\Delta\eta = 7\%$. The choke margin of the stage is reduced by 9%, which supports the hypothesis stated in Chapter 3.

Furthermore, the increase in n_s impacts the matching of downstream components in a multistage configuration. The swings in corrected mass flow per unit area at the current operating conditions are compared to the ones approaching the safety line as shown in Fig. 6-3. For the larger isentropic exponent, the swing between inlet and outlet corrected mass flow per unit area increases by 5%. An excursion in the corrected mass flow function at the inlet of the stage leads to a more significant excursion at the outlet compared to the design conditions. As a result, the operating point of the downstream stage will move away from its design condition yielding a reduced pressure rise. This effect gets amplified through the following stages and may lead to choking of the machine.

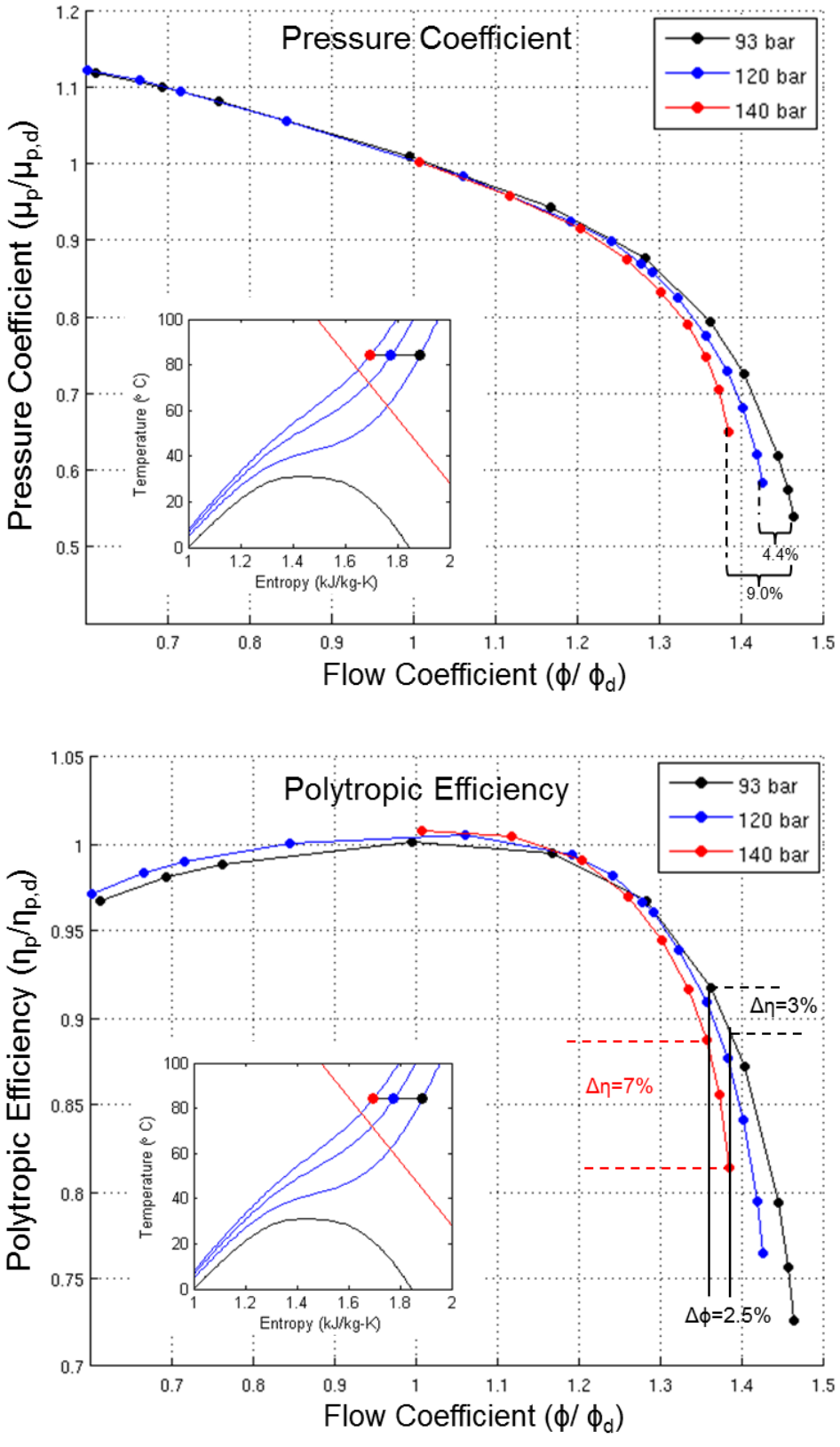

Figure 6-2: Decrease in compressor choke margin near empirical safety limit observed in pressure coefficient (top) and polytropic efficiency (bottom) characteristics.

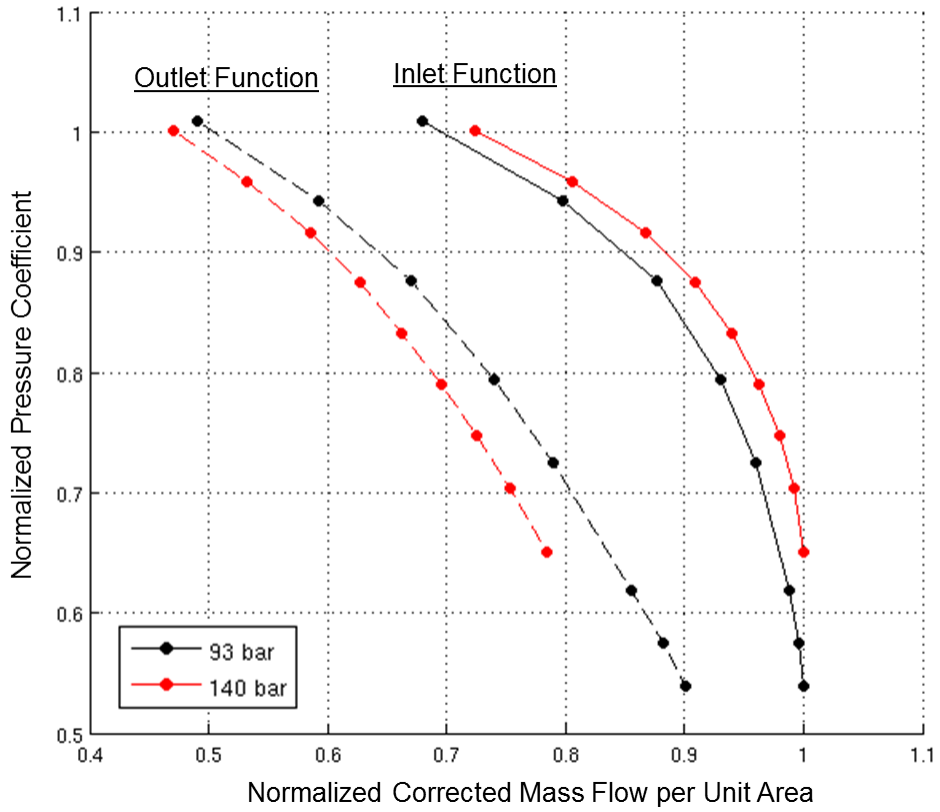

Figure 6-3: Larger swing between inlet and outlet corrected mass flow due to increasing n_s.

6.3 Flow Field Comparison Near Choke Conditions

The effects of the increase in isentropic exponent on the flow field at high flow coefficients for the three cases is assessed next. Contour plots of the relative Mach number distribution along the 85% span plane for the three different inlet pressures are shown in Fig. 6-4. The increase in the isentropic exponent causes greater bulk flow acceleration at high flow coefficients. This effect is expected to have even larger impact beyond the empirical safety margin, where the gradients in n_s become significantly steeper.

In all three cases, a large separation zone is observed along the pressure side of the blade that originates near the impeller leading edge. This 3D flow feature can be explained by examining more closely the flow behavior along the span of the blade. The high negative incidence angle causes the flow to become supersonic as it

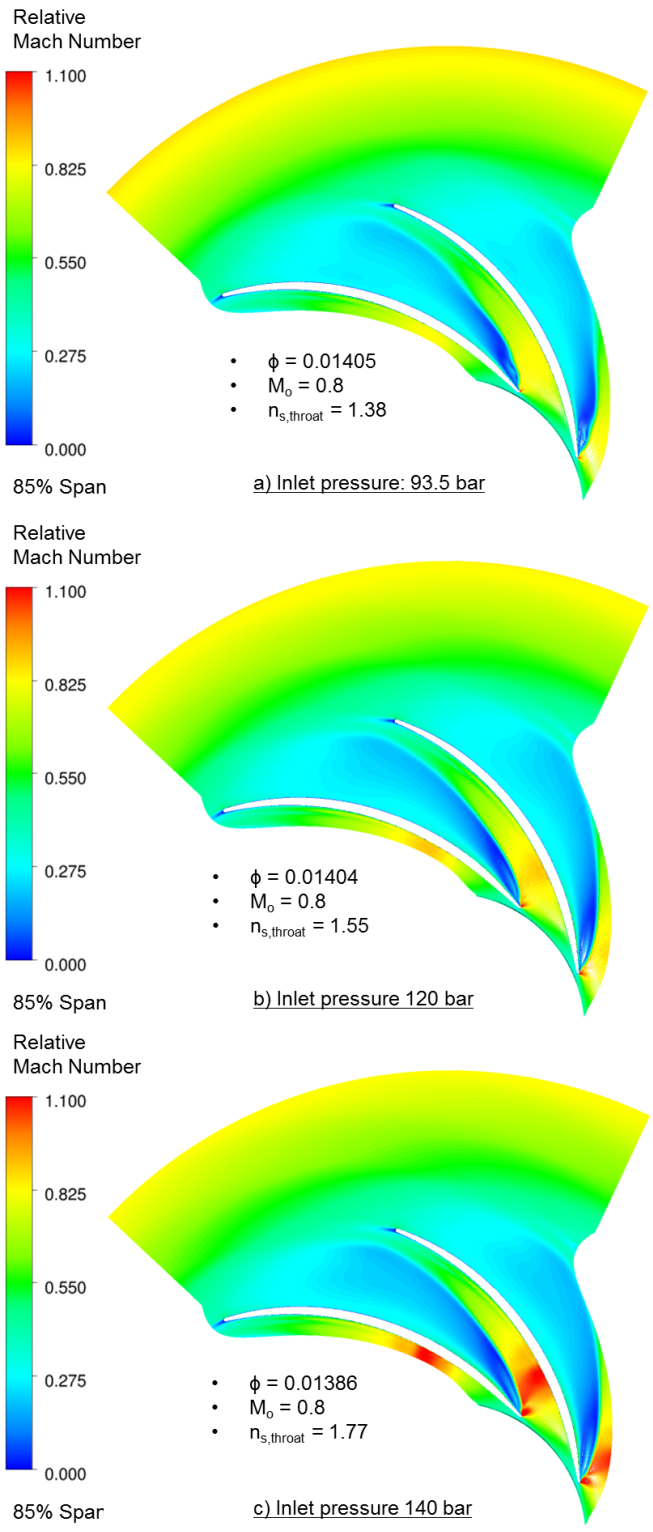

Figure 6-4: Effect of increasing isentropic exponent on flow field for total inlet pressures of a) 93.5 bar, b)120 bar, c) 140 bar

accelerates around the LE. The turning of the flow and the twist of the blade lead to a shock induced separation near the shroud as observed in the meridional cut at 1% blade chord in Fig. 6-5.

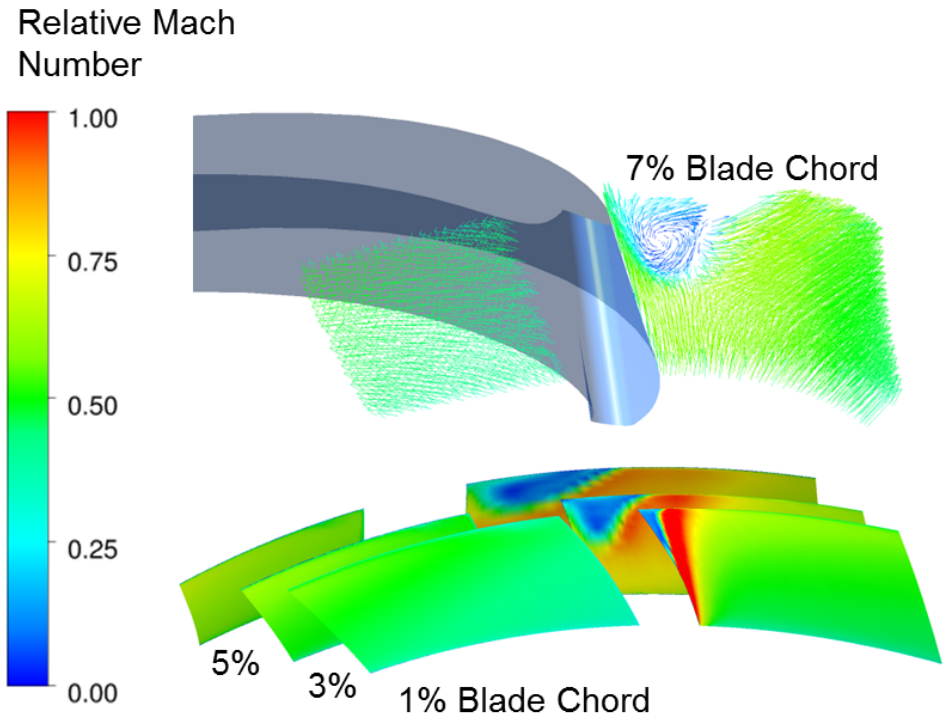

Figure 6-5: Shock induced separation near LE at $\phi/\phi_d = 1.36$

The separation region grows downstream causing significant blockage near the shroud. A strong shear layer forms between the separated region and the main flow. The stability of the shear layer is analyzed through an unsteady simulation presented in the following section.

6.4 Kelvin-Helmholtz Instability in Blade Passage

The steady state CFD results for $\phi/\phi_d = 1.36$, presented in the previous section, are used as an initial condition for an unsteady simulation to investigate the behavior of the shear layer. The time step for the calculation is adjusted to achieve a Courant number less than 1 inside the blade passage. The boundary conditions are carried over from the steady state simulation such that no disturbances are introduced in

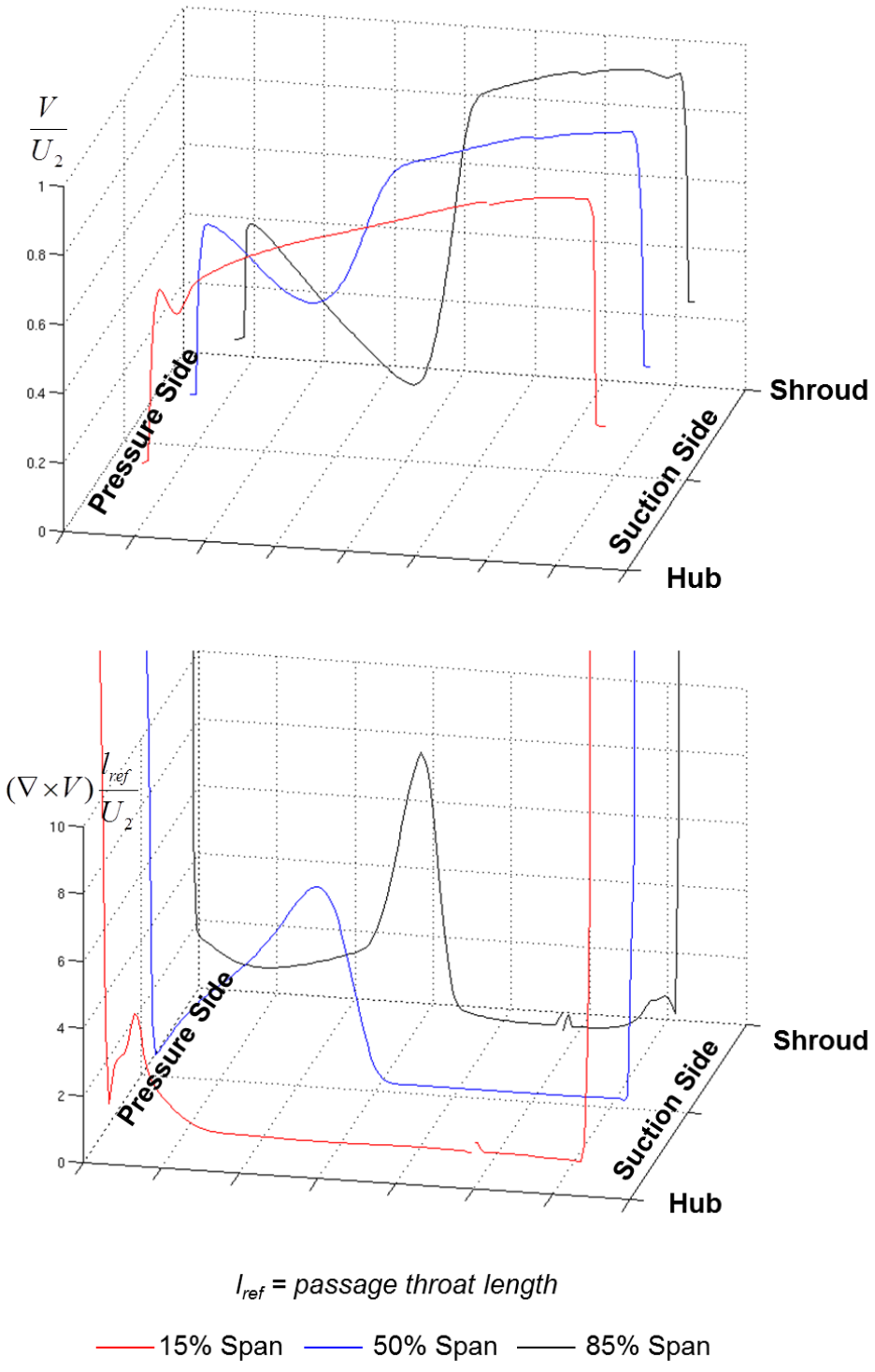

Figure 6-6: Inflection point in the velocity profile of the shear layer (top) with a corresponding maximum in vorticity profile (bottom) are necessary conditions for Kelvin-Helmholtz instability.

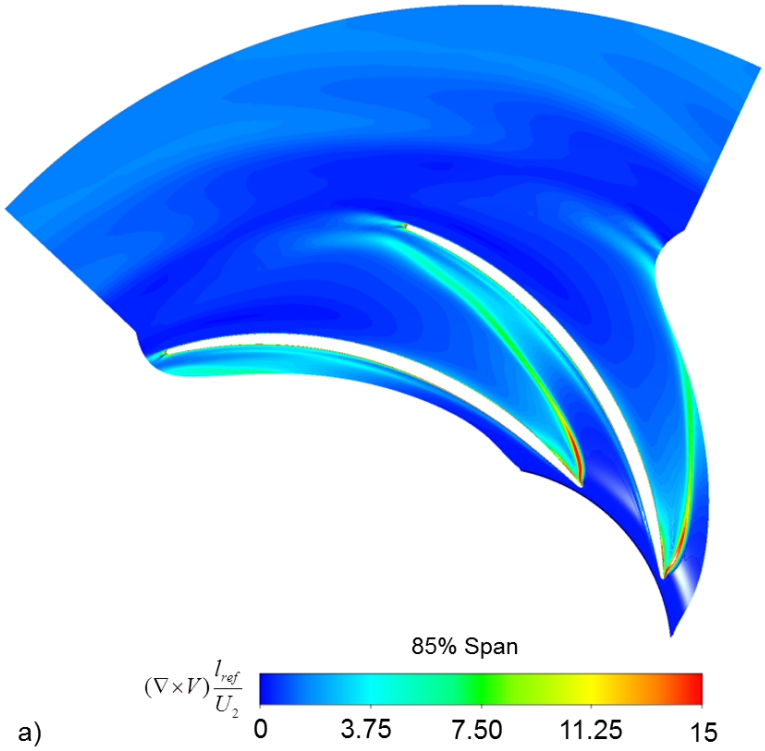

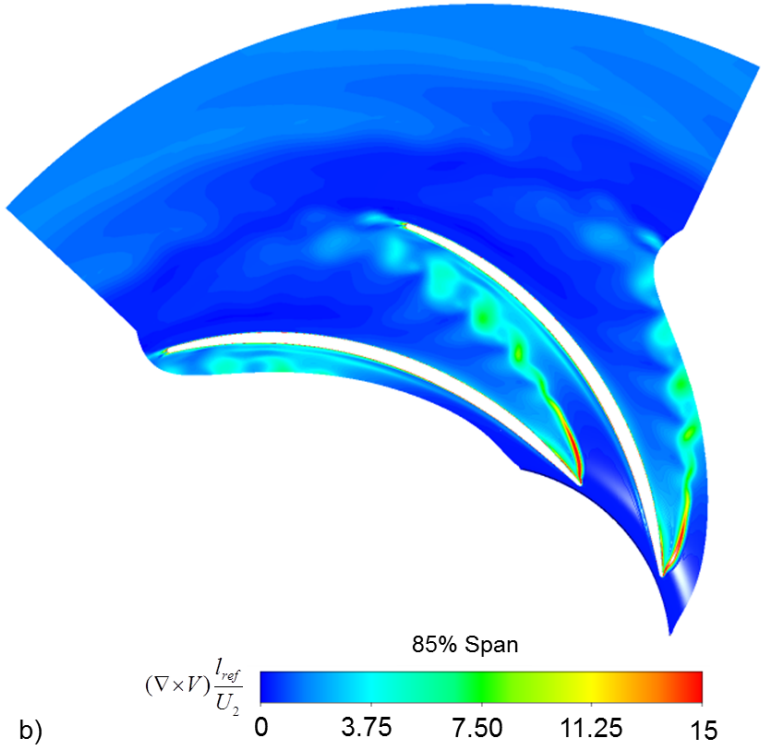

Figure 6-7: Vorticity field for $\phi/\phi_d = 1.36$ at a) initial time and b) one impeller revolution.

the flow from the boundaries. Time-averaged statistics of the flow field quantities are collected and the normalized velocity and vorticity profiles across the blade passage are shown in Fig. 6-6.

A strong inflection point in the velocity profile, with a corresponding peak in the vorticity profile, is observed. These are necessary conditions for a Kelvin-Helmholtz type instability to occur. A detailed derivation of this theorem by considering the behavior of small disturbances in an inviscid, constant density flow is provided by Greitzer et al in [25]. Shear layers with an inflection point can be stabilized by viscosity at low enough Reynolds numbers, but the values needed are several orders of magnitude lower than those of the supercritical CO_2 compressor. In the case of the candidate compressor stage, weak vortices shed from the impeller trailing edge create a pressure perturbations that travel upstream causing a disturbance in the shear layer. The evolution of the disturbance can be tracked using the time-accurate solutions from the unsteady computations. The unperturbed vortex sheet at t=0 eventually rolls up and begins to shed discreet vortices, as shown in Fig. 6-7.

6.5 Summary

This chapter presents the investigation of the impact of variations in real gas properties approaching the critical point on compressor performance and stage matching. Numerical simulations are conducted of the candidate compressor stage operating at different thermodynamic conditions. The performance characteristics of the stage are compared at three operating points chosen to be progressively closer to the critical point. The results indicate that the choke margin of the compressor is reduced by 9% as the isentropic exponent increases. Furthermore, the matching of compressor stages can be impacted as the swing in corrected mass flow per unit area between inlet and outlet increases. Investigating the flow field near the leading edge reveals that shock induced separation occurs at high flow coefficients. Strong shear layer with inflection point in the velocity profile forms between the separated region and main flow. The evolution of the resulting Kelvin-Helmholtz instability, promoted by

the high Reynolds number typical of supercritical CO_2 compressors, is investigated with unsteady CFD calculations.

Chapter 7

Conclusions

This thesis presents a comprehensive assessment of real gas effects in supercritical CO_2 compressors. While the main focus is on investigating the root cause for performance and stability issues reported near the critical point, the proposed framework serves as a foundation for the advanced study of the internal flow behavior of real fluids. A qualitative analysis from first principles is used to identify potential mechanisms for performance and stability issues before conducting numerical simulations to quantify their effect on a centrifugal compressor stage. The major contributions of this investigation are summarized next, followed by a discussion on recommendations for future work.

7.1 Thesis Contributions

The contributions of this thesis can be summarized into concepts and methods used to analyze the internal flow behavior of real fluids, and specific findings related to the performance and operation of the supercritical CO_2 compressor stage. The key concepts and methods include:

1. The compressible flow relations and influence coefficients for 1-D channel flow of a real gas were derived. These were used to assess trends in the gas dynamic behavior of real fluids, such as the inversion of gas dynamic effects and the variations in corrected mass flow per unit area.

2. The behavior of real gas properties, such as the compressibility factor Z and the isentropic exponent n_s, was examined to identify the thermodynamic conditions where real gas effects are expected to be prominent. For variations in n_s of less than 6% the compressible flow relations derived in Chapter 3 yield an error of less than 1%.

3. A non-dimensional criterion was established that determines whether two-phase flow effects are present in a particular flow situation. It relates the time required for stable liquid droplets to form, which depends on the expansion through the vapor-pressure curve, and the residence time of the flow under saturation conditions. Two-phase flow effects can be considered negligible when the ratio of the two time scales is much smaller than unity. The implication is that two-phase flow simulations are not required as long as the EOS model is amended with the metastable properties of the fluid.

The specific findings that relate to CO_2 and the candidate compressor stage include:

1. The fundamental derivative of CO_2 is shown to remain positive in the region of interest signifying that inversion of gas dynamic effects is not a concern.

2. Real gas effects are shown to have no significant impact on compressor performance and stage matching at its current operating conditions. The gradients of the compressibility factor at these conditions are nearly orthogonal to the compression process. The change in Z through the candidate compressor stage is found to be less than 3%. The compressor performance can be accurately modeled with an ideal gas provided that dynamic similarity with the real fluid conditions is preserved.

3. Approaching the critical point, the compressor choke margin is reduced by 9% due to the increase in the isentropic exponent. Furthermore, the swing in corrected mass flow per unit area increases by 5% impacting the matching of downstream components.

4. At high flow coefficients the local flow acceleration around the impeller leading edge causes the thermodynamic conditions to reach below the vapor-pressure curve. The nucleation time scale ratio in these cases however, is found to be much smaller than unity, indicating that condensation is not a concern.

While this investigation focused on supercritical CO_2 compressors used for carbon capture and sequestration, the analytical framework is directly applicable to other non-conventional fluids and applications.

7.2 Recommendations for Future Work

While the variation in real gas properties and the flow expansion through the vapor-pressure curve are assessed independently in this study, both mechanisms are expected to be more prominent in the immediate vicinity of the critical point. Numerical simulations can be used to investigate their simultaneous effect on compressor performance. The singular behavior of thermodynamic properties at the critical point however, might prevent the numerical schemes from capturing important trends in the gas dynamics of the flow. The classical nucleation theory on the other hand might not provide an accurate description of the phase change processes occurring in this region. These limitations might require the initiation of experimental efforts.

Canonical flow experiments could be used to validate the concepts and methods presented in this thesis and to supplement the modeling capabilities in the vicinity of the critical point. The expansion of CO_2 through the vapor-pressure curve in a converging-diverging nozzle experiment could provide important insight into the impact of metastable conditions on the corrected mass flow per unit area, in addition to the non-equilibrium condensation of CO_2 at high pressures where coalescence of molecules can be significant. The experimental work could be extended to a centrifugal compressor stage to validate the key findings of this thesis.

Another direction for continuation of this work is the matching of compressor stages. The corrected mass flow per unit area analysis discussed in this thesis can be incorporated in through flow codes to explore the sensitivity of multistage configu-

rations to fluctuations in inlet conditions and to improve current practices for stage matching.

Bibliography

[1] Wada, N., Sato, T., Tasaki, A., Masutani, J. "High Performance, High Reliability Re-injection Compressors for Green House Gas (CO2)". *Mitsubishi Heavy Industries Technical Review*, 41(1), Feb 2004.

[2] Sato, T., Tasaki, A., Masutani, J. "Re-injection Compressor for Greenhouse Gas (CO2)". *Mitsubishi Heavy Industries Technical Review*, 41(3), June 2004.

[3] Colonna, P., Harinck, J. "Real-Gas Effects in Organic Rankine Cycle Turbine Nozzles". *Journal of Propulsion and Power*, 24:282–294, 2008.

[4] Casey, M., Marty, F. "Centrifugal Compressors - Performance at Design and Off-Design". *The Institute of Refrigeration - Proceedings*, 5:1–10, 1985-86.

[5] Casey, M. "The Effects of Reynolds Number on the Efficiency of Centrifugal Compressor Stages". *Journal of Engineering for Gas Turbines and Power*, 107:541–548, 1985.

[6] Schultz, J. "Polytropic Analysis of Centrifugal Compressors". *Journal of Engineering for Power*, January:69–89, 1962.

[7] US EPA. Report on the Environment. Technical report, 2009.

[8] Kobayashi, S., Van Hassel, B. "CO2 Reduction by Oxy-Fuel Combustion: Economics and Opportunities". In *GCEP Advanced Coal Workshop, Provo, UT, March 15, 2005.*

[9] Moore, J.J., Nored, M.G. "Novel Concepts For The Compression of Large Volumes of Carbon Dioxide". *Proceedings of ASME Turbo Expo*, 2008.

[10] Moore, J.J., Lerche, A., Allison, T., Moreland, B., Pacheco, J. "Development of an Internally Cooled Centrifugal Compressor For Carbon Capture and Storage Applications". *Proceedings of ASME Turbo Expo*, 2012.

[11] Kimball, K. J., Clementoni, E. M. "Supercritical Carbon Dioxide Brayton Power Cycle Development Overview". *Proceedings of ASME Turbo Expo*, 2012.

[12] Conboy, T., Wright, S., Pasch, J., Fleming, D., Rochau, G., Fuller, R. "Performance Characteristics of an Operating Supercritical CO2 Brayton Cycle". *Proceedings of ASME Turbo Expo*, 2012.

[13] Turchi, C. S., Ma, Z., Dyreby, J. "Supercritical Carbon Dioxide Power Cycle Configurations for Use in Concentrating Solar Power Systems". *Proceedings of ASME Turbo Expo*, 2012.

[14] Wright, S., Radel, R., Vemon, M., Rochau, G., Pickard, P. "Operation and analysis of a Supercritical CO2 Brayton Cycle". Technical Report SAND2010-0171, Sandia National Laboratories, September 2010.

[15] Fuller, R., Noall, J., Preuss, J. "Turbomachinery For Supercritical CO2 Power Cycles". *Proceedings of ASME Turbo Expo*, 2012.

[16] Lee, J., Ahn, Y., Lee, J. I., Yoon, H. "Design Methodology of Supercritical CO2 Brayton Cycle Turbomachineries". *Proceedings of ASME Turbo Expo*, 2012.

[17] Pecnik, R., Colonna, P. "Accurate CFD Analysis of a Radial Compressor Operating with Supercritical CO2". In *Supercritical CO2 Power Cycle Symposium*, 2011.

[18] Lüdtke, K.H. *Process Centrifugal Compressors*. Springer, 2003. Chapter 2.

[19] Span, R., Wagner, W. "A New Equation of State for Carbon Dioxide Covering the Fluid Region from the Triple-Point Temperature to 1100 K at Pressures up to 800 MPa". *Journal of Physical and Chemical Reference Data*, 25:1509–1596, 1996.

[20] Lee, B. I., Kesler, M. G. "A Generalized Thermodynamic Correlation Based on Three-Parameter Corresponding States". *American Institute of Chemical Engineering*, 21, No. 3:510–527, 1975.

[21] Manji, A.H., Lielmezs, J. "Note on The Applicability of The Lee-Kesler Equation of State For P-V-T Calculations". *Thermochimica Acta*, 75:207–218, 1984.

[22] Vesovic, V., Wakeham, W.A., Olchowy, G.A., Sengers, J.V., Watson, J.T.R., Millat, J. "The Transport Properties of Carbon Dioxide". *Journal of Physical and Chemical Reference Data*, 19:763–808, 1990.

[23] Fenghour, A., Wakeham, W.A., Vesovic, V. "The Viscosity of Carbon Dioxide". *Journal of Physical and Chemical Reference Data*, 27:31–44, 1998.

[24] Linstrom, P.J., Mallard, W.G. *NIST Chemistry WebBook, NIST Standard Reference Database Number 69.* National Institute of Standards and Technology, Gaithersburg MD, 20899. http://webbook.nist.gov (retrieved February to May 2011).

[25] Greitzer, E. M., Tan, C. S., Graf, M. B. *Internal Flow Concepts and Applications.* Cambridge University Press, 2004.

[26] Thompson, P. "A Fundamental Derivative in Gas Dynamics". *Physics of Fluids*, 14:1843–1849, 1971.

[27] Cumpsty, N. A. *Compressor Aerodynamics.* Krieger Publishing Co, 1989.

[28] Casey, M., Dalbert, P., Schurter, E. "Radial Compressor Stages for Low Flow Coefficients". *Institute of Mechanical Engineers*, C403/004:117–126, 1990.

[29] Ryzhov, Y. A., Pirumov, U. G., Gorbunov, V. N. *Non-Equilibrium Condensation in High-Speed Gas Flows.* Gordon and Breach Science Publishers, 1989.

[30] Gyarmathy, G. *"Grundlagen Einer Theorie der Nassdampfturbine".* PhD thesis, No. 3221, ETH Zürich, 1962.

[31] Starzmann, J., Casey, M. V. "Non-Equilibrium Condensation Effects on the Flow Field and the Performance of Low Pressure Steam Turbine". *Proceedings of ASME Turbo Expo*, 2010.

[32] Li, Z., Zhong, J., Levin, D. "Modeling of CO2 Homogeneous and Heterogeneous Condensation Plumes". *Journal of Physical Chemistry C*, 114:5276–5286, 2010.

[33] ANSYS Inc. *ANSYS CFX - Solver Theory Guide*, November 2010.

Appendix A

Additional Thermodynamic Relations

A.1 Useful Mathematical Relations

A given function of two variables $F = F(x, y)$ can be written in differential form as

$$dF = Bdx + Cdy \ . \tag{A.1}$$

The exactness criteria for this function states

$$\left(\frac{\partial B}{\partial y}\right)_x = \left(\frac{\partial C}{\partial x}\right)_y \ . \tag{A.2}$$

For a function of three variables $F = F(x, y, z)$, where

$$dF = Bdx + Cdy + Ddz \tag{A.3}$$

the exactness criteria state

$$\begin{aligned} \left(\frac{\partial B}{\partial y}\right)_{x,z} &= \left(\frac{\partial C}{\partial x}\right)_{y,z} \\ \left(\frac{\partial B}{\partial z}\right)_{x,y} &= \left(\frac{\partial D}{\partial x}\right)_{y,z} \\ \left(\frac{\partial C}{\partial z}\right)_{x,y} &= \left(\frac{\partial D}{\partial y}\right)_{x,z} \end{aligned} \tag{A.4}$$

The three variables x,y, and z are related by the cyclic relation rule

$$\left(\frac{\partial x}{\partial y}\right)_z \left(\frac{\partial y}{\partial z}\right)_x \left(\frac{\partial z}{\partial x}\right)_y = -1 \quad . \tag{A.5}$$

A.2 Maxwell Relations

For the Gibbs equation in general terms (1^{st} and 2^{nd} law combined)

$$du = Tds - pdv \tag{A.6}$$

$$dh = vdp + Tds \tag{A.7}$$

$$da = -pdv - sdT \tag{A.8}$$

$$dg = -sdT + vdp \tag{A.9}$$

applying the exactness criteria gives the Maxwell relations

$$\left(\frac{\partial T}{\partial v}\right)_s = -\left(\frac{\partial p}{\partial s}\right)_v$$

$$\left(\frac{\partial v}{\partial s}\right)_p = \left(\frac{\partial T}{\partial p}\right)_s$$

$$\left(\frac{\partial p}{\partial T}\right)_v = -\left(\frac{\partial s}{\partial v}\right)_T$$

$$\left(\frac{\partial s}{\partial p}\right)_T = \left(\frac{\partial v}{\partial T}\right)_p \tag{A.10}$$

From Eq. A.7 it follows that

$$\left(\frac{\partial h}{\partial p}\right)_T = v + T\left(\frac{\partial s}{\partial p}\right)_T \quad .$$

Substituting the Maxwell relation yields the final form of Eq. 3.2. Similarly, from Eq. A.6 it follows that

$$\left(\frac{\partial u}{\partial v}\right)_T = T\left(\frac{\partial s}{\partial v}\right)_T - p$$

and using the Maxwell relations gives

$$\left(\frac{\partial u}{\partial v}\right)_T = T\left(\frac{\partial p}{\partial T}\right)_v - p \quad . \tag{A.11}$$

A.3 Alternative Derivation of Isentropic Relations

An alternative way to derive the isentropic relations, discussed in Chapter 3, is by considering the expression of an isentrope in T-p space

$$Tp^{-m_s} = const \tag{A.12}$$

where m_s is the temperature isentropic exponent. In differential form Eq. A.12 can be written as

$$\frac{dT}{T} - m_s\frac{dp}{p} = 0\Big|_{s=const}$$

or equivalently

$$m_s = \frac{p}{T}\left(\frac{\partial T}{\partial p}\right)_s \quad . \tag{A.13}$$

Eq. A.13 can be expressed in terms of the isothermal and isobaric compressibilities, similar to n_s. Using Eq. 3.11 and 3.12, a relation for the difference of the specific heats can be obtained

$$c_p - c_v = T\left(\frac{\partial p}{\partial T}\right)_v\left(\frac{\partial v}{\partial T}\right)_p \quad . \tag{A.14}$$

Dividing Eq. A.14 by Eq. 3.11 gives

$$\frac{c_p - c_v}{c_p} = \frac{\gamma - 1}{\gamma} = \left(\frac{\partial p}{\partial T}\right)_v \left(\frac{\partial T}{\partial p}\right)_s \quad . \tag{A.15}$$

Rearranging the terms and using the fact that

$$\frac{\beta_T}{\beta_p} = \left(\frac{\partial T}{\partial p}\right)_v \tag{A.16}$$

yields

$$\left(\frac{\partial T}{\partial p}\right)_s = \frac{\gamma - 1}{\gamma}\frac{\beta_T}{\beta_p} \quad . \tag{A.17}$$

Substituting Eq. A.17 into Eq. A.13 gives the final form of the isentropic exponent shown in Table 3.2

$$m_s = \frac{\gamma - 1}{\gamma}\frac{\beta_T p}{\beta_p T} \quad . \tag{A.18}$$

Another way to express m_s is by multiplying both sides of Eq. 3.11 by $T/(pv)$ yielding

$$m_s \frac{T}{pv} = \frac{\beta_p T}{c_p} \quad . \tag{A.19}$$

Substituting Eq. A.19 into Eq. 3.19 gives

$$dh = \frac{1}{m_s}\frac{pv}{T}dT \tag{A.20}$$

The ratio between stagnation and static temperature can be obtained by integrating Eq. A.20. The integral of the left hand side is given by Eq. 3.22. To integrate the right hand side however, an assumption is made that the isentropic exponents remain constant. Using the isentropic relation

$$\frac{T_t}{T} = \left(\frac{p_t}{p}\right)^{m_s} = \left(\frac{v_t}{v}\right)^{-n_s m_s} \tag{A.21}$$

the right hand side of Eq. A.20 can be written as

$$\int_{T}^{T_t} \frac{1}{m_s} p_t v_t \left(\frac{T}{T_t}\right)^{\frac{n_s-1}{n_s m_s}} dT = v_t p_t \left[1 - \left(\frac{T}{T_t}\right)^{\frac{n_s-1}{n_s m_s}}\right] \frac{n_s}{n_s - 1} \quad . \tag{A.22}$$

Equating the two sides of Eq. A.20 yields

$$\frac{M^2}{2} = \frac{v_t p_t}{vp} \left[1 - \left(\frac{T}{T_t}\right)^{\frac{n_s-1}{n_s m_s}}\right] \frac{1}{n_s - 1} \quad . \tag{A.23}$$

Using Eq. A.21 to express pressure and the specific volume ratios in terms of the temperature ration and rearranging gives

$$\frac{T_t}{T} = \left(1 + \frac{n_s - 1}{2} M^2\right)^{\frac{m_s n_s}{n_s - 1}} \tag{A.24}$$

which is consistent with the one derived in Section 3.3.

Appendix B

Influence Coefficients for 1-D Compressible Flow

Detailed derivation of the influence coefficients for 1-D compressible channel flow for real gas are presented here. These are derived by coupling the governing equations of fluid motion with the real gas equation of state. A general case is considered for a flow in a channel with varying area and shaft work, but with no mass injection, heat transfer, friction, or body forces acting on it.

The differential form of the real gas equation of state can be written as

$$\frac{dp}{p} = \frac{d\rho}{\rho} + \frac{dT}{T} + \frac{dZ}{Z} \quad . \tag{B.1}$$

Expressing Z as a function of temperature and pressure yields

$$dZ = \left(\frac{\partial Z}{\partial T}\right)_p dT + \left(\frac{\partial Z}{\partial p}\right)_T dp \quad . \tag{B.2}$$

Dividing both sides by Z and using the definitions of β_T and β_p from Table 3.1 gives

$$\frac{dZ}{Z} = \frac{T}{Z}\left(\frac{\partial Z}{\partial T}\right)_p \frac{dT}{T} + \frac{p}{Z}\left(\frac{\partial Z}{\partial p}\right)_T \frac{dp}{p} = (\beta_p T - 1)\frac{dT}{T} + (1 - \beta_T p)\frac{dp}{p} \quad . \tag{B.3}$$

Substituting Eq. B.3 into B.1 and combining the terms yields

$$(\beta_T p)\,\frac{dp}{p} - (\beta_p T)\,\frac{dT}{T} = \frac{d\rho}{\rho} \quad . \tag{B.4}$$

The conservation of mass, momentum and energy can be written in differential form as

$$\frac{d\rho}{\rho} + \frac{dc}{c} = -\frac{dA}{A} \tag{B.5}$$

$$cdc + \frac{1}{\rho}dp = -\frac{dF_{shaft}}{\rho A} \tag{B.6}$$

$$dh_t = dh + cdc = -dw_{shaft} \tag{B.7}$$

where dF_{shaft} is the force exerted by the shaft on the fluid, and dw_{shaft} is the shaft work. The two are related by $\dot{m}dw_{shaft} = cdF_{shaft}$. Substituting this relation in the momentum equation yields

$$cdc + \frac{1}{\rho}dp = -dw_{shaft} \tag{B.8}$$

The caloric equation of state, Eq. 3.3, can be substituted in Eq. B.7 yielding

$$c_p dT + \frac{(1-\beta_p T)}{\rho}dp + cdc = -dw_{shaft} \quad . \tag{B.9}$$

Eq. B.8 and B.9 can be combined such that the velocity and shaft work terms drop out and a relationship between the temperature and pressure terms can be obtained

$$c_p dT = \frac{\beta_p T}{\rho}dp \quad . \tag{B.10}$$

Using Eq. **??** and A.19, Eq. B.10 can be rewritten as

$$\frac{dT}{T} = \frac{\gamma - 1}{\gamma}\frac{\beta_T p}{\beta_p T}\frac{dp}{p} \quad . \tag{B.11}$$

Substituting Eq. B.11 in B.4 yields a relation between changes in density and changes in pressure via

$$\frac{d\rho}{\rho} = \frac{\beta_p T}{\gamma}\frac{dp}{p} \quad . \tag{B.12}$$

Combining Eq. B.12 with the conservation of mass, Eq. B.5, in turn gives a relationship between changes in velocity to changes in pressure and area by

$$\frac{dc}{c} = -\frac{dA}{A} - \frac{\beta_T p}{\gamma}\frac{dp}{p} \quad . \tag{B.13}$$

The final expression that relates dp/p to the two independent variables dA/A and $dw_{shaft}/\left(c_p T\right)$ is obtained by dividing both sides of the momentum equation by ρc^2. Using the relation

$$c^2 = a^2 M^2 = n_s p v M^2 = M^2 \frac{\gamma - 1}{\left(\beta_p T\right)^2} c_p T \quad . \tag{B.14}$$

Eq. B.6 can be rewritten as

$$\frac{dc}{c} + \frac{\beta_T p}{\gamma M^2}\frac{dp}{p} = -\frac{\left(\beta_p T\right)^2}{\left(\gamma - 1\right) M^2}\frac{dw_{shaft}}{c_p T} \quad . \tag{B.15}$$

Plugging Eq. B.13 into B.15 and rearranging the terms yields

$$\frac{dp}{p} = \left[\frac{\gamma M^2}{\left(1 - M^2\right)}\frac{1}{\beta_T p}\right]\frac{dA}{A} - \left[\frac{1}{\left(1 - M^2\right)}\frac{1}{\left(\gamma - 1\right)}\frac{\left(\beta_p T\right)^2}{\left(\beta_T p\right)}\right]\frac{dw_{shaft}}{c_p T} \quad . \tag{B.16}$$

where the terms inside the square brackets represent the influence coefficients for dp/p, given in Table 3.3. The influence coefficients for dT/T, $d\rho/\rho$, and dc/c can be obtained by substituting Eq. B.16 into Eq. B.11, B.12, and B.13 respectively.

$$\frac{dT}{T} = \left[\frac{M^2}{\left(1 - M^2\right)}\frac{\gamma - 1}{\beta_p T}\right]\frac{dA}{A} - \left[\frac{\beta_p T}{\left(1 - M^2\right)}\right]\frac{dw_{shaft}}{c_p T} \tag{B.17}$$

$$\frac{d\rho}{\rho} = \left[\frac{M^2}{(1-M^2)}\right]\frac{dA}{A} - \left[\frac{1}{(1-M^2)}\frac{(\beta_p T)^2}{(\gamma-1)}\right]\frac{dw_{shaft}}{c_p T} \tag{B.18}$$

$$\frac{dc}{c} = -\left[\frac{1}{(1-M^2)}\right]\frac{dA}{A} + \left[\frac{1}{(1-M^2)}\frac{(\beta_p T)^2}{(\gamma-1)}\right]\frac{dw_{shaft}}{c_p T} \tag{B.19}$$

The last two rows in Table 3.3 can be obtained by considering the definition of the fundamental derivative. Eq. 3.33 can be rewritten as

$$\frac{da}{a} = (\Gamma - 1)\frac{d\rho}{\rho} \tag{B.20}$$

Substituting Eq. B.18 into B.20 yields

$$\frac{da}{a} = \left[\frac{(\Gamma-1)M^2}{(1-M^2)}\right]\frac{dA}{A} + \left[\frac{(\Gamma-1)}{(1-M^2)}\frac{(\beta_p T)^2}{(\gamma-1)}\right]\frac{dw_{shaft}}{c_p T} \tag{B.21}$$

Combining Eq. B.19 and B.21 with the definition of speed of sound in differential form

$$\frac{dc}{c} - \frac{da}{a} = \frac{dM}{M} \tag{B.22}$$

gives

$$\frac{dM}{M} = -\left[\frac{1+(\Gamma-1)M^2}{(1-M^2)}\right]\frac{dA}{A} + \left[\frac{\Gamma}{(1-M^2)}\frac{(\beta_p T)^2}{(\gamma-1)}\right]\frac{dw_{shaft}}{c_p T} \tag{B.23}$$

As a final check, if the ideal gas form of the terms β_p, β_T, and Γ are substituted in these equations, the tables presented by Greitzer [25] are reproduced.

Appendix C

Thermodynamic Diagrams for CO_2

The Lee-Kesler equation of state model is used to plot the thermodynamic properties of CO_2 on T-s diagrams. The range of thermodynamic states is from 15 bar to 700 bar in pressure and from -25°C to 200°C. The isobars (in blue) and the isenthalps (in red) are kept the same in all the diagrams. The third property (in green) is different in each diagram. The order of diagrams is as follows:

1. Density
2. Internal energy
3. Isobaric specific heat capacity
4. Isochoric specific heat capacity
5. Ratio of specific heat capacities
6. Speed of sound
7. Joule-Thomson coefficient
8. Isentropic pressure exponent
9. Isentropic temperature exponent
10. Compressibility function $\beta_p T = X + 1$

11. Compressibility function $\beta_T p = Y$

12. Compressibility factor

13. Fundamental Derivative

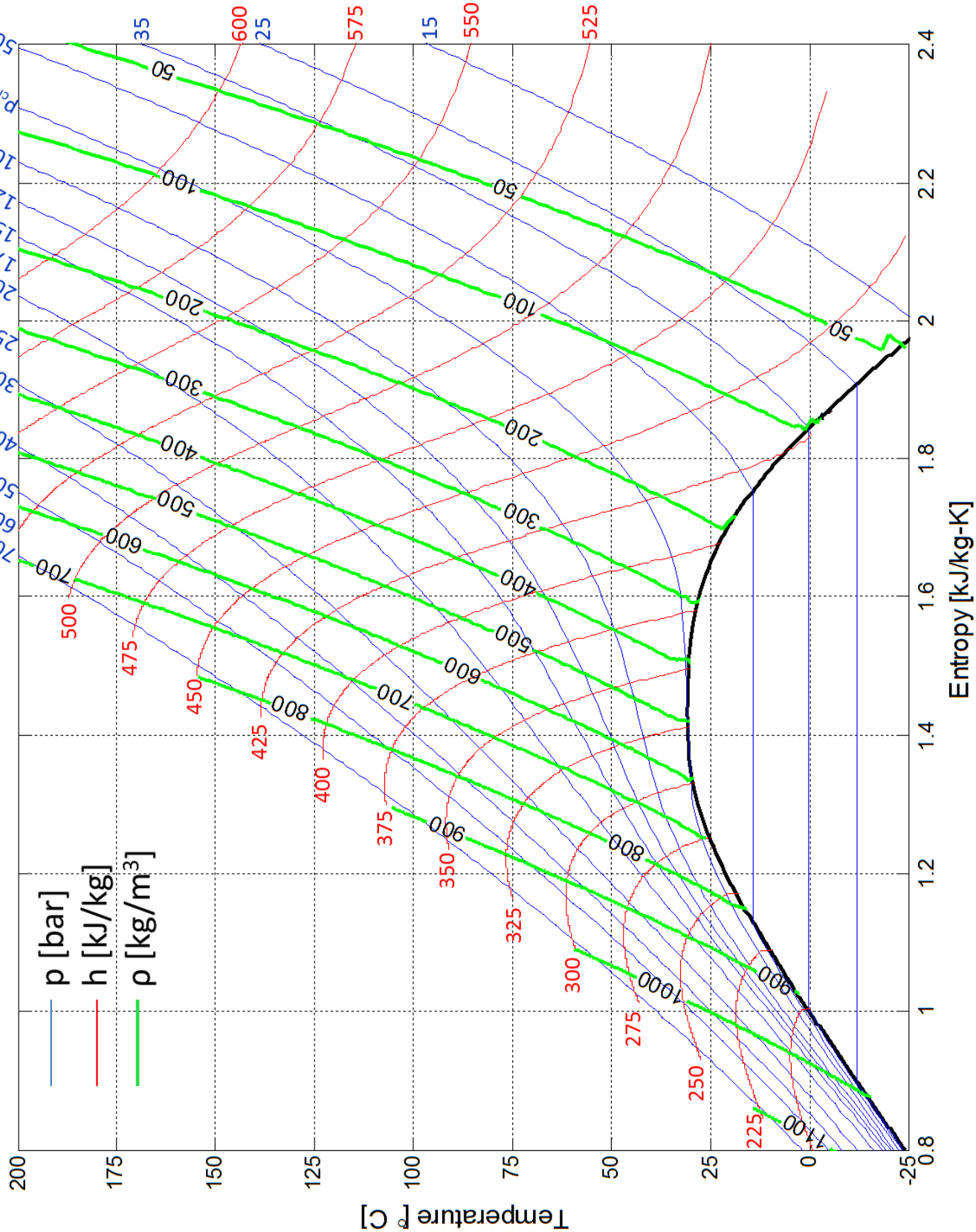

Figure C-1: Contours of density.

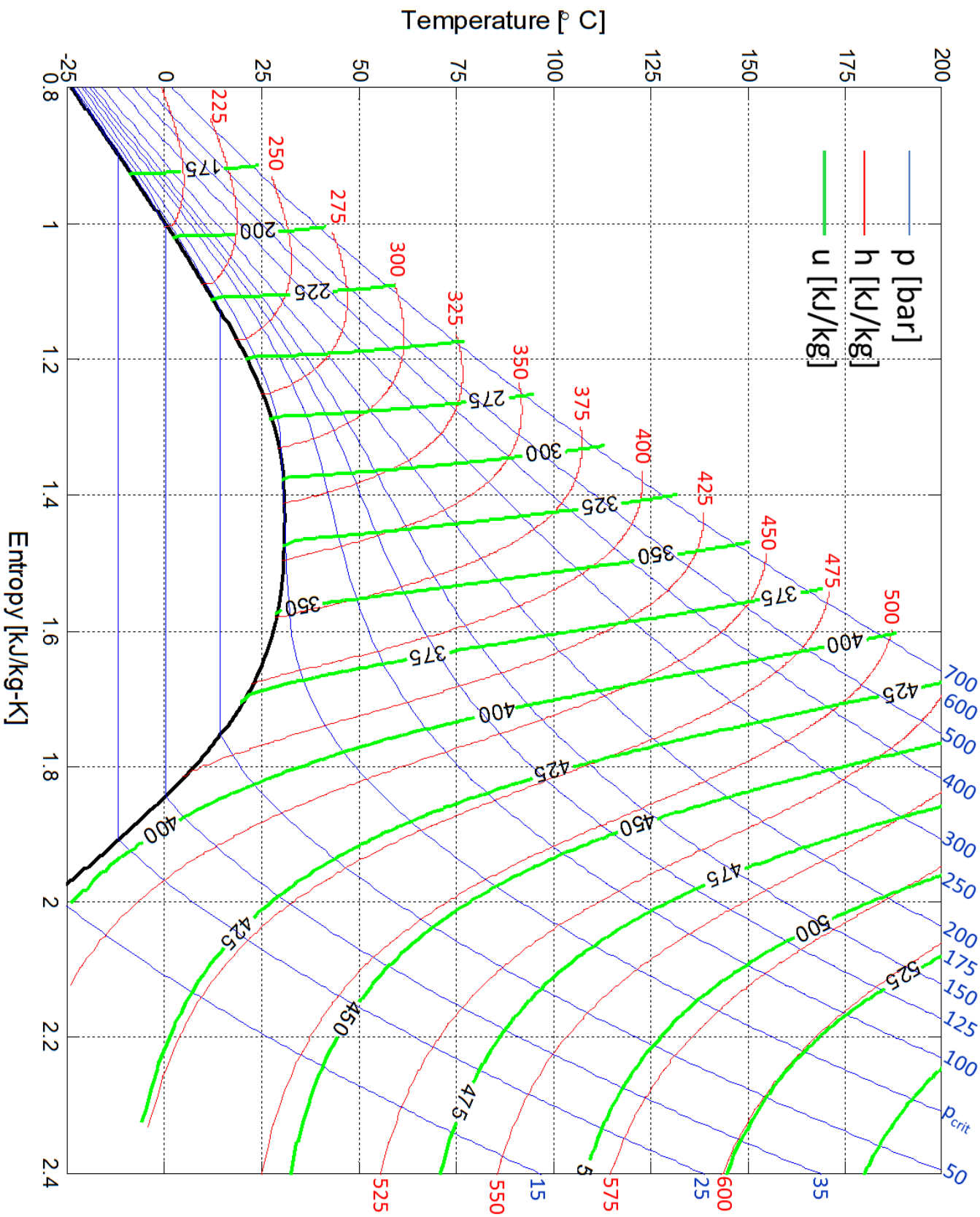

Figure C-2: Contours of internal energy.

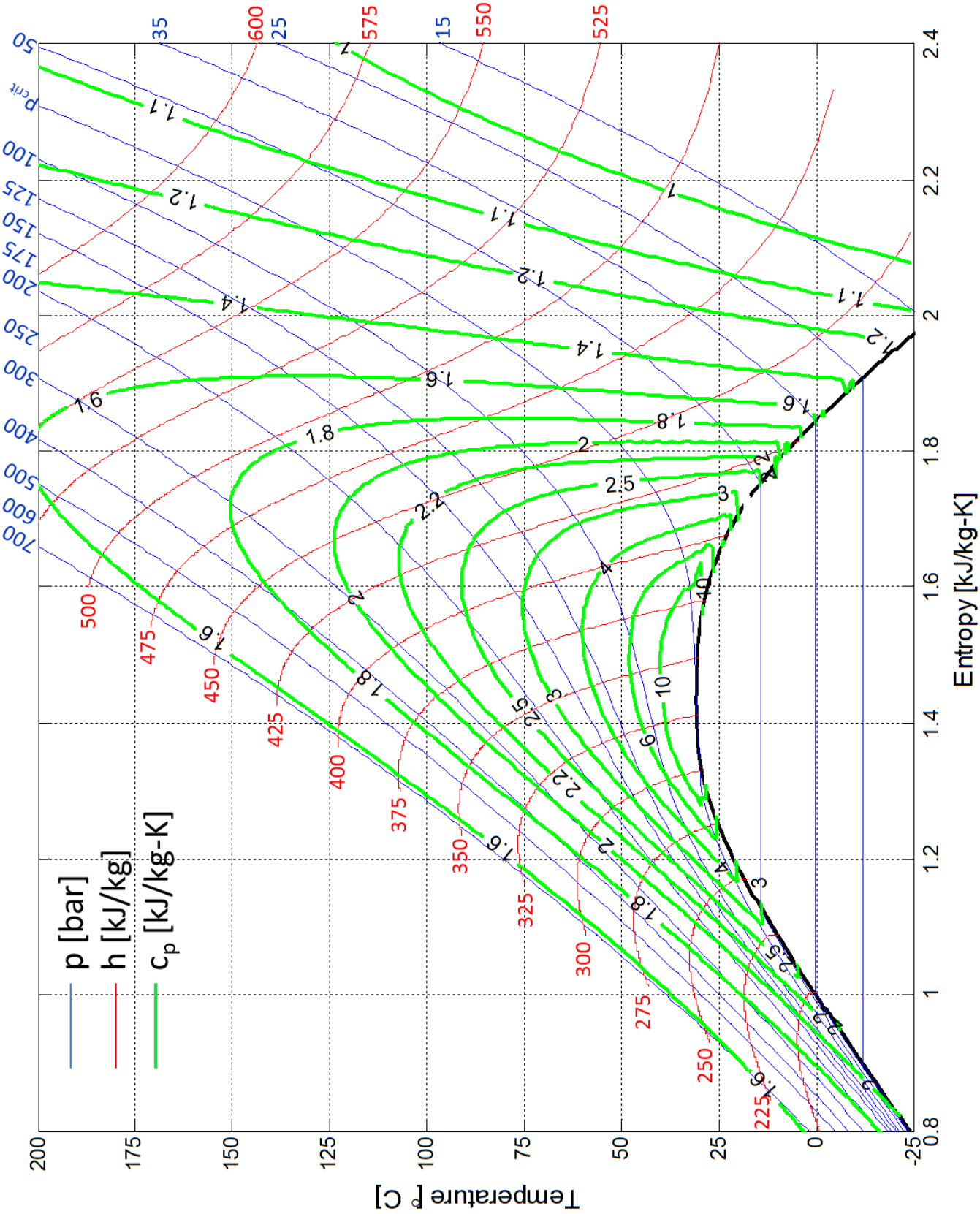

Figure C-3: Contours of isobaric specific heat capacity.

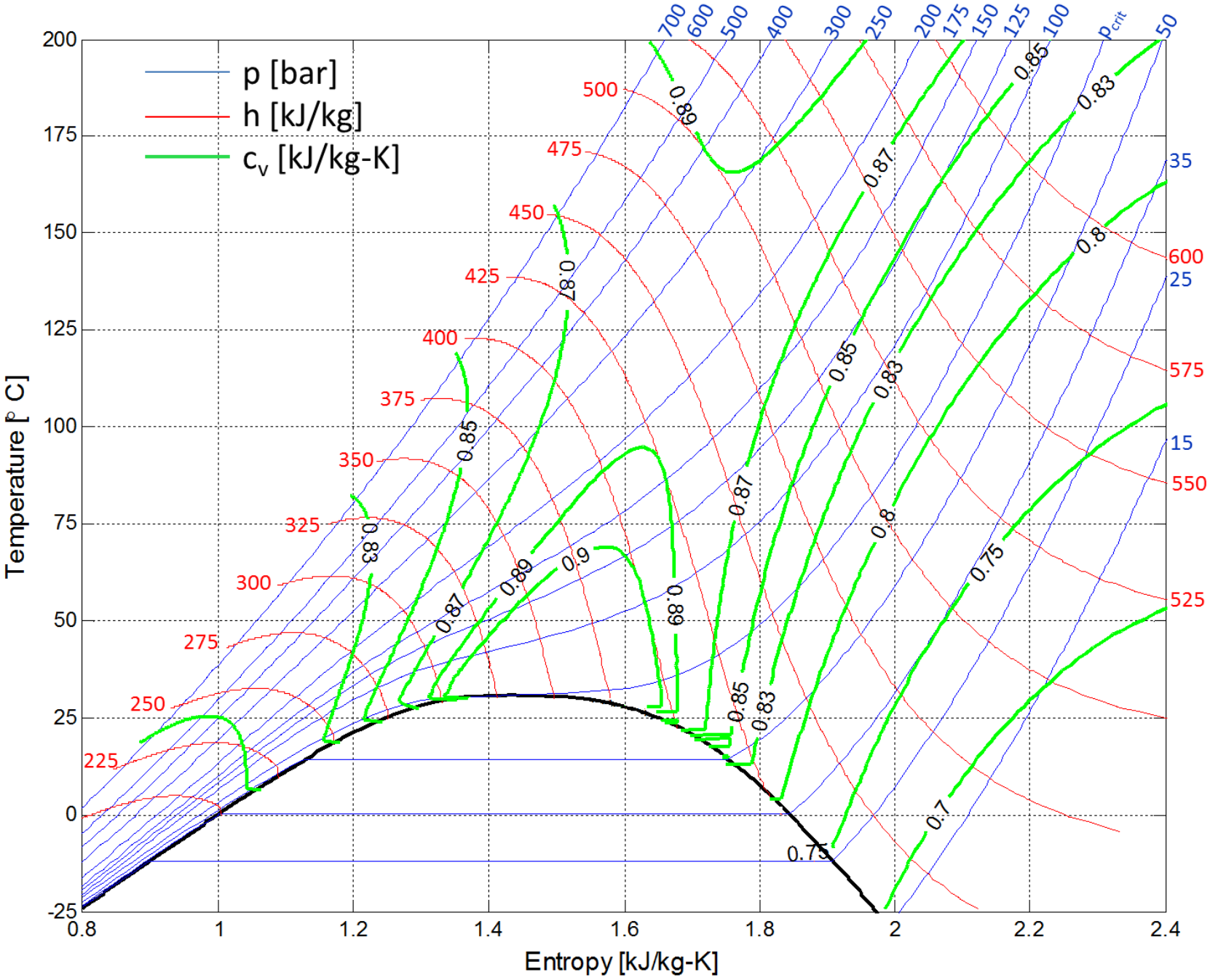

Figure C-4: Contours of isochoric specific heat capacity.

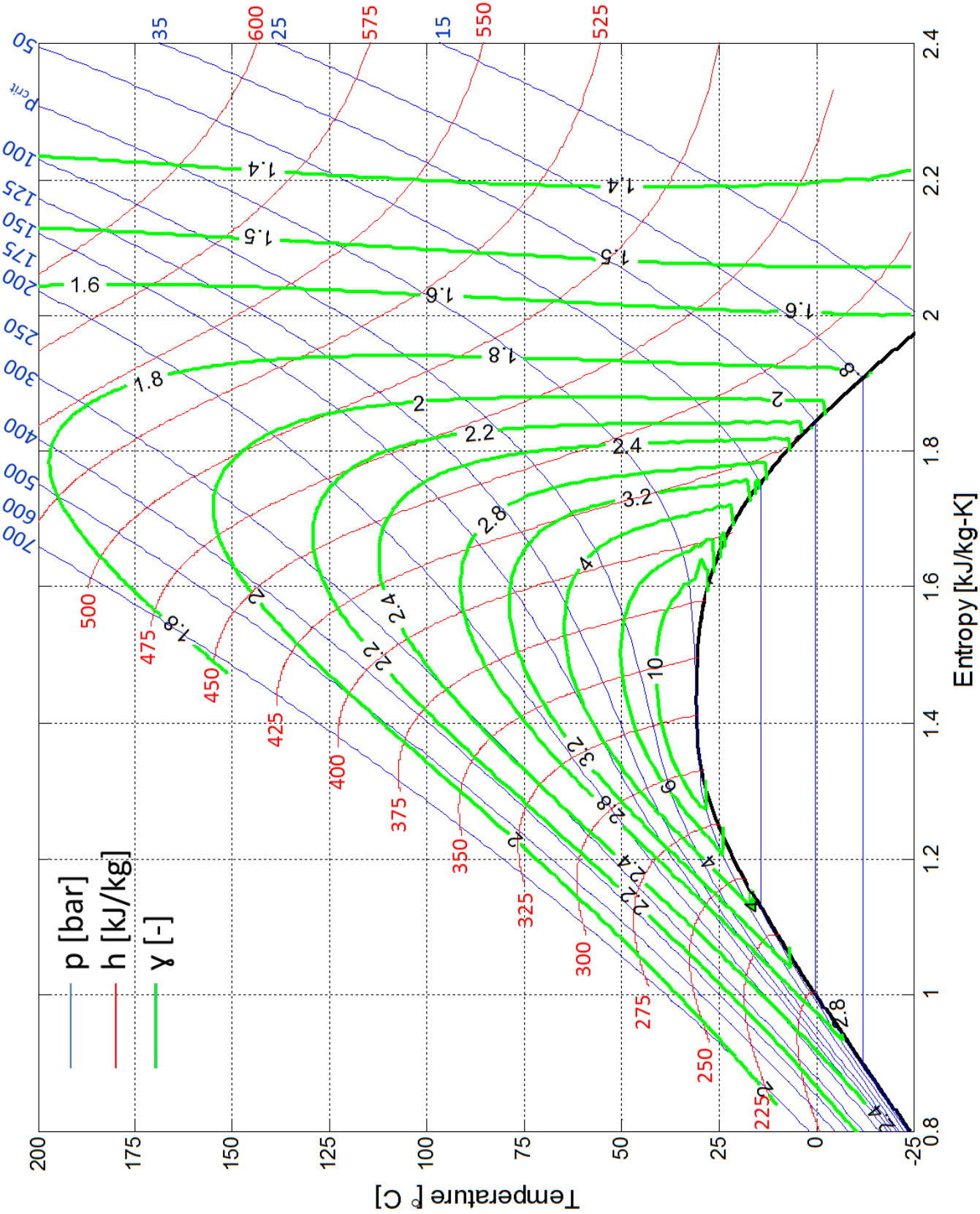

Figure C-5: Contours of ratio of specific heat capacities.

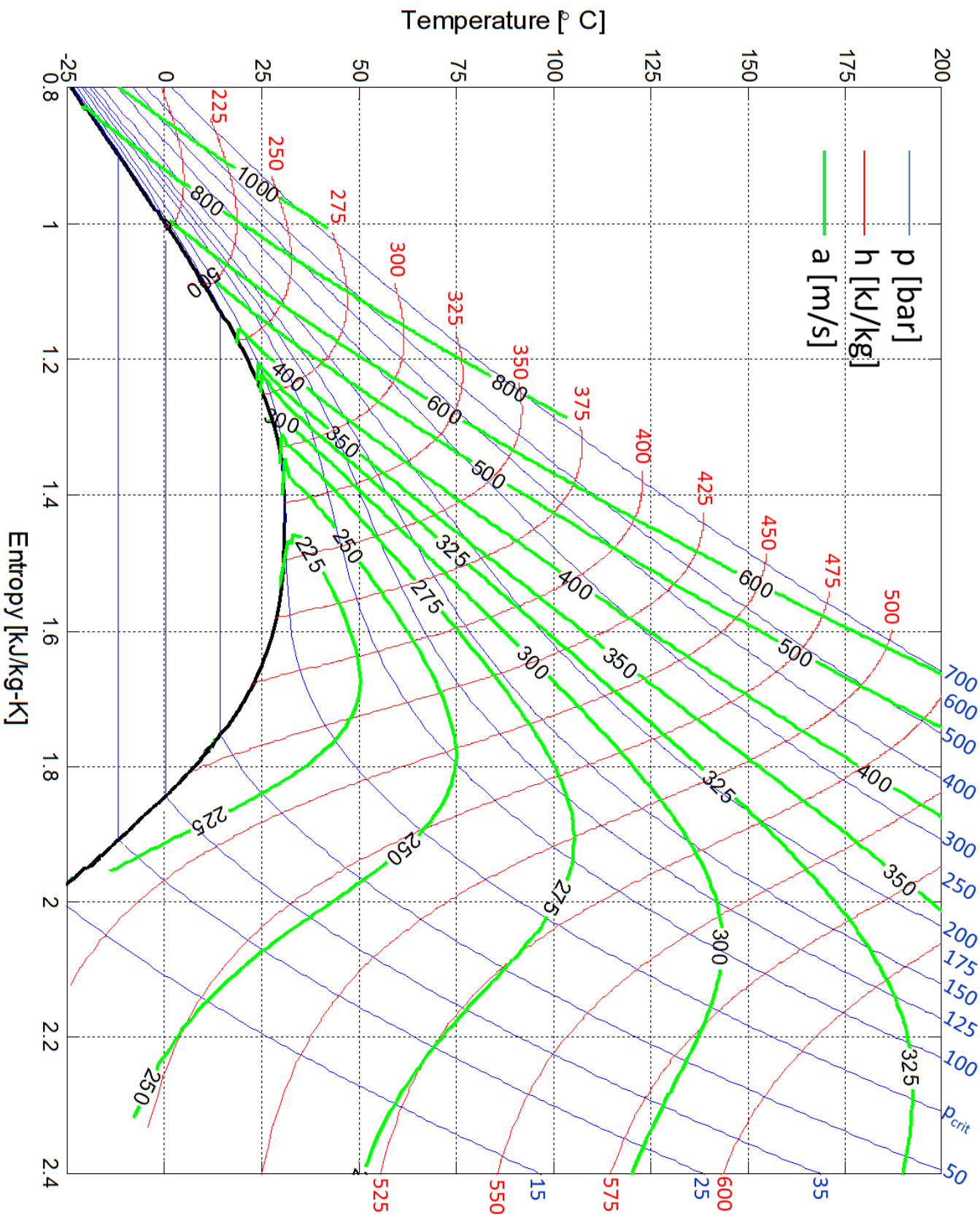

Figure C-6: Contours of speed of sound.

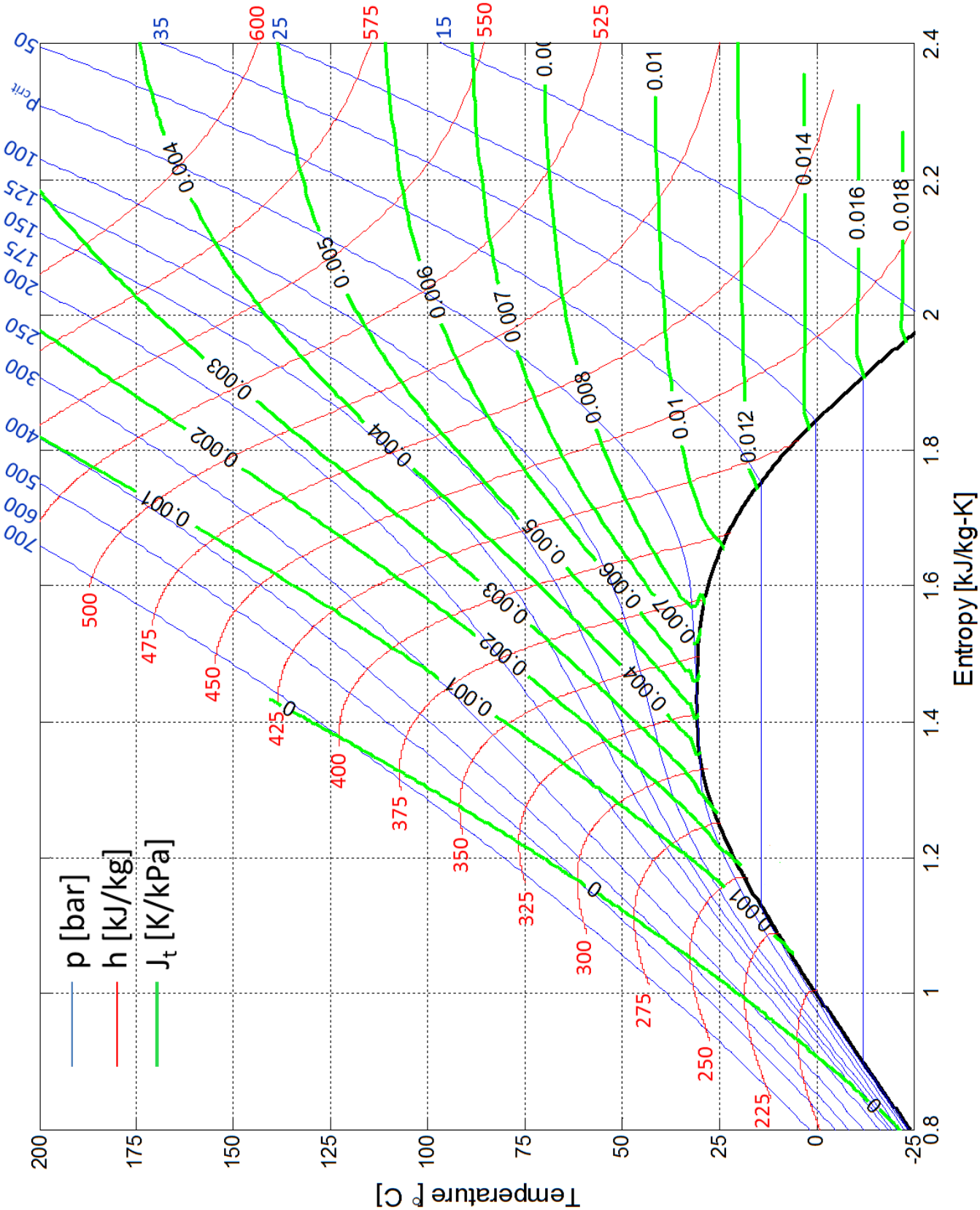

Figure C-7: Contours of Joule-Thomson coefficient.

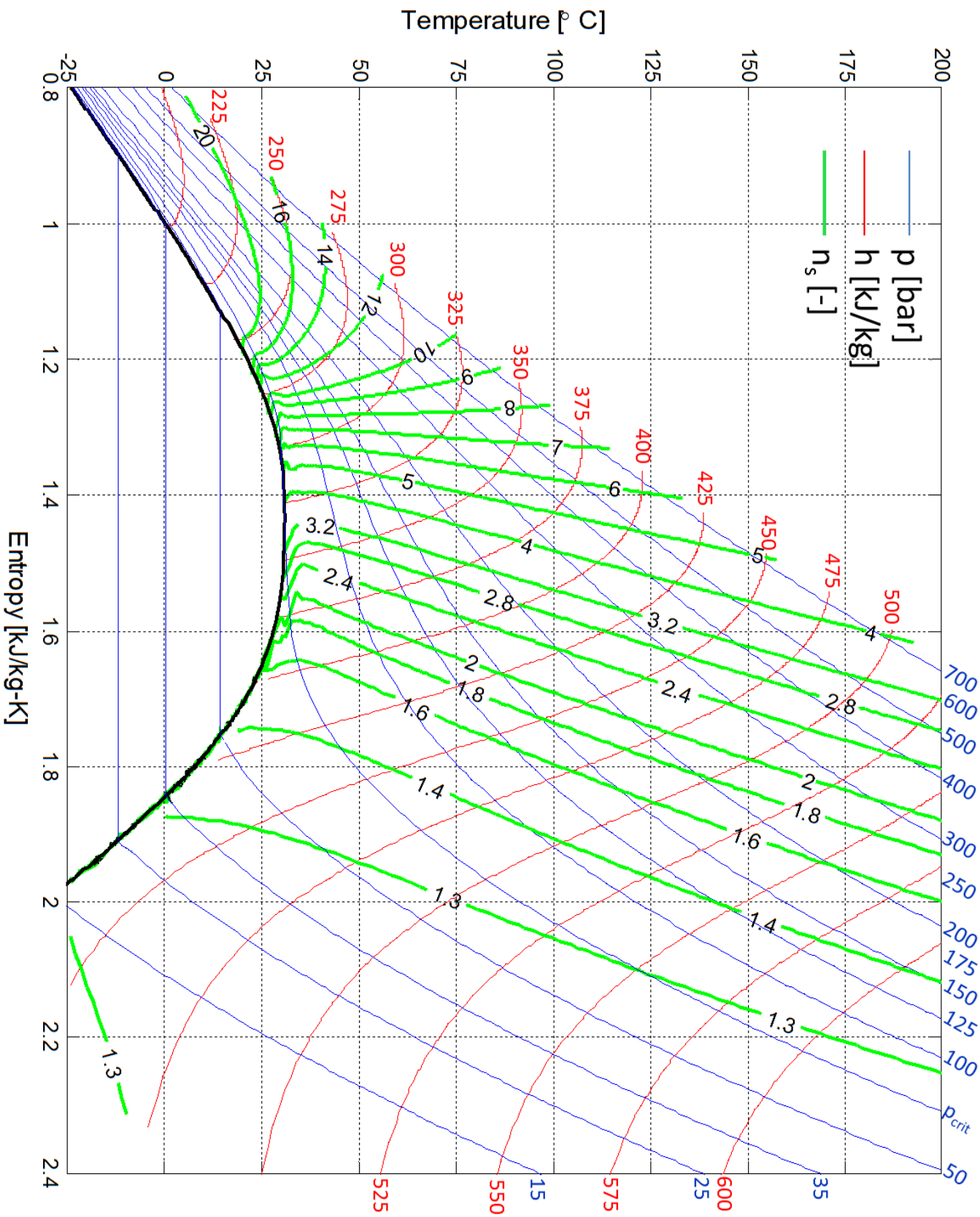

Figure C-8: Contours of isentropic pressure exponent.

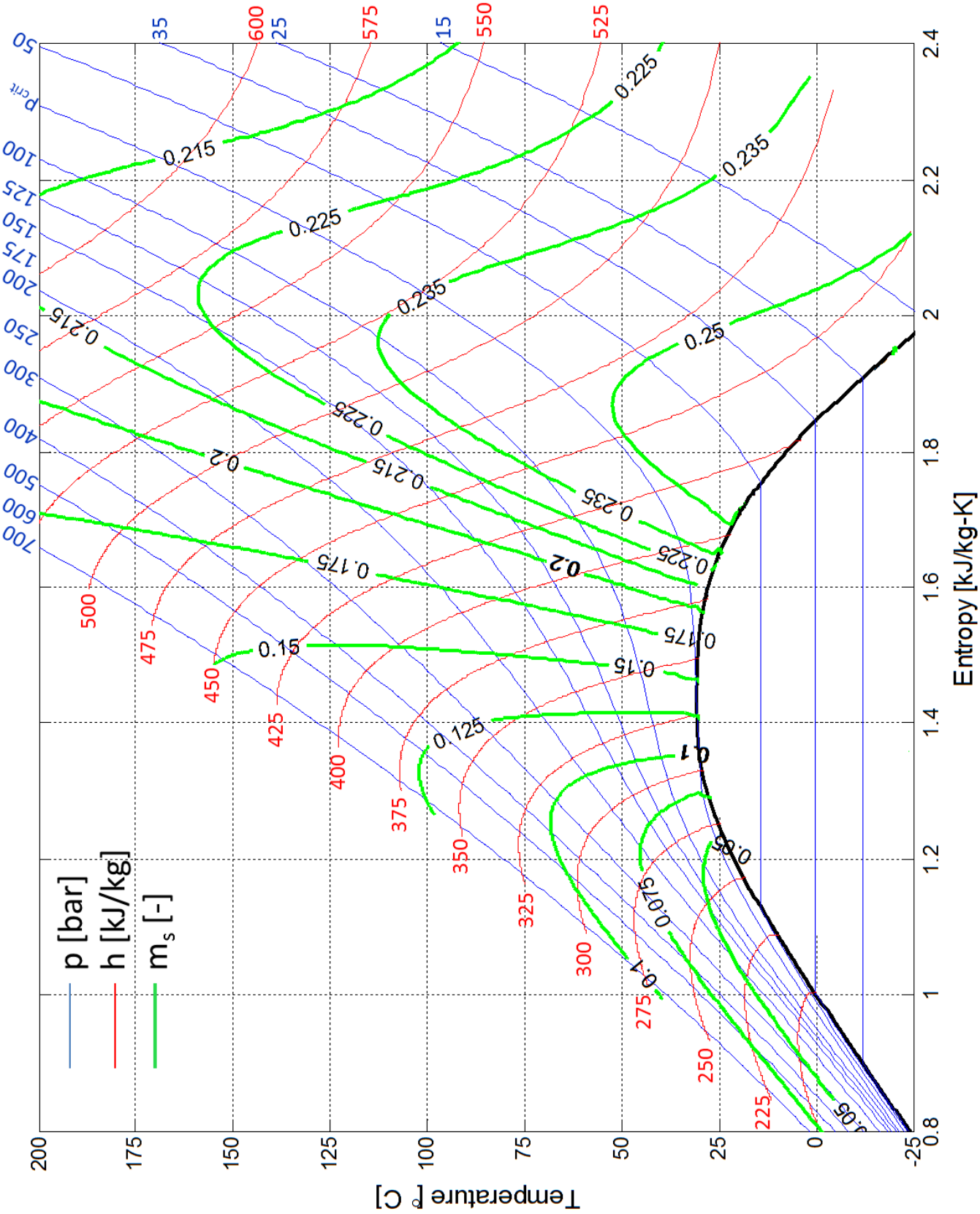

Figure C-9: Contours of isentropic temperature exponent.

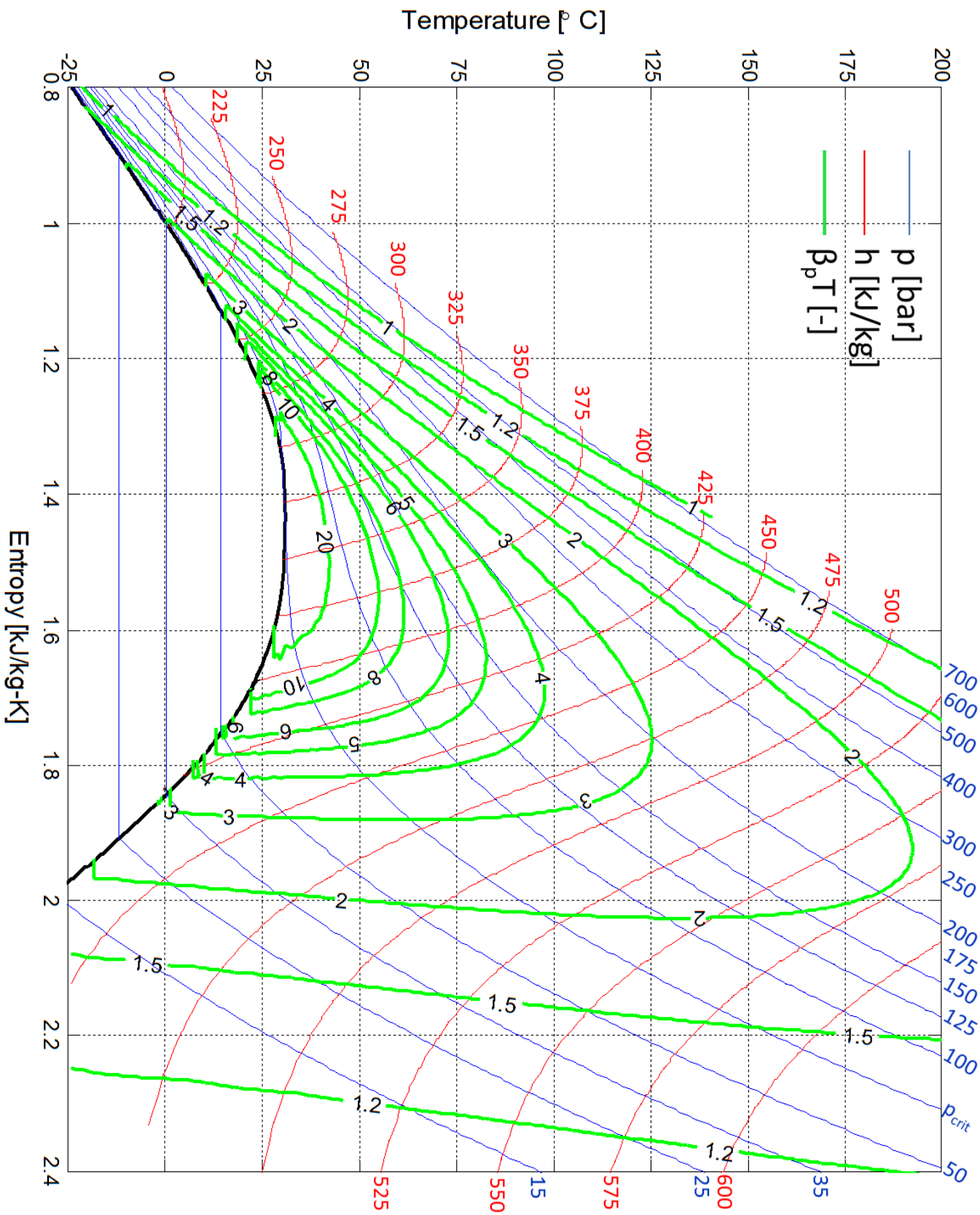

Figure C-10: Contours of compressibility function $\beta_p T = X + 1$.

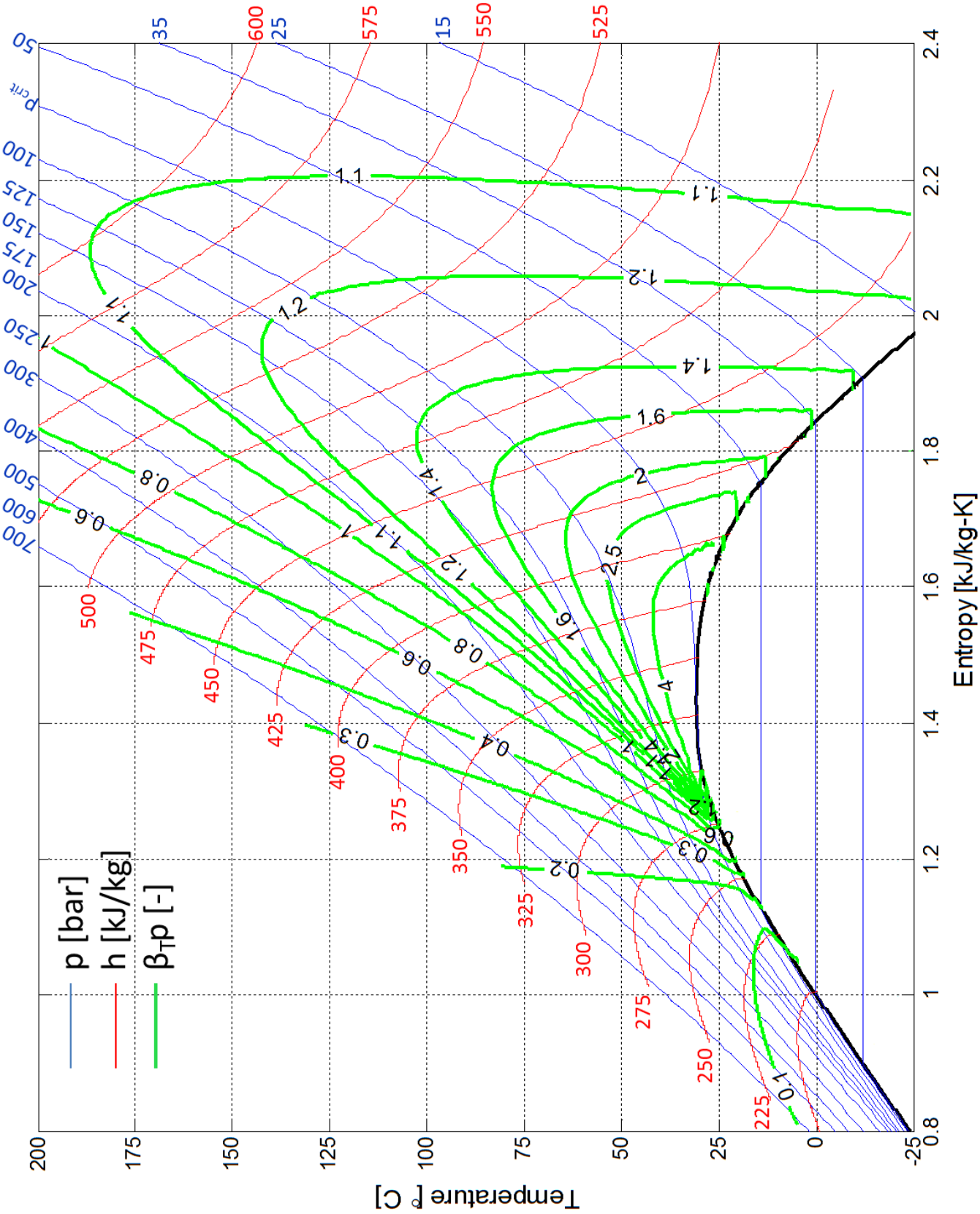

Figure C-11: Contours of compressibility function $\beta_T p = Y$.

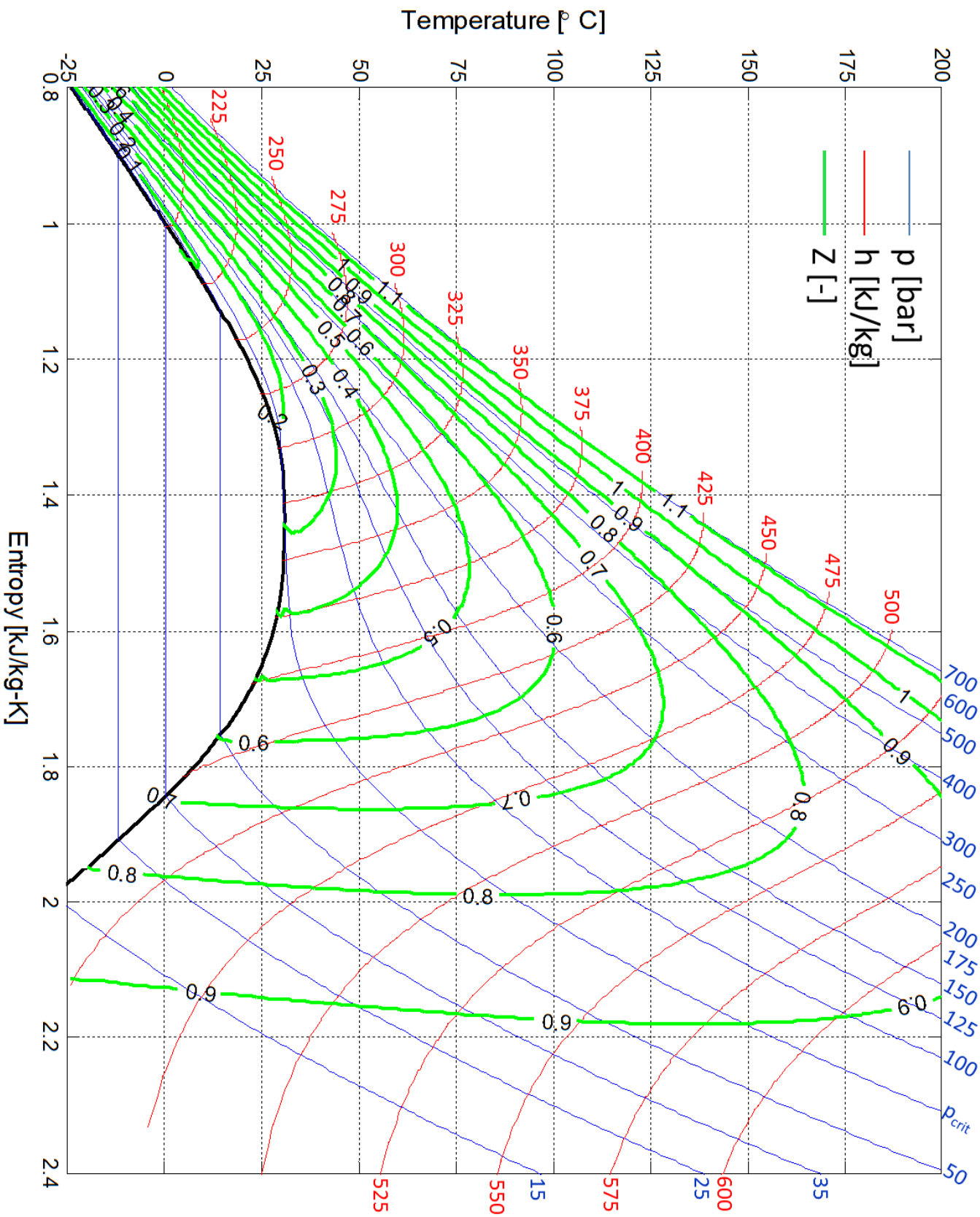

Figure C-12: Contours of compressibility factor.

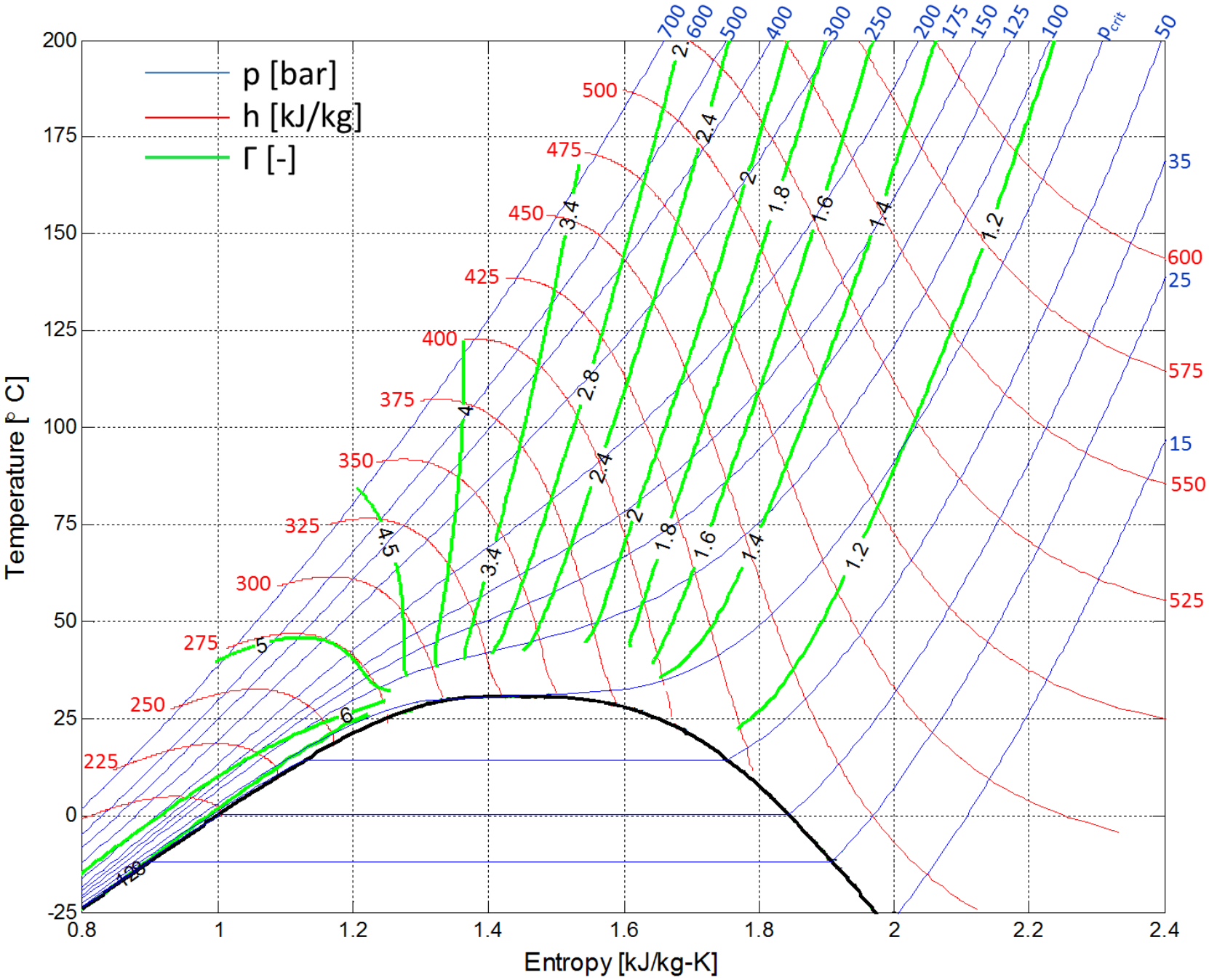

Figure C-13: Contours of fundamental derivative. Values near critical point not shown due to uncertainty in thermodynamic properties.